

**EFFECTS OF FLUX SURFACE SHAPING ON ION
TEMPERATURE GRADIENT TURBULENCE IN TOKAMAKS**

by

Joey M. Duff

A thesis submitted in partial fulfillment
of the requirements for the degree of

Bachelor of Science
(Engineering Physics)

at the

UNIVERSITY OF WISCONSIN - MADISON

2019

Table of Contents

Table of Contents	i
List of Tables	iii
List of Figures	iv
Abstract	vii
1 Introduction	1
1.1 Fusion Energy	1
1.2 Magnetic Confinement Fusion	2
1.2.1 Single Particle Drifts	4
1.2.2 MHD Equilibrium	5
1.2.3 Toroidal Configurations	6
1.3 Ion Temperature Gradient Drift Waves	7
1.4 Turbulence	8
1.5 Thesis Outline	9
2 Magnetic Flux Surfaces	10
2.1 Magnetic Coordinates	10
2.2 Local Equilibrium	11
2.2.1 Miller Equilibrium	12
2.2.2 Three-Dimensional Local Equilibrium	13
2.2.3 Numerical Implementation	15
2.3 Section Summary	16
3 Plasma Turbulence Simulations	17
3.1 Gyrokinetic Theory	17
3.2 Flux Tubes	18
3.3 The GENE Code	20
3.3.1 GENE Normalizations	20
3.4 Types of Microturbulence Calculations	20
3.5 Tokamak Shaping ITG Turbulence Studies	21
3.6 Section Summary	23
4 Linear Studies	24
4.1 Linear Stability Analysis	24
4.1.1 Linear Growth Rates	25
4.2 Quasilinear Heat Flux	30
4.3 Section Summary	33

5	Nonlinear Studies	34
5.1	Simulation Quality	34
5.1.1	Base Case	35
5.1.2	Elongation	37
5.1.3	Triangularity	39
5.2	Nonlinear Heat Flux	46
5.3	Section Summary	51
6	Conclusions	53
6.1	Summary	53
6.1.1	Linear Studies	53
6.1.2	Nonlinear Studies	53
6.2	Future Research	54
6.2.1	Nonlinear Convergence Tests	54
6.2.2	Other Tokamak Shaping Studies	54
6.2.3	Temperature Gradient Scans	54
6.2.4	ITG Saturation Metric	55
6.2.5	Electron Turbulence	55
6.2.6	Stellarator Shaping	55
	References	57

List of Tables

5.1	Comparison of quasilinear and nonlinear heat fluxes for each configuration with a nonlinear simulation performed and the $nz0$, $nv0$, and k_y^{\min} settings for the simulation from which the nonlinear heat flux was calculated. The quasilinear heat flux for the base case was chosen to be equal to the nonlinear heat flux of the base case to set \mathcal{C} for each quasilinear heat flux.	46
-----	--	----

List of Figures

1.1	Reaction cross sections for the D-D, D-He ³ , and D-T fusion reactions as a function of thermal energy [4].	2
1.2	Toroidal (blue) and poloidal (red) directions on a torus [5].	4
1.3	Example of a stellarator (a) and a tokamak (b) where the coils are blue and a surface of constant magnetic flux in the plasma is yellow [6].	6
1.4	Illustration of an ITG instability in a nonhomogeneous plasma with a slab geometry. A temperature gradient in the negative x -direction is represented by hotter ions in blue and colder ions in white. The magnetic field is in the z -direction out of the page with the pressure and magnetic field gradients in the negative x -direction [10].	8
2.1	The cylindrical and toroidal-like coordinate system [12].	10
2.2	Shaped cross section of a tokamak using the Miller equilibrium [17]. The shaping for this equilibrium is prescribed by $A = 3.17$, $\kappa = 1.66$, and $\delta = 0.416$. A circular cross section corresponds to $\kappa = 1$, $\delta = 0$	13
4.1	ITG growth rates of elongated geometries for the base case ($\kappa = 1$) (purple), $\kappa = 1.5$ (green), $\kappa = 2$ (light blue), and $\kappa = 2.5$ (orange) scanned over $k_y\rho_s$ assuming adiabatic electrons.	25
4.2	A stability metric (a) and curvature of the magnetic field (b) along a field line for the base case ($\kappa = 1$) (purple), $\kappa = 1.5$ (green), $\kappa = 2$ (light blue), and $\kappa = 2.5$ (orange).	26
4.3	ITG growth rates of positive triangularity geometries for the base case ($\delta = 0$) (purple), $\delta = 0.25$ (green), $\delta = 0.5$ (light blue), and $\delta = 0.75$ (orange) scanned over $k_y\rho_s$ assuming adiabatic electrons.	27
4.4	A stability metric (a) and curvature of the magnetic field (b) along a field line for the base case ($\delta = 0$) (purple), $\delta = 0.25$ (green), $\delta = 0.5$ (light blue), and $\delta = 0.75$ (orange).	28
4.5	ITG growth rates of negative triangularity geometries for the base case ($\delta = 0$) (purple), $\delta = -0.25$ (yellow), $\delta = -0.5$ (dark blue), and $\delta = -0.75$ (red) scanned over $k_y\rho_s$ assuming adiabatic electrons.	29
4.6	A stability metric (a) and curvature of the magnetic field (b) along a field line for the base case ($\delta = 0$) (purple), $\delta = -0.25$ (yellow), $\delta = -0.5$ (dark blue), and $\delta = -0.75$ (red).	29
4.7	Quasilinear heat flux using growth rates for $k_y\rho_s \leq 2$ for the base case ($\kappa = 1$), $\kappa = 1.5$, $\kappa = 2$, and $\kappa = 2.5$	31
4.8	Cumulative quasilinear heat flux contribution as a function of $k_y\rho_s$ for $\kappa = 1.5$ (green), $\kappa = 2$ (light blue), and $\kappa = 2.5$ (orange).	31
4.9	Quasilinear heat flux for the base case ($\delta = 0$), $\delta = \pm 0.25$, $\delta = \pm 0.5$, and $\delta = \pm 0.75$	32
5.1	Time trace of nonlinear heat flux for the base case with $nz0 = 32$, $k_y^{\min} = 0.05$ (purple) and $nz0 = 64$, $k_y^{\min} = 0.05$ (green) showing the base case converged in the parallel spatial direction. Also the incomplete run of the base case with $nz0 = 32$, $k_y^{\min} = 0.025$ (yellow) is shown to illustrate convergence is likely.	35

5.2	Heat flux spectra in k_x (a) and k_y (b) for the base case with $k_y^{\min} = 0.05$ (green) and $k_y^{\min} = 0.025$ (purple). With more resolution in k_x - k_y space, the maximum $\langle Q_{es} \rangle$ decreases, because the nonlinear heat flux contributions from each mode were divided into more bins in the finer resolution simulation ($k_y^{\min} = 0.025$).	36
5.3	Radial correlation coefficient of Φ with itself without zonal modes for the base case $k_y^{\min} = 0.05$. The horizontal dashed line denotes the half correlation length and the vertical dashed line denotes correlation coefficient at the half correlation length.	36
5.4	Heat flux spectra in k_x (a) and k_y (b) for the base case (purple) and $\kappa = 1.5$ (green).	37
5.5	Time trace of nonlinear heat flux for $\kappa = 1.5$ with $nz0 = 64, nv0 = 32$ (purple) and $nz0 = 128, nv0 = 32$ (green), and $nz0 = 64, nv0 = 64$ (yellow). The incomplete simulation using $nz0 = 64, nv0 = 128$ (red) is included to show the parallel velocity space is likely close to convergence.	38
5.6	Radial correlation coefficient of Φ with itself without zonal modes for $\kappa = 1.5$ with $k_y^{\min} = 0.05$. The horizontal dashed line denotes the half correlation length and the vertical dashed line denotes correlation coefficient at the half correlation length.	38
5.7	Heat flux spectra for negative triangularity geometries in k_x (a) and k_y (b) for the base case (purple), $\delta = -0.25$ (yellow), $\delta = -0.5$ (dark blue), and $\delta = -0.75$ (red), and for positive triangularity geometries in k_x (c) and k_y (d) for the base case (purple), $\delta = 0.25$ (green), $\delta = 0.5$ (light blue), and $\delta = 0.75$ (orange). Because the nonlinear heat flux is much smaller, separate figures are shown for the k_x (e) and k_y (f) spectra for $\delta = 0.75$	40
5.8	Time trace of nonlinear heat flux for $\delta = 0.25$ with $nz0 = 64$ (purple) and $nz0 = 128$ (green) to illustrate convergence in the parallel spatial resolution.	41
5.9	Time trace of nonlinear heat flux for $\delta = 0.5$ with $nz0 = 64$ (purple) and $nz0 = 128$ (green) to show the relative insensitivity to parallel spatial resolution and large quasi-periodic change in nonlinear heat flux.	42
5.10	Time trace of nonlinear heat flux for $\delta = 0.75$ with $nz0 = 64, nv0 = 32$ (purple) and $nz0 = 128, nv0 = 32$ (green), and $nz0 = 64, nv0 = 64$ (yellow). For $nz0 = 64, nv0 = 32$, the saturated state begins at about $t/(c_s/R_0) = 2000$, and the saturated state for $nz0 = 128, nv0 = 32$ begins around $t/(c_s/R_0) = 400$	42
5.11	Time trace of nonlinear heat flux for $\delta = -0.25$ with $nz0 = 32$ (purple) and $nz0 = 64$ (green), $nz0 = 128$ (yellow) is shown to illustrate the relative insensitivity to parallel spatial resolution and large quasi-periodic change in nonlinear heat flux.	43
5.12	Time trace of nonlinear heat flux for $\delta = -0.5$ with $nz0 = 64, nv0 = 32$ (purple) and $nz0 = 128, nv0 = 32$ (green), is shown to illustrate convergence in the parallel spatial resolution. The simulations for $nz0 = 64, nv0 = 64$ (yellow) and $nz0 = 64, nv0 = 128$ (red) are plotted to show a higher parallel velocity resolution is needed.	44

5.13	Time trace of nonlinear heat flux for $\delta = -0.75$ with $nz0 = 64, nv0 = 32$ (purple) and $nz0 = 128, nv0 = 32$ (green), is shown to illustrate convergence in the parallel spatial resolution. The simulation for $nz0 = 64, nv0 = 64$ (yellow) is also plotted to show the simulation likely converged for the parallel velocity.	44
5.14	Radial correlation coefficient of Φ with itself without zonal modes for (a) $\delta = 0.25$, (c) $\delta = 0.5$, (e) $\delta = 0.75$, (b) $\delta = -0.25$, (d) $\delta = -0.5$, (f) $\delta = -0.75$. The horizontal dashed line denotes the half correlation length and the vertical dashed line denotes correlation coefficient at the half correlation length.	45
5.15	Quasilinear and nonlinear heat fluxes varying triangularity from Table 5.1. All nonlinear heat fluxes were likely close to the converged values except $\delta = -0.5$, which, from Figure 5.12, is probably closer to five.	47
5.16	Contours of Φ for the base case (a) and $\kappa = 1.5$ (b) taken at the last time step of the simulation.	48
5.17	Time traces of the magnitude of electrostatic potential of several zonal and nonzonal modes for nonlinear simulations of (a) the base case, (b) $\kappa = 1.5$. The modes are denoted with (k_x, k_y) where zonal modes have $k_x \neq 0, k_y = 0$. Each subfigure depicts the same sized time domains and range of $ \Phi $ values.	49
5.18	Time traces of the magnitude of electrostatic potential of several zonal and nonzonal modes for nonlinear simulations of (a) $\delta = 0.25$, (b) $\delta = -0.25$, (c) $\delta = 0.5$, (d) $\delta = -0.5$, (e) $\delta = 0.75$, and (f) $\delta = -0.75$. The modes are denoted with (k_x, k_y) where zonal modes have $k_x \neq 0, k_y = 0$. Each subfigure depicts the same sized time domain and range of $ \Phi $ values.	51

Abstract

Driven by the renewed interest in optimizing a stellarator to reduce ITG turbulence and the success of changing flux surface shaping in advanced tokamaks to control plasma behaviors for a variety of scales, there is interest in how tokamak shaping affects ITG turbulence. In this thesis, the changes in linear and nonlinear properties of ITG turbulence from independent variation of triangularity and elongation for a single axisymmetric flux surface away from a circular base case were studied. Each flux surface is described and its properties computed with local MHD equilibrium theory using the `NE3DLE` code. The turbulence properties of each flux surface was then investigated using the gyrokinetics code `GENE`.

A linear stability analysis of flux surfaces with a large range of values for elongation and triangularity was performed. A comparison of trends in linear growth rates to trends in the curvature of magnetic field lines as shaping was varied was also performed. The trends in curvature correlated with the decrease in linear growth rates at low k_y and the decrease in quasilinear heat flux values with increasing elongation. For the cases $\delta = 0.5$ and $\delta = 0.75$, the curvature trends correlated with linear growth rate trends at low k_y , but there was less correlation between curvature and linear growth rates at low k_y with increasing negative triangularity. Additionally, the quasilinear heat flux decreased with both increasing positive and negative triangularity, with positive triangularity having a stronger effect.

In addition, the first computations of nonlinear heat fluxes and the first comparisons between nonlinear and quasilinear heat fluxes for various tokamak shaping were performed. Despite incomplete numerical convergence in nonlinear heat flux for any shaping, evidence was provided that all but one of the geometries likely had nonlinear heat fluxes similar to what the converged value will be. The exception was the case $\delta = -0.5$. The only elongated geometry simulated nonlinearly was $\kappa = 1.5$, where the nonlinear heat flux was larger than the nonlinear heat flux for base case, disagreeing with quasilinear heat flux trends for elongation. The increase in nonlinear heat flux for $\kappa = 1.5$ compared to the base case correlated with an increase in radial elongations in the contours of electrostatic potential and decreased zonal mode strength at higher k_x . With the exception of $\delta = -0.5$, nonlinear heat flux trends in triangularity agreed qualitatively with the corresponding quasilinear heat flux trends. However, qualitatively, the nonlinear heat fluxes were typically significantly less than quasilinear heat fluxes, and the trend in nonlinear heat fluxes with triangularity did not correlate with increasing zonal mode amplitudes. The case $\delta = 0.75$ had a nonlinear heat flux of nearly zero, but there is circumstantial evidence this case may be in a Dimits region, potentially explaining the unusually low nonlinear heat flux for this case.

1 Introduction

The purpose of this section is to provide motivation for and background of studying turbulence in fusion devices with toroidal geometry. This section will introduce nuclear fusion and basic plasma physics concepts necessary to study turbulence in toroidal devices.

1.1 Fusion Energy

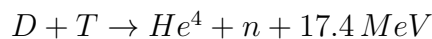
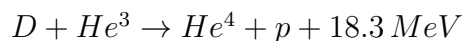
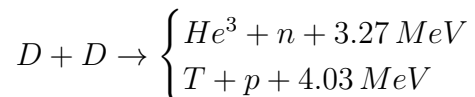
As civilization progresses over time, the energy requirements to drive development continues to increase. Estimates suggest by 2040 world energy consumption will increase by 28%, with fossil fuels poised to continue as the dominant source of energy [1]. The problem with continuing the trend of fossil fuel reliance is twofold. First, extracting energy from fossil fuels produces byproducts harmful to the climate in significant amounts. Extraction of energy from fossil fuels relies on combustion, producing carbon dioxide and nitrous oxide, which creates a greenhouse effect; if unchecked, the greenhouse effect would render the Earth uninhabitable. For civilization to continue and progress, a new source of energy without harmful byproducts must replace fossil fuels. Second, the world's supply of fossil fuels finite. World reserves of fossil fuels are estimated to be on the order of a hundred years [2]. Once fossil fuel reserves are depleted, a new primary source of energy will be needed to replace the void left by fossil fuels.

A promising alternative energy source to fossil fuels is the binding energy of an atomic nucleus. The binding energy of a nucleus is a result of a fundamental force called the strong nuclear force. There are two ways of using the strong nuclear force as an energy source. One method is through nuclear fission—the splitting of one heavy nucleus into two smaller nuclei. While nuclear fission is effectively employed as an energy source, the fission reaction produces dangerously radioactive waste, which maintains its radioactive properties for tens of thousands of years. The level and lifetime of radioactive waste produced by fission raises health and environmental concerns over waste disposal and containment.

Another method of harnessing the binding energy of a nucleus is through the fusion process. *Nuclear fusion* is the process of fusing two smaller nuclei into one larger nuclei. Nuclear fusion has two clear advantages over fission: little radioactive waste and a substantially higher energy density per reaction [3]. However, achieving nuclear fusion has proved difficult. To fuse two nuclei together, the strong nuclear force must be the dominant force. Because the strong nuclear force is dominant at short distances, the fusing nuclei must overcome the repulsive barrier of Coulomb forces. To overcome the Coulomb forces, the nuclei must collide with substantial velocities. To produce reactor-scale energy, a large portion of the fusion fuel must have substantial velocities, which requires temperatures over 100 million degrees Celsius [4]. These temperatures are well above ionization energies, putting the fusion reactants and products in the *plasma* state. Plasmas are more complex than neutral gasses, because ionization creates a soup of charged ions and electrons, introducing Coulomb interactions between plasma particles. Due to the charged nature of a plasma's constituents, plasmas can be influenced by internal and external electromagnetic forces, creating a system of richly complex behaviors. One of the complex behaviors, turbulence, is a focus of this thesis.

1.2 Magnetic Confinement Fusion

There are several reactions that make good candidates for nuclear fusion. One potential reaction to use is the deuterium-deuterium (D-D) reaction. Deuterium is an isotope of hydrogen with a nucleus comprising one proton and one neutron. The products of the D-D reaction can either be a helium-3, a helium isotope with one neutron, and a neutron or a tritium (a hydrogen isotope with two neutrons) and a proton. Another candidate is the deuterium-helium-3 (D-He³) reaction. The D-He³ reaction produces an α particle (a twice-ionized helium-4) and a proton. The most promising reaction is the deuterium-tritium (D-T) reaction, which produces an α particle and a neutron.



The D-T reaction has a much larger collisional cross-section occurring at lower thermal energies than the D-D and D-He³ reactions, as seen in Figure 1.1 [4]. This means the D-T reaction will happen more frequently generating more power than the D-D and D-He³ reactions. Because the D-T cross-section peaks at a lower temperature, additional physics and engineering challenges regarding heating are less substantial. With the largest cross-section at a lower temperature, the D-T reaction is the most promising choice for a fusion reactor.

Because plasmas react to external and internal electromagnetic forces, a fusion device

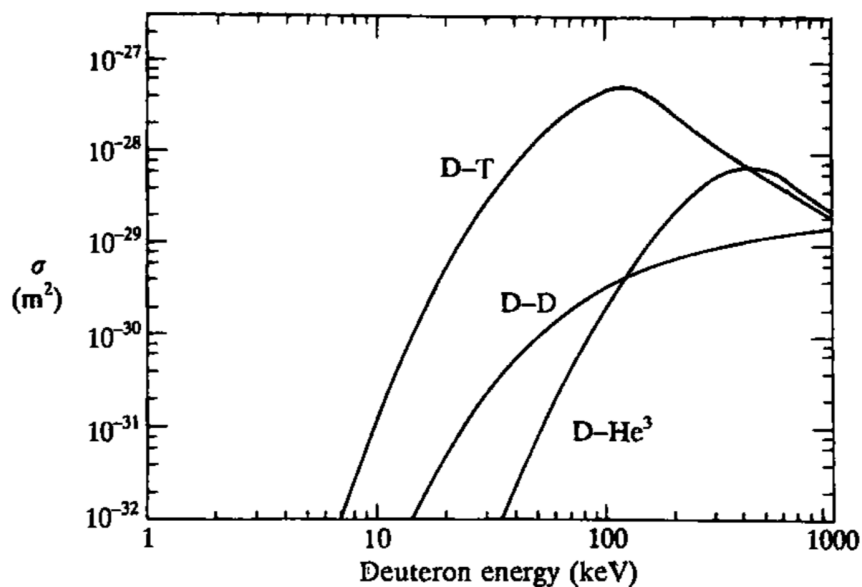


Figure 1.1: Reaction cross sections for the D-D, D-He³, and D-T fusion reactions as a function of thermal energy [4].

could use magnetic fields to confine the plasma, a scheme known as *magnetic confinement fusion*. Comprised of ionized particles, plasmas obey *Maxwell's Equations*,

$$\nabla \cdot \mathbf{E} = \frac{\rho_t}{\epsilon_0} \quad (1.1)$$

$$\nabla \times \mathbf{E} = -\frac{\partial \mathbf{B}}{\partial t} \quad (1.2)$$

$$\nabla \cdot \mathbf{B} = 0 \quad (1.3)$$

$$\nabla \times \mathbf{B} = \mu_0 \mathbf{J}_t + \frac{1}{c} \frac{\partial \mathbf{E}}{\partial t}, \quad (1.4)$$

where c is the speed of light in a vacuum, ϵ_0 is the vacuum permittivity, μ_0 is the vacuum permeability, and $\rho_t = \rho_{\text{external}} + \rho_{\text{plasma}}$ and $\mathbf{J}_t = \mathbf{J}_{\text{external}} + \mathbf{J}_{\text{plasma}}$ are the total charge density and total current density of the system, respectively. To describe ρ_{plasma} and $\mathbf{J}_{\text{plasma}}$, a statistical treatment is required, because plasmas typically have a large number of particles. A *distribution function* of a species s is defined as the number of particles per unit volume of the six dimensional phase space [4]. Mathematically, the distribution function is written as

$$\int f_s(\mathbf{x}, \mathbf{v}, t) d\mathbf{x} d\mathbf{v} = N_s, \quad (1.5)$$

where N_s is the total number of particles of the species. Now, the plasma charge density and current density are defined as

$$\rho_{\text{plasma}} = \sum_s q_s \int f_s(\mathbf{x}, \mathbf{v}, t) d\mathbf{v} = \sum_s q_s n_s \quad (1.6)$$

and

$$\mathbf{J}_{\text{plasma}} = \sum_s q_s \int \mathbf{v} f_s(\mathbf{x}, \mathbf{v}, t) d\mathbf{v} = \sum_s q_s n_s \mathbf{V}_s, \quad (1.7)$$

where $n_s = \int f_s(\mathbf{x}, \mathbf{v}, t) d\mathbf{v}$ is the plasma density and $\mathbf{V}_s = \int \mathbf{v} f_s(\mathbf{x}, \mathbf{v}, t) d\mathbf{v} / n_s$ is the mean velocity of a species s .

With a distribution function defined, the kinetic behavior of plasmas can be described using the *Fokker-Plank Equation*:

$$\frac{\partial f_s}{\partial t} + \mathbf{v} \cdot \frac{\partial f_s}{\partial \mathbf{x}} + \frac{q_s}{m_s} (\mathbf{E} + \mathbf{v} \times \mathbf{B}) \cdot \frac{\partial f_s}{\partial \mathbf{v}} = \mathcal{C}(f_s) + \mathcal{S} - \mathcal{D}. \quad (1.8)$$

The Coulomb operator $\mathcal{C}(f_s)$ describes the effects Coulomb collisions have on f_s over time, the source term \mathcal{S} represents adding species through processes such as ionization, and the sink term \mathcal{D} accounts for the loss of species through processes like atomic recombination. However, a conservative, collisionless form of Equation (1.8) is often used. The collisionless approximation can be motivated, because collision frequency decreases with increasing plasma thermal velocity with the scaling $\nu \propto v_{th,s}^{-3}$, where $v_{th,s} = \sqrt{2T_s/m_s}$. Temperatures where fusion cross-sections are maximized are high enough for the plasma to be considered collisionless. The conservative, collisionless kinetic equation is called the *Vlasov Equation*:

$$\frac{\partial f_s}{\partial t} + \mathbf{v} \cdot \frac{\partial f_s}{\partial \mathbf{x}} + \frac{q_s}{m_s} (\mathbf{E} + \mathbf{v} \times \mathbf{B}) \cdot \frac{\partial f_s}{\partial \mathbf{v}} = 0. \quad (1.9)$$

Analytically solving Equation (1.9) is nontrivial and only possible for certain idealized systems, because there are nonlinear interactions between \mathbf{E} , \mathbf{B} , and the plasma. The nonlinearities arise in the third term of Equation (1.9), which have the form $\mathbf{E}f \sim f^2$, because $\mathbf{E} \sim f$ from Equations (1.1) and (1.6) and $\mathbf{B} \sim \mathbf{E}/c$ from Equations (1.4) and (1.7). The nonlinearities in Equation (1.9) give rise to complex plasma behaviors, including turbulence. To model the nonlinear behavior of the solutions to Equation (1.9), a wealth of numerical tools have been developed and implemented, as has been done in this thesis.

1.2.1 Single Particle Drifts

The velocity of a single ionized plasma particle, \mathbf{v} , also reacts to the Coulomb and Lorenz forces:

$$\frac{d\mathbf{v}}{dt} = \frac{q_s}{m_s}(\mathbf{E} + \mathbf{v} \times \mathbf{B}), \quad (1.10)$$

where q_s and m_s is the charge and mass of a particle species, s , respectively. The Lorenz force confines plasma particles perpendicularly to magnetic field lines with a *gyroradius* $\rho_{L,s} = m_s v_{\perp} / q_s B$, where v_{\perp} is the magnitude of the particle's velocity perpendicular to the magnetic field line. However, along the magnetic field lines, plasma particles are unrestricted, resulting in the particle moving in a helical motion parallel to the magnetic field lines. This led to high “streaming losses” in early linear fusion devices, such as the magnetic mirror and pinch configurations. Streaming losses can be eliminated by “attaching” the ends in a toroidal geometry (Figure 1.2). While toroidal geometry eliminates streaming losses, it also adds complexity to the fusion problem.

Toroidal geometry of magnetic fields adds physics of single particle drifts that can complicate to plasma confinement. The toroidal magnetic field in a toroidal system manifestly has finite curvature. This nonzero curvature induces centrifugal forces on particles moving along the magnetic field lines, resulting the the following curvature drift velocity:

$$\mathbf{v}_c = \frac{v_{\parallel}^2}{\Omega_s} \frac{\mathbf{B} \times \boldsymbol{\kappa}}{B}, \quad (1.11)$$

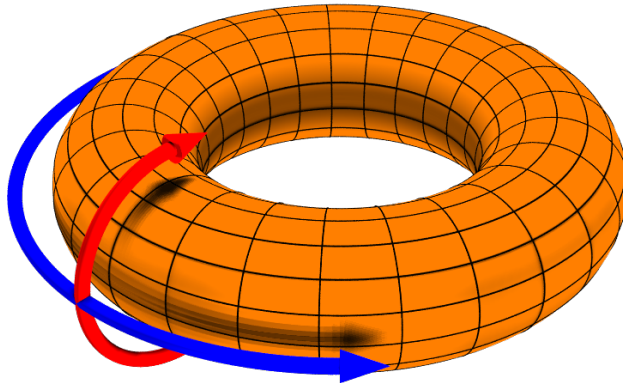


Figure 1.2: Toroidal (blue) and poloidal (red) directions on a torus [5].

where $\Omega_s = q_s B / m_s$ is the frequency at which the particle gyrates around the magnetic field line (referred to as the *gyrofrequency*), v_{\parallel} is the magnitude of the particle's velocity parallel to the magnetic field line, and $\boldsymbol{\kappa} = (\hat{\mathbf{b}} \cdot \nabla) \hat{\mathbf{b}}$ is the curvature of the magnetic field line, with $\hat{\mathbf{b}} = \mathbf{B} / B$. The finite curvature of the toroidal magnetic field also implies a nonzero gradient in the magnetic field, which drops off with a $1/R$ dependence, where R is the radius from the toroidal axis. A gyrating particle in a heterogenous magnetic field experiences an imbalance in forces over a complete orbit about the field line, resulting in the *guiding center* drifting away from its original position. The movement of the guiding center of a particle due to a magnetic field gradient, called the “ ∇B ” drift, is quantified in the following equation:

$$\mathbf{v}_{\nabla B} = \frac{v_{\perp}^2}{2\Omega_s} \frac{\mathbf{B} \times \nabla B}{B^2}. \quad (1.12)$$

Additionally, in a toroidal system magnetic field lines have a nonzero curvature in general. Another drift is present when there is an electric field, \mathbf{E} :

$$\mathbf{v}_{\mathbf{E} \times \mathbf{B}} = \frac{\mathbf{E} \times \mathbf{B}}{B}, \quad (1.13)$$

called the “ $\mathbf{E} \times \mathbf{B}$ ” drift. Assuming only a toroidal field, the ∇B and curvature drifts are vertical and opposite for ions and electrons. The resultant charge separation creates a downward vertical electric field, stimulating an $\mathbf{E} \times \mathbf{B}$ drift outward radially, losing confinement. Hence, a poloidal magnetic field must be added to contain particle drifts.

1.2.2 MHD Equilibrium

Magnetic confinement requires the confinement and isolation of hot plasmas from the external structure, where the macroscopic force balance is described by the *magnetohydrodynamics* (MHD) model. MHD treats the plasma as a single magnetized fluid and is a model used to study plasmas that are collisional enough for a fluid theory to be valid on length scales greater than the ion gyroradius. The magnetized fluid has a mass density $\rho = \sum_s m_s n_s$ and velocity $\mathbf{V} = (\sum_s m_s n_s \mathbf{v}_s) / \rho$. Ideal MHD neglects plasma resistivity and viscosity and assumes isotropic pressure while still capturing important physical phenomena central to MHD theory. The 11 nonlinear partial differential equations describing ideal MHD are as follows:

$$\frac{\partial \rho}{\partial t} + \nabla \cdot (\rho \mathbf{V}) = 0 \quad (1.14)$$

$$\rho \left(\frac{\partial \mathbf{V}}{\partial t} + (\mathbf{V} \cdot \nabla) \mathbf{V} \right) = \mathbf{J} \times \mathbf{B} - \nabla p \quad (1.15)$$

$$\frac{d}{dt} \left(\frac{p}{\rho^\gamma} \right) = 0 \quad (1.16)$$

$$\frac{\partial \mathbf{B}}{\partial t} = \nabla \times (\mathbf{V} \times \mathbf{B}) \quad (1.17)$$

$$\mu_0 \mathbf{J} = \nabla \times \mathbf{B} \quad (1.18)$$

with the natural constraint on magnetic fields in Equation (1.3). In the MHD limit, light waves are not resolved, and the $\partial \mathbf{E} / \partial t$ term is dropped from Equation (1.4) for Equation (1.18). Here, $\mathbf{J} = \sum_s q_s n_s \mathbf{v}_s$ is the plasma current, p is an isotropic pressure, and $\gamma = 1 + 2/N$ is an adiabatic index with N degrees of freedom.

A desirable quality for a reactor is to be able operate at steady state, which can be modeled using a static ideal MHD equilibrium. Equilibrium means all quantities do not evolve in time ($\partial / \partial t = 0$), and static means the fluid velocity is zero, reducing the description of the plasma using Equations (1.14) to (1.17) to a force balance of

$$\mathbf{J} \times \mathbf{B} = \nabla p. \quad (1.19)$$

From Equation (1.19), it is immediately clear that plasma current and magnetic field lines lie on surfaces of constant pressure; the application this property is discussed in Section 2.

1.2.3 Toroidal Configurations

As mentioned in Section 1.2.1, to achieve confinement, a poloidal field is needed, which can be provided by different toroidal configurations. The *stellarator* configuration, relies on richly shaped external magnetic coils to produce a poloidal magnetic field. An example of a stellarator with 3D shaping is shown in Figure 1.3a, where the coils are blue and a surface of constant magnetic flux in the plasma is yellow. Despite not having externally driven current, stellarators still see currents to balance forces in Equation (1.19). The plasma currents appearing from the force balance have a component parallel to the magnetic field arising from *quasineutrality* of a plasma, $\nabla \cdot \mathbf{J} = 0$. These parallel currents can be reduced such that the stellarator is MHD stable, meaning no plasma behavior described by the MHD model will disrupt confinement. However, the complexity of shaping needed for the magnetic coils breaks *axisymmetry* (magnetic symmetry about the toroidal angle), introducing engineering and theoretical difficulties. Namely, the magnetic coils of a stellarator require low tolerances and difficult to manufacture shapes. From a theory standpoint, there are no analytical MHD equilibrium solutions in a general three-dimensional (3D) magnetic field geometry, forcing

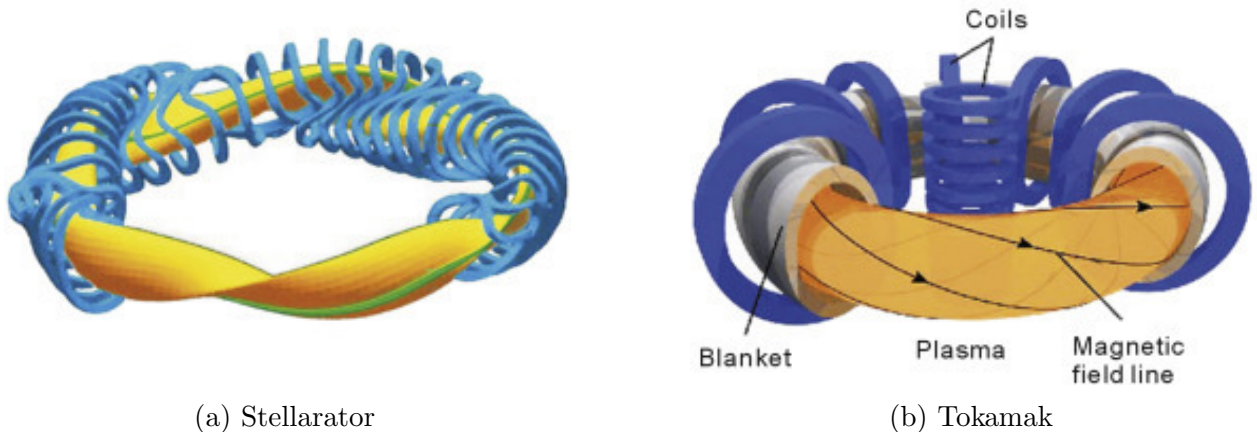


Figure 1.3: Example of a stellarator (a) and a tokamak (b) where the coils are blue and a surface of constant magnetic flux in the plasma is yellow [6].

a dependence on expensive numerical computations to find MHD solutions for stellarators. Despite a lack of analytical MHD equilibrium solutions for stellarators, the rich 3D shaping allows for the possibility of optimizing a stellarator. Specifically, optimizing a stellarator to reduce turbulence is a major area of ongoing research [7].

In contrast to stellarators, the *tokamak* configuration uses a driven current to create the poloidal magnetic field. Tokamaks use current in simply poloidally closed magnetic coils to produce the toroidal magnetic field. Present-day tokamaks rely on ohmic heating, radio frequency (RF) heating, or internal bootstrap current as a source for the poloidal field [4]. The large amount of current driven acts as a source of free energy, giving rise to MHD instabilities. MHD instabilities can significantly reduce or even completely disrupt confinement, putting constraints on tokamak operation. Despite MHD operational constraints, tokamaks are one of the most common toroidal configurations [4]. However, one of the advantages of the tokamak is its axisymmetry. Axisymmetry is an advantageous feature for engineering, because magnetic coil designs can be simple in contrast to stellarator coils. Even with axisymmetric simplifications, tokamaks still have a large two-dimensional (2D) parameter space, which has been used to improve MHD stability in the advanced tokamak scenario [8]. An example of a tokamak with a slightly elongated cross section is shown in Figure 1.3b, with a surface of constant magnetic flux depicted in yellow and the coils in blue. Like the stellarator, the 2D parameter space of a tokamak also provides the opportunity to study turbulence in various shaped tokamak scenarios.

1.3 Ion Temperature Gradient Drift Waves

When particles drift in a nonuniform plasma, ion and electron motion can produce *drift waves*. When coupled with other nonuniformities, such as temperature gradients, drift waves may become less stable and may result in significant degradation of plasma confinement. Drift waves are on the scale of a gyroradius, and, when unstable, are classified as a *microinstability*. Unstable drift waves are believed to be a significant source of heat and particle loss in tokamaks, despite manifesting on a small scales [9]. The *ion temperature gradient* (ITG) mode drift wave instability will be the main focus of this section.

To illustrate an instability from an ion temperature gradient, a nonhomogeneous plasma with a slab geometry will be considered. Suppose the magnetic field is in the z -direction, and the magnetic field, pressure, and ion temperature gradients in the negative x -direction (Figure 1.4). The ∇B drift for the ions(electrons) is in the negative(positive) y -direction, but the hotter ions drift faster than the colder ions, creating multiple charge separations in space. The charge separation induces a spatially varying electric field in the y -direction, giving rise to an $\mathbf{E} \times \mathbf{B}$ drift in the x -direction, reversing spatially in the y -direction, which can enhance the charge separation and therefore a drift growing for all time.

The stability of a drift wave in the presence of an ion temperature gradient in a toroidal geometry depends on many factors. In addition to the ion temperature gradient, density gradients play a role by shifting the phase of the wave such that the $\mathbf{E} \times \mathbf{B}$ drift may stabilize or destabilize the electrostatic perturbation. Another factor influencing drift wave stability is magnetic field curvature. More curvature increases charge separation, and the direction of curvature has a profound effect on stability. For instance, in Figure 1.4, if

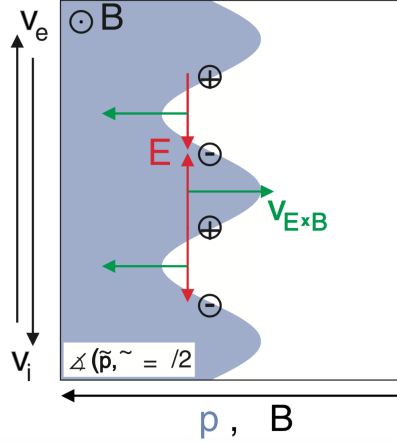


Figure 1.4: Illustration of an ITG instability in a nonhomogeneous plasma with a slab geometry. A temperature gradient in the negative x -direction is represented by hotter ions in blue and colder ions in white. The magnetic field is in the z -direction out of the page with the pressure and magnetic field gradients in the negative x -direction [10].

the direction of curvature (i.e. ∇B) reversed, a similar analysis as the previous paragraph finds $\mathbf{E} \times \mathbf{B}$ drift damps the initial perturbation. Further, with temperature and density gradients, pressure gradients arise. Pressure gradients are known to have a stabilizing effect if antiparallel to the curvature and a destabilizing effect if parallel to the curvature. There are a variety of other destabilizing or stabilizing mechanisms (e.g. magnetic shear), complicating the problem of drift wave stability. The work done in this thesis emphasizes the effects of curvature on ITG modes in Section 4.

1.4 Turbulence

Plasma turbulence is a broad area of research, encompassing multiple distinct phenomena. In general, turbulence in plasmas (and nonmagnetized fluids as well) is the unpredictable evolution of motion and nonlinear interactions over a range of length scales. As mentioned previously, ITG turbulence is believed to be a significant source confinement loss in tokamaks [9], however the mechanisms of ITG turbulence (and turbulence in general) are not fully understood. This section will introduce the concept of one turbulence mechanism used in this thesis, saturation.

For a plasma to achieve a steady state required for a working fusion reactor, the energy dissipated in a turbulent flow must be equal to the energy transferred to the turbulent flow from a free energy source, a process called *turbulent saturation*. For ITG turbulence, gradients of profile quantities, such as pressure, provide a source of free energy. Free energy sources drive instabilities, which can cause instability-driven turbulence. However modes with negative growth rates, called *stable modes*, exist simultaneously with *unstable modes*. The nonlinear interactions in turbulence allows unstable modes to excite stable modes to a finite amplitude. The stable modes then decay in time, dissipating the energy transferred by the unstable modes [11]. Although the mechanism of turbulent saturation is not the primary focus, the region of turbulent saturation is studied in this thesis.

1.5 Thesis Outline

The succeeding sections of this thesis are as follows. Section 2 will address the concept of local equilibrium. Magnetic coordinates will be introduced, which are a vital tool in local equilibrium theory. A methodology for solving 3D local equilibria is described, and a prescription of axisymmetric shaping for local equilibria, called the Miller equilibrium, is also described. Section 3 will describe how gyrokinetic simulations are used in turbulence studies. A brief description of gyrokinetic theory is discussed to introduce the Gyrokinetic Electromagnetic Numerical Experiment (GENE) code. Previous turbulence studies on the effects of tokamak shaping will be discussed in Section 3 as well. Section 4 compares the linear growth rates across a wave number spectrum with varying shaping parameters using adiabatic electrons with the curvatures of each configuration. Additionally, the quasilinear heat flux is computed for each geometry using the ITG growth rates. Section 5 presents results of nonlinear GENE calculations and compares the nonlinear heat fluxes with quasilinear heat fluxes. This thesis ends with Section 6, a summary of the results of this thesis and a description of possible future research directions from this work.

2 Magnetic Flux Surfaces

The toroidal geometry of magnetic fields used in magnetic confinement fusion can be shaped to achieve desired plasma behavior. The purpose of this section is to introduce the concept of and the tools used to describe the shaping of flux surfaces. Magnetic coordinates will be introduced as a mathematical framework, constructed to have advantageous properties for describing toroidal magnetic fields. Then, local equilibrium theory will be introduced and motivated, beginning with the shaped axisymmetric local equilibrium known as the Miller equilibrium, then moving onto a generalized 3D local equilibrium. Finally, the numerical implementation of the 3D equilibrium procedure in NE3DLE is discussed.

2.1 Magnetic Coordinates

When working with a simple torus, it follows that one should use a cylindrical coordinate system (R, ϕ, Z) or a toroidal-like coordinate system (r, θ, ϕ) (Figure 2.1). The cylindrical coordinate system is mapped to the toroidal-like coordinate system with the mapping

$$\begin{aligned} R &= R_0 + r \cos \theta \\ \phi &= \phi \\ Z &= r \sin \theta, \end{aligned} \tag{2.1}$$

where R_0 is the major radius, $r \in [0, a]$ with a as the minor radius of the torus, θ is the *geometric poloidal angle*, and ϕ is the *geometric toroidal angle*. The aspect ratio in Figure 2.1 for a device is R_0/a .

In Figure 2.1 the *radial coordinate* is r , which is not the case in general. From Equation (1.19), it is obvious that magnetic field lines and currents lie on a surface normal to ∇p . Therefore, pressure can be used as a radial coordinate in MHD equilibrium. Because magnetic field lines are tangent to the surfaces of constant pressure, both toroidal and poloidal magnetic flux,

$$\psi_{tor} = \int \mathbf{B} \cdot d\mathbf{S}_{tor} \tag{2.2}$$

$$\psi_{pol} = \int \mathbf{B} \cdot d\mathbf{S}_{pol}, \tag{2.3}$$

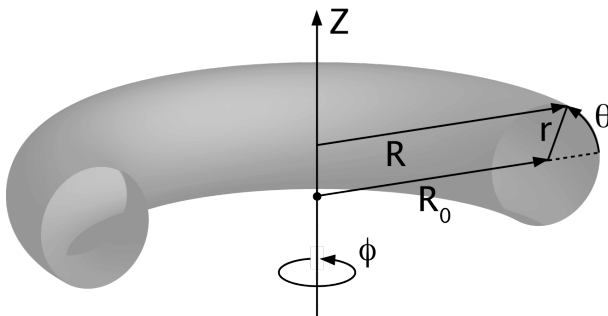


Figure 2.1: The cylindrical and toroidal-like coordinate system [12].

are conserved, and surfaces of constant pressure are also surfaces of constant magnetic flux, termed *flux surfaces*. Therefore, magnetic flux can be used as a radial coordinate.

While the toroidal-like coordinate system may work for a simple torus, to describe MHD equilibrium with more generality, a curvilinear coordinate system called *magnetic coordinates* are used. For a thorough treatment of magnetic coordinates, see [13]. In magnetic coordinates, a magnetic field line is a straight line in $\Theta - \zeta$ space, where Θ is a poloidal angle and $\zeta = -\phi$ is a toroidal angle. The straight field line angles are related through a *field line label*:

$$\alpha = \Theta - \iota\zeta. \quad (2.4)$$

which is constant along a field line. The *rotational transform*, ι , is the rate at which field lines progress poloidally with respect to the toroidal progression:

$$\iota = \frac{d\Theta}{d\zeta} = \frac{\mathbf{B} \cdot \nabla\Theta}{\mathbf{B} \cdot \nabla\zeta} = \frac{1}{q}, \quad (2.5)$$

where q is the *safety factor*. A convenience of straight field line coordinates is the rotational transform (and, by extension, the safety factor) is a flux function: $\iota = \iota(\psi)$. Choosing a magnetic flux as the flux surface label, the magnetic field can be written in Clebsch form with the field line label:

$$\mathbf{B} = \nabla\psi \times \nabla\alpha. \quad (2.6)$$

One should be aware that although ζ is the geometric toroidal angle, Θ is not the the geometric poloidal angle, θ . The relationship between Θ and θ is needed to translate flux surface shaping in real geometry to magnetic coordinates, which will be discussed in Section 2.2.2.

2.2 Local Equilibrium

It is widely accepted changing the cross-sectional shaping of the flux surfaces in axisymmetric configurations impact stability of various plasma behaviors, including ITG mode drift waves. Early MHD equilibrium theory describes MHD equilibrium of plasmas globally, most notably using the Grad-Shafranov equation for axisymmetric systems [14, 15]:

$$\Delta^*\psi = -FF' - \mu_0 R^2 p', \quad (2.7)$$

where $F(\psi) = RB_\phi$, and the elliptic derivative is defined as

$$\Delta^* = R \frac{\partial}{\partial R} \left(\frac{1}{R} \frac{\partial}{\partial R} \right) + \frac{\partial^2}{\partial Z^2}. \quad (2.8)$$

While describing a broad range of critical plasma behavior, using global equilibrium to study microinstabilities is not efficient. Now, a different approach describing a single flux surface, called a *local equilibrium*, is used to investigate microinstabilities. Axisymmetric local equilibrium models often use Equation (2.7) in their derivations as well [16, 17]. A major contribution to developing a model for shaped axisymmetric local equilibria came from Greene and Chance [16], which allowed for global magnetic shear and pressure gradient to be varied while keeping other parameters constant in what is called an $s - \alpha$ model. Miller, et al. [17] expanded the work of [16] to develop a model using the formalism developed by Mercier and

Luc [18] to describe an axisymmetric local equilibrium using plasma profile quantities, such as current, and nine shaping parameters. The work of [17] is described in Section 2.2.1. A generalized method to solve a nonaxisymmetric local equilibrium using magnetic coordinates was developed by Hegna [19] and is equivalent to [17] in the axisymmetric limit. The method described by [19] is discussed in Section 2.2.2. In Section 2.2.3 the numerical implementation of Hegna's method of solving a local equilibrium by the NE3DLE code is discussed.

2.2.1 Miller Equilibrium

To study how changes in an axisymmetric equilibrium affects localized instabilities, the Miller equilibrium [17] provides a method to independently vary plasma profile quantities and nine shaping parameters using a finite aspect ratio, noncircular model. The Miller equilibrium uses the Mercier-Luc formalism [18] to specify a local equilibrium at a flux surface $\psi = \psi_0$ in cylindrical coordinates using three steps: (1) define the flux surface shaping, $R(l), Z(l)$; (2) define the poloidal field, $B_p(l)$; (3) define profile quantities $p'(\psi_0)$ and $FF'(\psi_0)$ from Equation (2.7), where $l = l(\theta)$ is the poloidal arc length. These three steps can be satisfied by specifying the nine dimensionless shaping parameters: elongation (κ), triangularity (δ), the variations of κ , δ , and major radius with the flux surface (s_κ , s_δ , and $\partial_r R_0$, respectively), global magnetic shear (s), pressure gradient (α), safety factor (q), and aspect ratio (A).

The flux surface shaping is given by R and Z :

$$R = R_0 + r \cos(\theta + (\arcsin \delta) \sin \theta) \quad (2.9)$$

$$Z = \kappa r \sin \theta. \quad (2.10)$$

The poloidal field is given by the following:

$$B_p = \frac{\partial_r \psi [\sin^2(\theta + x \sin \theta)(1 + x \cos \theta)^2 + \kappa^2 \cos^2 \theta]^{1/2}}{\kappa R (\cos(x \sin \theta) + \partial_r R_0 \cos \theta + [s_\kappa - s_\delta \cos \theta + (1 + s_\kappa)x \cos \theta] \sin \theta \sin(\theta + x \sin \theta))}, \quad (2.11)$$

where $\sin x = \delta$,

$$s_\kappa = \frac{r \partial_r \kappa}{\kappa}, \quad (2.12)$$

$$s_\delta = \frac{r \partial_r \delta}{(1 - \delta^2)^{1/2}}, \quad (2.13)$$

and $\partial_r \psi$ is the radial derivative of flux, which can be defined by using the definition of q ,

$$q = \frac{F}{2\pi} \int \frac{dl}{R^2 B_p} \quad (2.14)$$

through choice of the toroidal field $B_0 = F_0/R_0$ with Equation (2.11). The profile quantities $q'(\psi_0)$ and $p'(\psi_0)$ are defined using the dimensionless quantities s and α :

$$s = \frac{2Vq'}{V'} \quad (2.15)$$

$$\alpha = \frac{2V'}{4\pi^2} \left(\frac{V}{2\pi^2 R_0} \right)^{1/2} \mu_0 p'. \quad (2.16)$$

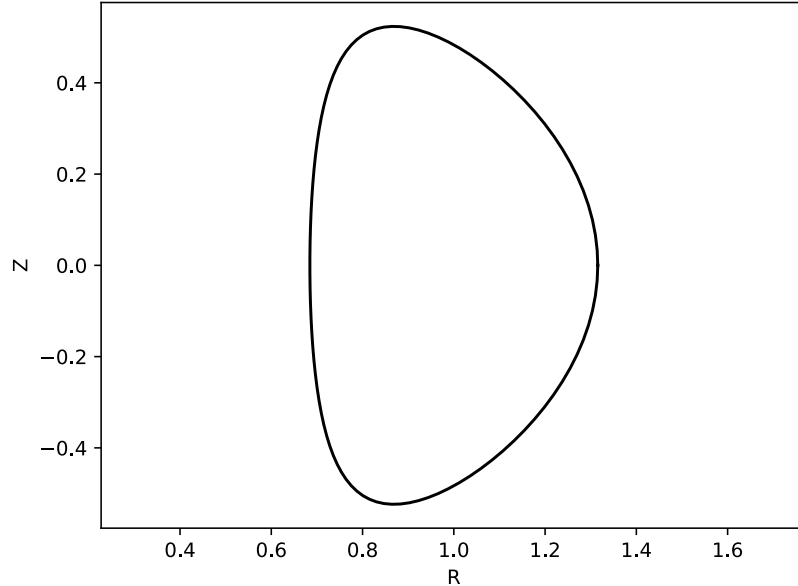


Figure 2.2: Shaped cross section of a tokamak using the Miller equilibrium [17]. The shaping for this equilibrium is prescribed by $A = 3.17$, $\kappa = 1.66$, and $\delta = 0.416$. A circular cross section corresponds to $\kappa = 1$, $\delta = 0$.

Here V is the volume enclosed by the flux surface, and $V' = dV/d\psi$. The shift in major radius with flux surface is not explicitly known, but it is known to depend on B_p , and the pressure and current profiles and has been derived for large aspect ratio elliptical surfaces [20]. As for $\partial_r \kappa$ and $\partial_r \delta$, Miller, et al. [17] use their experience with experiments and numerical calculations to approximate s_κ and s_δ as

$$s_\kappa = \frac{\kappa - 1}{\kappa} \quad (2.17)$$

$$s_\delta = \frac{\delta}{(1 - \delta^2)^{1/2}}. \quad (2.18)$$

In addition, one can conclude of the nine shaping parameters, physically, only six are independent and three (s_κ , s_δ , and $\partial_r R_0$) are dependent parameters. However, the effects of s_κ , s_δ , and $\partial_r R_0$ on the equilibrium may be studied by separating them from the other parameters. Using the Miller equilibrium, a local equilibrium is fully described by setting plasma profile quantities and nine shaping parameters.

2.2.2 Three-Dimensional Local Equilibrium

While Miller, et al. is sufficient to describe a shaped axisymmetric local equilibrium, other codes used to study ITG turbulence, such as GENE (discussed in Section 3) require inputs in magnetic coordinates, and studying stellarators requires a fully 3D equilibrium. An analytic theory for 3D local MHD equilibrium has been developed equivalent to the Miller equilibrium [17] in Section 2.2.1. The following section will introduce the steps for describing a local equilibrium in [19], where a full derivation can be found. The method

of [19] requires the specification of (1) the magnetic coordinate mapping, $\mathbf{x}(\Theta, \zeta)$ and the rotational transform ι on the magnetic surface $\psi = \psi_0$, where ψ is now the toroidal flux and (2) two of three flux functions: the pressure gradient $p'(\psi)$, the averaged parallel current $\sigma(\psi) = \mu_0 \langle \mathbf{J} \cdot \mathbf{B} \rangle / \langle B^2 \rangle$, or the flux surface averaged magnetic shear $\iota'(\psi)$. If two of the three quantities in (2) are specified, the third is determined. In the axisymmetric limit, step (1) is equivalent to steps (1) and (2) and in Section 2.2.1, and step (2) here is equivalent to step (3) in Section 2.2.1 .

The equilibrium magnetic field's geometric properties can be found using the coordinate parameterization $\mathbf{x} = \mathbf{x}(\Theta, \zeta)$ and rotational transform. The equilibrium magnetic field is defined using Equation (2.6) and curvilinear properties of the coordinate system (ψ, Θ, ζ) :

$$\mathbf{B} = \left(\frac{\partial \mathbf{x}}{\partial \zeta} + \iota \frac{\partial \mathbf{x}}{\partial \Theta} \right) \frac{1}{\sqrt{g}} \quad (2.19)$$

where the Jacobian is

$$\sqrt{g} = \frac{1}{\nabla \psi \cdot \nabla \Theta \times \nabla \zeta} = \frac{\partial \mathbf{x}}{\partial \psi} \cdot \frac{\partial \mathbf{x}}{\partial \Theta} \times \frac{\partial \mathbf{x}}{\partial \zeta}. \quad (2.20)$$

By construction of the curvilinear magnetic coordinates,

$$\nabla \psi = \left(\frac{\partial \mathbf{x}}{\partial \Theta} \times \frac{\partial \mathbf{x}}{\partial \zeta} \right) \frac{1}{\sqrt{g}}. \quad (2.21)$$

The geometric quantities are computed beginning with the unit tangent and normal vectors:

$$\hat{\mathbf{b}} = \frac{\mathbf{B}}{B} = \frac{\frac{\partial \mathbf{x}}{\partial \zeta} + \iota \frac{\partial \mathbf{x}}{\partial \Theta}}{(g_{\zeta\zeta} + 2\iota g_{\Theta\zeta} + \iota^2 g_{\Theta\Theta})^{1/2}} \quad (2.22)$$

$$\hat{\mathbf{n}} = \frac{\nabla \psi}{|\nabla \psi|} = \frac{\frac{\partial \mathbf{x}}{\partial \Theta} \times \frac{\partial \mathbf{x}}{\partial \zeta}}{(g_{\zeta\zeta} g_{\Theta\Theta} - g_{\Theta\zeta}^2)^{1/2}}, \quad (2.23)$$

where a metric element g_{ij} is defined as

$$g_{ij} = \frac{\partial \mathbf{x}}{\partial u^i} \cdot \frac{\partial \mathbf{x}}{\partial u^j}, \quad (2.24)$$

with $u^i, u^j \in \{\psi, \Theta, \zeta\}$. Taking derivatives along the magnetic field and using the unit tangent, unit normal, and unit binormal $\hat{\mathbf{b}} \times \hat{\mathbf{n}}$, the normal curvature κ_n , geodesic curvature κ_g , and normal torsion τ_n are computed:

$$\kappa_n = \hat{\mathbf{n}} \cdot (\hat{\mathbf{b}} \cdot \nabla) \hat{\mathbf{b}} \quad (2.25)$$

$$\kappa_g = (\hat{\mathbf{b}} \times \hat{\mathbf{n}}) \cdot (\hat{\mathbf{b}} \cdot \nabla) \hat{\mathbf{b}} \quad (2.26)$$

$$\tau_n = (\hat{\mathbf{b}} \times \hat{\mathbf{n}}) \cdot (\hat{\mathbf{b}} \cdot \nabla) \hat{\mathbf{n}}. \quad (2.27)$$

The three profile quantities ι' , σ , and p' are related using the geometric quantities defined

above and other current quantities. An equation for the flux surface averaged local shear relates σ and p' :

$$\iota' = \sigma \left\langle \frac{B^2}{|\nabla\psi|^2} \right\rangle \hat{V}' + p' \left\langle \frac{B^2}{|\nabla\psi|^2} \lambda \right\rangle \hat{V}' - 2 \left\langle \frac{B^2}{|\nabla\psi|^2} \tau_n \right\rangle \hat{V}'. \quad (2.28)$$

Here, λ is the Pfirsch-Schlüter coefficient, which relates perpendicular currents to parallel currents, and $\sigma = \mu_0 \langle \mathbf{J} \cdot \mathbf{B} \rangle / \langle B^2 \rangle$. The flux surface average of a quantity f is defined as

$$\langle f \rangle = \frac{\oint d\Theta \oint d\zeta \sqrt{g} f}{V'}, \quad (2.29)$$

where $V' = \oint d\Theta \oint d\zeta \sqrt{g} = 4\pi^2 \hat{V}'$ is a normalization factor. Therefore, choosing two of the three flux functions immediately determines the third. This formulation allows studying a surface with reduced current free energy for reduced MHD stabilities by defining $\sigma = 0$, and control over ι' allows for adjusting stability properties of the flux surface.

It can be shown the methods of Section 2.2.1 and Section 2.2.2 are equivalent in the axisymmetric limit, however many of the details are not relevant to this thesis (for a thorough treatment and derivation, see [19]). However, one important detail when proving steps (1) and (2) in Section 2.2.1 are equivalent to step (1) in this section in the axisymmetric limit is relating the geometric poloidal angle (θ) to the straight field line poloidal angle (Θ):

$$\frac{\partial\Theta}{\partial\theta} = \frac{F}{qR^2 B_p} \sqrt{\left(\frac{\partial R}{\partial\theta}\right)^2 + \left(\frac{\partial Z}{\partial\theta}\right)^2}. \quad (2.30)$$

Using Equation (2.30), one can define shaping in geometric space, then compute the equilibrium using magnetic coordinates, which is often required for inputs to additional codes, such as GENE, discussed in Section 3.

To summarize, specifying a coordinate mapping $\mathbf{x}(\Theta, \zeta)$, ι , and two flux functions fully prescribes a 3D local MHD equilibrium. The general local equilibrium characterization by [19] is also equivalent to the description of [17] when describing an axisymmetric case.

2.2.3 Numerical Implementation

The description of a local equilibrium in the previous subsections was implemented numerically by the Numerical Evaluation of 3D Local Equilibria (NE3DLE) code [21]. NE3DLE is a Python program which solves a local equilibrium using the method in [19] to be input into gyrokinetic codes, such as GENE. The inputs for NE3DLE are a coordinate parameterization to relate the geometric and magnetic poloidal angles, a coordinate mapping to specify the flux surface shape, ι or q , two profile quantities of p' , ι' , or σ , and other computation settings. Also, instead of using the definitions of s and α in Equations (2.15) to (2.16), NE3DLE uses an alternative definition of global shear and pressure gradient using the dimensionless quantities \hat{s} and α [22]:

$$\hat{s} = \frac{r_0}{q_0} \frac{dq}{dr} \quad (2.31)$$

$$\alpha = -\frac{2\mu_0 R_0 q_0^2}{B_0^2} \frac{dp}{dr}, \quad (2.32)$$

where $q = q(\psi)$ and $p = p(\psi)$ are flux functions, R_0 is the major radius, $r_0 = r(\psi_0)$ is the minor radius of the flux surface at $\psi = \psi_0$, $q_0 = q(\psi_0)$, and B_0 is the toroidal field. Both [17] and Equations (2.31) and (2.32) prescribe an appropriate q' and p' , but with Equations (2.31) and (2.32) there is no need to compute flux surface volumes. First, geometric quantities are solved on a rectangular mesh grid in $\Theta - \zeta$ space. Then, important quantities related to the output file are calculated along a magnetic field line. **NE3DLE** outputs several settings and a nine-column array identical to a **GIST** output file [23], with the exception that the ninth column of **NE3DLE** is the field line angle. **GIST** is another equilibrium solving code already successfully coupled with **GENE**. A coordinate parameterization and coordinate mapping file to use the Miller equilibrium in **NE3DLE** using Equation (2.30) has been written, so shaped tokamak flux surfaces may be studied, as done in this thesis. Results of **NE3DLE** agree with analytic high-aspect-ratio expansion calculations. While **NE3DLE** has a shaped tokamak coordinate mapping and coordinate parameterization, there is no comprehensive coordinate mapping or coordinate parameterization for a 3D shaped stellarator, which would be beneficial to study stellarator shaping effects on turbulence.

2.3 Section Summary

Understanding the concepts of a flux surface and local equilibrium is critical to studying microstabilities, such as ITG turbulence. Magnetic coordinates, briefly derived in this section, lay out a mathematical foundation to communicate these concepts. Additionally, this section presented the Miller equilibrium [17], which builds on prior work, including global equilibrium theory also described in this section, to formulate a model to systematically vary flux surface shaping through profile quantities and nine shaping parameters. A generalized method of Miller et al. produced by Hegna [19] was also presented. The **NE3DLE** code uses the description of local equilibria presented by Hegna to output useful information for gyrokinetic codes used to study ITG turbulence, which will be discussed in Section 3.

3 Plasma Turbulence Simulations

The purpose of this section is to introduce key concepts and quantities used in gyrokinetic simulations of plasma turbulence and to motivate the research presented in this thesis. A brief conceptual overview of gyrokinetic and gyrofluid theory is given, followed by a discussion on flux tubes. Next, the GENE code is described. Then, different simulation assumptions are introduced. This section ends with a discussion of previous tokamak shaping ITG turbulence studies using gyrokinetic and gyrofluid simulations.

3.1 Gyrokinetic Theory

The theory of *gyrokinetics* is used to describe the fluctuations of various plasma quantities, including the magnetic field. Turbulent fluctuations, such as ITG mode drift waves, typically are on length scales of the ion gyroradius or smaller, and turbulent fluctuation frequencies are much smaller than the ion cyclotron frequency. Therefore, it is beneficial to convert a system where a charged particle has a helical trajectory along a magnetic field line to a system where a ring of charge with a radius equal to the particle’s gyroradius experiences the same guiding center drifts. The fully kinetic system is converted to the gyrokinetic system by averaging over a period of gyromotion. Many of the foundational derivations of gyrokinetic theory, including gyroaveraging can be found in [24]. Gyrokinetic simulations solve a system of equations comprising the perturbed gyrocenter form of the Vlasov Equation and gyrokinetic field equations; these equations are beyond the scope of this thesis and are not presented here, but can be found in [25]. Gyroaveraging reduces the dimensions of calculations by one, which greatly reduces the computational expense for gyrokinetic simulations.

An alternative application of gyrokinetics takes velocity moments of the perturbed gyrocenter form of the Vlasov Equation and adds closures, then solving fluid equations of the moments. This approach is called *gyrofluid* theory [26,27]. When moments of the gyrokinetic equation are taken, the moments of the distribution function become physical quantities. For example, the density n_s is the zeroth moment

$$n_s = \int f_s \mathbf{v}^0 d\mathbf{v}. \tag{3.1}$$

Closures are added to capture the physics missed by fluid equations. A complete description of gyrofluid equations and many of the appropriate closures can be found in [26]. While gyrofluid simulations are more efficient than gyrokinetic simulations, more geometrically complex simulations show significant discrepancies between gyrofluid and gyrokinetic calculations. In the 2D shearless slab and 3D sheared slab geometries, gyrofluid and gyrokinetic showed some promising agreements [28]. However, toroidal geometries showed significant discrepancies in thermal ion diffusivities—a way to measure heat loss (see Section 3.4 for more details)—between gyrokinetic and gyrofluid simulations [29]. More recently, after implementing a closure from [30] for *zonal flows* (a type of $\mathbf{E} \times \mathbf{B}$ driven poloidal flow of the plasma known to suppress turbulence [26,31,32]), a recent study by [33] found closer agreement to the gyrokinetic simulations in [29]. While the findings from [33] are promising for the

gyrofluid model, many tokamak shaping ITG turbulence studies (discussed in Section 3.5) were done prior to the development of the zonal flow closure from [30].

3.2 Flux Tubes

Gyrokinetic codes use *flux tubes*, a tube whose surfaces are flux surfaces, for turbulence simulations. Flux tubes are used for gyrokinetic simulations, because flux tubes use fewer computational resources than a global simulation [34]. Turbulent fluctuations have long wavelengths parallel to the magnetic field and short wavelengths perpendicular to the magnetic field, i.e. $\lambda_{\perp} \ll \lambda_{\parallel}$. Therefore, parallel correlation lengths are long and perpendicular correlation lengths are short for turbulent fluctuations. Using the nature of the parallel and perpendicular correlation lengths, a simulation domain may have a significantly smaller volume than using the whole torus while still resolving the necessary small-scale behaviors of microturbulence. Because of the reduced simulation domain, gyrokinetic computations for local, small-scale turbulence, such as ITG modes, use a flux tube geometry.

Flux tube geometry makes use of magnetic geometry, because the perpendicular and parallel behaviors relative to the magnetic field lines are easier to separate and minimize domain volume. Also, periodic boundary conditions can be enforced. Beginning with the Clebsch form for the magnetic field (Equation (2.6)) and choosing ψ to be the poloidal flux and the field line label as $\alpha = q\Theta - \zeta$ to be consistent with GENE, a coordinate system of (ψ, α, z) can be constructed, where $\eta = \Theta$ is the poloidal straight field line angle, representing the length of the flux tube. With this coordinate system, the simulation domain is centered about ψ_0 and α_0 , explicitly given as

$$\begin{aligned} \psi_0 - \Delta\psi < \psi < \psi_0 + \Delta\psi, \\ \alpha_0 - \Delta\alpha < \alpha < \alpha_0 + \Delta\alpha, \\ -z_0 < z < z_0, \end{aligned} \tag{3.2}$$

where the domain is several turbulent correlation lengths in each direction.

The boundary conditions for the simulation domain are periodic for each coordinate. However, for ψ and α , the periodicity is a statistical, rather than physical, assumption. This means, if the width $2\Delta\psi$ and $2\Delta\alpha$ are larger than the perpendicular turbulent correlation lengths, for a fluctuation quantity, f , $f(\psi + 2\Delta\psi, \alpha, z, t) = f(\psi, \alpha, z, t) = f(\psi, \alpha + 2\Delta\alpha, z, t)$. The periodicity of z is not as straight forward. The condition $f(\psi, \alpha, -z_0, t) = f(\psi, \alpha, z_0, t)$ implies all flux surfaces are rational ($q = m/n$, where m, n are integers), because the ends of the field lines connect after m toroidal and n poloidal turns. It is well known not all flux surfaces are rational, hence a different periodicity condition is needed for z . The periodicity condition for z relates the number of poloidal turns needed to resolve parallel correlation lengths, N , such that

$$\hat{f}_{m+\delta m, n}(\Theta + 2\pi N, t)C_n = \hat{f}_{m, n}(\Theta, t), \tag{3.3}$$

with

$$\begin{aligned}
C_n &= \exp(-i2\pi N n q_0 n_0), \\
n_0 &= \pi/\Delta\alpha, \\
\delta m &= 2\pi N n q' \frac{\Delta\psi}{\Delta\alpha},
\end{aligned} \tag{3.4}$$

where q' is the global magnetic shear, $q_0 = q(\psi_0)$, and $\hat{f}_{m,n}$ is the m, n th Fourier coefficient of f , and N must be chosen large enough such that $2z_0 = 2\pi N$ is several correlation lengths in length. This means a mode number m and $m + \delta m$ are coupled together at opposite ends of the flux tube. The details and derivation of the parallel periodicity are not directly relevant to the thesis, and can be found in [34]. However, it is important to understand the parallel periodicity of a flux tube domain is not as straight forward as one might think.

GENE uses a coordinate system similar to the (ψ, α, z) system. The mapping from (ψ, α, z) to GENE's (x, y, z) system is as follows:

$$\begin{aligned}
x &= \frac{q_0}{B_0 r_0} (\psi - \psi_0) \\
y &= \frac{r_0}{q_0} (\alpha - \alpha_0) \\
z &= \Theta.
\end{aligned} \tag{3.5}$$

Here, B_0 is the toroidal field and r_0 is the geometric distance from the magnetic axis to the center of the simulation domain. The perpendicular wave numbers are

$$k_x = \frac{m\pi}{\Delta x} = \frac{m\pi B_0 r_0}{q_0 \Delta\psi}, \tag{3.6}$$

$$k_y = \frac{n\pi}{\Delta y} = \frac{n\pi q_0}{r_0 \Delta\alpha}, \tag{3.7}$$

$$k_\perp^2 = k_x^2 g^{xx} + 2k_x k_y g^{xy} + k_y^2 g^{yy}, \tag{3.8}$$

where g^{ij} is i, j element of the metric tensor for the (x, y, z) coordinate system:

$$g^{ij} = \nabla x_i \cdot \nabla x_j, \tag{3.9}$$

with $x_i, x_j \in \{x, y, z\}$.

In simulations the finite domain size of a flux tube discretizes the wavenumbers in the perpendicular directions. Using GENE notation, a minimum wavenumber, designated by superscript “min”, describes both wavenumber

$$k_x = m k_x^{\min}, \quad k_y = n k_y^{\min}, \quad m, n \in \mathbb{Z} \text{ such that } m \leq n x_0, n \leq n k y_0, \tag{3.10}$$

where $n x_0$ and $n k y_0$ sets the number of wavenumber used, and box size

$$L_x = 2\pi/k_x^{\min}, \quad L_y = 2\pi/k_y^{\min}. \tag{3.11}$$

It is apparent from Equation (3.4) that the parallel boundary condition imposes a direct relationship between L_x and L_y . Hence, for example, halving one minimum wavenumber halves the other and doubles both L_x and L_y . Understanding how flux tube geometry and wavenumber resolution are related, along with Equation (3.8), is important for discussing gyrokinetic results in Sections 4 and 5.

3.3 The Gene Code

One widely used gyrokinetics code is the Gyrokinetic Electromagnetic Numerical Experiment (GENE) code [35,36]. GENE is a massively-parallel gyrokinetic turbulence code used to study microturbulence in astrophysical and magnetized fusion plasmas in both tokamak and stellarator geometries. While GENE is capable of global calculations, this thesis will focus on local simulations in GENE, which uses a computational domain with a flux tube geometry. Computations in GENE use non-dimensional values, which also must be defined. Outlining important quantities from the flux tube geometry and normalizations is important to understand the data gathered in Sections 4 and 5.

3.3.1 Gene Normalizations

Important physical quantities are normalized to be non-dimensional in GENE, and these quantities should be understood to interpret gyrokinetic results. The non-dimensional quantities are of order unity to reduce numerical machine error. In addition, GENE uses reference quantities with subscript “ref” are chosen based on the species of interest. For instance, this thesis focuses on ITG turbulence, therefore the reference quantities are chosen to be of the ions in the plasma. A device length scale L_{ref} is also used (for the calculations in this thesis, the major radius R_0 was used), and a reference magnetic field B_{ref} is typically the toroidal magnetic field. Additional reference quantities used are density n_{ref} , temperature T_{ref} , mass m_{ref} , and the elementary charge e . Additionally, the reference gyroradius ρ_{ref} is derived, along with a reference thermal velocity c_{ref} :

$$c_{\text{ref}} = \sqrt{\frac{T_{\text{ref}}}{m_{\text{ref}}}} \quad (3.12)$$

$$\rho_{\text{ref}} = \frac{m_{\text{ref}} c_{\text{ref}}}{e B_{\text{ref}}}. \quad (3.13)$$

These non-dimensional values are important to know when discussing the results in Sections 4 and 5.

3.4 Types of Microturbulence Calculations

Gyrokinetic and gyrofluid simulations have a multitude of different assumptions resulting in a trade-off between computation speed and simulation accuracy. The purpose of this section is to present several settings for microturbulence simulations pertinent to this thesis and previous studies discussed in Section 3.5. Specifically, this subsection discusses the difference between using a linear or nonlinear simulation and adiabatic versus kinetic electrons.

Often, the linear behavior of waves in plasmas are studied, and making a linear assumption can reduce computational expense of microturbulence simulations. Suppose there is a plasma at an equilibrium, then the equilibrium is perturbed. A quantity is represented as $f = f_0 + f_1$, where f_0 is the equilibrium value, and $f_1 = \tilde{f} e^{i\mathbf{k}\cdot\mathbf{x} - i\omega t}$ is the perturbed value. Because the perturbed quantity is assumed small relative to the equilibrium value (i.e. $|f_1|/|f_0| \ll 1$), the system can be linearized, meaning quantities of order $\mathcal{O}(f_1^2)$ are neglected. The frequency, ω , is a complex number in general, and the growth rate is $\gamma = \Im(\omega)$.

If the growth rate is negative(positive), then the perturbed quantity experiences exponential decay(growth). Additionally, a mixing length estimate of $\chi \sim \gamma/k_{\perp}^2$ may be used to determine the scaling of heat lost Q , where χ is a thermal diffusivity based on the linear heat equation $Q = n\chi\nabla T$. Linear computations miss out on nonlinear effects, such as saturation, but are suitable to study stability properties by using growth rates, while also reducing the computational demands by not using nonlinear terms in the calculations.

Nonlinear simulations, however, are more realistic, albeit more resource intensive than linear simulations. While linear approximations are a good measure of stability by calculating growth rates, nonlinear simulations capture nonlinear behavior, such as turbulent saturation, discussed previously in Section 1.4. As a result, nonlinear computations directly calculate heat lost or thermal diffusivity instead of an indirect calculation using growth rates. Although including nonlinear terms in the simulations requires many more computational resources, but it is not prohibitive.

Another consideration in microturbulence simulations is treating the plasma as having *adiabatic electrons* or having *kinetic electrons*. Adiabatic electrons means the electrons are treated as having zero mass and moving infinitely fast along magnetic field lines, therefore responding infinitely quickly to changes in temperature and maintaining a Maxwellian velocity distribution. Kinetic electrons means electrons are treated as a second species in the plasma with finite mass and thermal equilibration times (i.e. electrons may have a non-Maxwellian velocity distribution). As a result, kinetic electrons introduce physics, such as trapped electrons, which also influences ITG modes. Using kinetic electrons in a turbulence simulation uses more computing power but also captures more physics. For drift waves, kinetic electrons lead to a larger charge separation than an adiabatic electron treatment and therefore may increase growth rates. Both concepts of linear and nonlinear simulations and adiabatic versus kinetic electrons will show up in the next section, along with Sections 4 and 5.

3.5 Tokamak Shaping ITG Turbulence Studies

The tokamak community widely accepts that flux surface shaping in tokamaks has a significant effect on gyrokinetic stability, however the exact effects are unknown. ITG turbulence in particular is influenced by the changes in local shear caused by shaping [37, 38]. Theoretical and computational studies have been done on the effects of tokamak shaping on gyrokinetic linear stability [39, 40]. The linear studies done by [40] used the Miller equilibrium [17] and the gyrokinetic code GS2 [36, 41], varying aspect ratio A , elongation κ , and triangularity δ away from a base case (later called the ‘‘GA standard (STD) case’’):

$$\begin{array}{lll}
 r/a = 1/2 & \beta = 0(\alpha = 0) & a/L_T = 3 \\
 R_0/a = 3(A = 6) & \kappa = 1 & a/L_n = 1 \\
 q = 2 & \delta = 0 & T_i/T_e = 1 \\
 \hat{s} = 1 & & \nu_{ei} = 0.
 \end{array}$$

The ratio between mean plasma pressure and magnetic field strength is $\beta = \langle p \rangle / (B^2/2\mu_0)$, and the third column, from top to bottom, is the background ion temperature gradient,

background ion density gradient, background ion-electron temperature ratio, and electron-ion collision frequency. The linear study in [40] concluded ITG modes became less unstable as κ and δ were increased, more so with negative triangularity than positive triangularity, and lower aspect ratios saw lower growth rates, if adiabatic electrons were assumed. However, the shaping parameter scans presented only looked at a single wavenumber, $k_y \rho_s = 0.4$. Because lower wavenumbers correspond to longer wavelengths, most turbulence effects occur at low wavenumbers. If the growth rate trends at wavenumbers lower than $k_y \rho_s = 0.4$ are different than the trends shown in [40], the conclusions drawn by [40] on how κ , δ , and A affect ITG turbulence in a tokamak could be different. Therefore, looking at growth rates over a large k_y spectrum would provide greater insight into how shaping affects linear ITG stability.

Further studies looked at the effects shaping has on the nonlinear behaviors of ITG turbulence, some using a gyrofluid approach [40, 42] and others using a gyrokinetic approach [43, 44]. The nonlinear gyrofluid study done by [40] used a code with four-moment (density, parallel velocity, and perpendicular and parallel pressure) closure for adiabatic electrons [45]. The metric for ITG turbulence used in this study used an ion thermal diffusivity, χ_{ITER} and assumed a linear heat loss. First, κ was varied, which resulted in χ_{ITER} decreasing. Then, the effects of safety factor on changing κ at different q was studied. As q increased, the dependence of χ_{ITER} on κ weakened. The paper [40] concludes increasing κ decreases χ_{ITER} , however this relationship depends on the safety factor. The major drawback of [40] is in the gyrofluid code used for nonlinear calculations included few moments and missed zonal closures, as the study was during the early development of gyrofluid theory.

Although most ITG turbulence has been studied in core-like plasmas, a study done in [42] looked at edge-like plasmas using the gyrofluid code GEM [46, 47]. The study varied elongation $1 \leq \kappa \leq 2$ and triangularity $0 \leq \delta \leq 0.4$. Using both turbulent particle transport F_n and heat transport Q_i as metrics, [42] found increasing κ or δ reduced F_n and Q_i , but δ had a weaker effect than κ . Additionally, [42] concluded the physical causes of ITG turbulence suppression in increased elongation came from (1) magnetic shear damping, (2) reduced curvature drive, and (3) zonal flow enhancement. Again, [42] uses a gyrofluid code, which misses some wave-particle resonance physics.

While most tokamak shaping studies used nonlinear gyrofluid codes, [43] used the nonlinear gyrokinetic code GYRO [48]. GYRO has been benchmarked with analytic theory and linear gyrokinetic codes [48] and with GENE [49]. The study in [43] investigated the effect of elongation κ on linear stability, nonlinear ion diffusivities with adiabatic and kinetic electrons using the STD case. Again, increasing κ was found to decrease ITG growth rates and decrease ion diffusivities. In addition, this study looked at the effects of triangularity on ion diffusivities by scanning from $\delta = -0.5$ to 0.75 in the STD case but with $\kappa = 1.5$. The study found ion diffusivities increased across the triangularity scan. As with [40], the study by [43] assumes a linear heat loss, and it is unknown whether some nonlinear heat loss physics may play a significant role.

As mentioned in Section 2.2.1, plasma profile parameters, radial shift $\partial r R_0$, and the other shaping parameters may be coupled together in a real machine. A study done by [44] explored how changing κ for realistic equilibria effects stability and nonlinear diffusivity using the gyrokinetic GS2 code [36, 41] with kinetic electrons. The study reconstructed equilibria from data gathered by the Joint European Torus (JET). A scaling of shaping and plasma

parameters, including δ , as a function of κ is given, then κ is scanned from 1 to 2.20. The results of [44] found increasing κ decreased linear ITG growth rates and decreased χ_{ITER} . While this study elucidates how changing κ for a realistic plasma affects ITG turbulence, the study does not differentiate the effects of elongation from triangularity. In addition, like the previous studies discussed in this section, this study assumes a linear heat loss as well.

Several aspects of how flux surface shaping effects ITG turbulence is still unclear. Therefore, the research presented in this thesis covers several properties of ITG turbulence and equilibrium geometry. First, elongation and triangularity were varied independently to separate the effects of each parameter from the other. Curvature and stability metrics along the magnetic field lines of the equilibria are discussed in the context of ITG turbulence. Then, nonlinear heat fluxes were computed using GENE to capture physics missed by the linear heat loss assumption and nonlinear gyrofluid studies and compared to a quasilinear heat flux estimation. The aforementioned studies present an updated and novel insight on the effect flux surface shaping has on ITG turbulence.

3.6 Section Summary

This section described several methods by which plasma turbulence is studied. Gyrokinetic and gyrofluid theory were introduced, followed by how local turbulence simulation domains are described with flux tube geometry. Then, the GENE code and its normalizations were described. Next, this section discussed several assumptions made in gyrokinetic and gyrofluid simulations, including linear and nonlinear simulations, quasilinear heat loss, and adiabatic and kinetic electrons. Finally, previous tokamak shaping studies were discussed, illuminating the need for a new gyrokinetic study of how flux surface shaping affects ITG turbulence with GENE.

4 Linear Studies

The effects of shaping on the linear stability of ITG turbulence are presented in this section. In this section and Section 5 flux surfaces are scanned in elongation κ and triangularity δ away from a base case similar to the STD case, using NE3DLE to compute the input files for GENE:

$$\begin{array}{lll}
 r/a = 1/2 & \beta = 0(\alpha = 0) & R_0/L_T = 9 \\
 R_0/a = 3(A = 6) & \kappa = 1 & R_0/L_n = 3 \\
 q = 2 & \delta = 0 & T_i/T_e = 1 \\
 \hat{s} = 1 & \partial_r R_0 = 0 & \nu_{ei} = 0.
 \end{array}$$

The parameters above will be referred to as the base case. The base case configuration was chosen to be similar to the STD case, except this thesis's base case is normalized to the major radius, \hat{s} is consistent with Equation (2.31), and $\partial_r R_0$ was not prescribed in STD. For this thesis, the current profile and pressure profile were not assumed, the aspect ratio was not large, and not every shaping was purely elliptical, making the derivation for $\partial_r R_0$ in [20] not proper for the geometries considered in this thesis. In addition, holding the radial shift constant separates the effects of $\partial_r R_0$ from shaping effects. Separating $\partial_r R_0$ from κ and δ is reasonable, because the radial shift may be manipulated in machines by using vertical magnetic fields.

Linear simulations were performed for geometries with $1 \leq \kappa \leq 2.5$ and $-0.75 \leq \delta \leq 0.75$. Results are presented for both elongation and triangularity scans assuming adiabatic electrons. ITG growth rates over the $k_y \rho_s$ spectrum were obtained, indicating geometries with more elongation and triangularity—both negative and positive—have lower ITG growth rates at low $k_y \rho_s$. In addition, the growth rate spectra for triangularity shows high positive triangularity geometries had lower ITG growth rates at low $k_y \rho_s$ than high negative triangularity geometries. Quasilinear heat flux calculations indicate with more elongation or triangularity, the quasilinear heat flux decreases, again with high positive triangularity configurations having lower quasilinear heat flux than high negative triangularity configurations. All heat fluxes presented in this thesis are physically interpreted as radial heat flux and are given in gyro-Bohm units, i.e. normalized to $Q_{gB} = c_s n_i T_i (\rho_s / R_0)^2$.

4.1 Linear Stability Analysis

In this section, the linear simulations used an initial value method to find the fastest growing mode for each $k_y \rho_s$ assuming adiabatic electrons. All modes presented in this section are known to be ion modes, because the real part of the frequency is positive, corresponding to the ion gyration direction in GENE. Each growth rate was computed to the nearest thousandth in the linear simulations. Numerical convergence for growth rates were checked by doubling the number of k_x modes used ($nx0$) and in the parallel spatial resolution ($nz0$), where nearly all growth rates changed by less five percent, and a majority of growth rates changed by less than two percent. The largest change in growth rate when the radial resolution was doubled was 0.002. When parallel spatial resolution was doubled, some growth rates where $\gamma \sim \mathcal{O}(10^{-1})$ changed by less than ten percent. A few

growth rates with $\gamma \sim \mathcal{O}(10^{-3})$ changed by more than 50 percent, but still remained near zero. Growth rates were computed in the $k_y \rho_s$ spectrum for $0.05 \leq k_y \rho_s \leq 1$ for triangularity scans and $0.05 \leq k_y \rho_s \leq 2$ for elongation scans. The simulation resolutions were $n_x 0 \times n_{k_y} 0 \times n_z 0 \times n_v 0 \times n_w 0 = 16 \times 1 \times 32 \times 32 \times 8$ for $\delta \leq 0.5$ and $n_z 0 = 64$ for $\delta = 0.75$. Here, the number of k_y modes used is $n_{k_y} 0$, the parallel velocity resolution is $n_v 0$, and the perpendicular velocity resolution is given by $n_w 0$. Necessary for collisionless simulations, the parallel hyper diffusion term, discussed in [50], was set to $\epsilon_z = 2$.

4.1.1 Linear Growth Rates

To investigate linear stability of a configuration, the linear ITG growth rates must be computed. The growth rates of ITG modes in elongation scans away from this base case assuming adiabatic electrons are presented in Figure 4.1. Flux surfaces with elongation greater than this base case ($\kappa = 1$) had unstable modes at larger $k_y \rho_s$ than the base case. The maximum growth rate increases with elongation and shifts to higher $k_y \rho_s$. The difference in growth rates can usually be explained by differences in curvature at local minimums in a stability metric g^{yy} in Figure 4.2. In Figure 4.2a, the stability metric has a minimum at $\eta = 0$, meaning shear, a stabilizing mechanism, is smallest at $\eta = 0$. Here, η is a field line angle where $\eta \in [-q\pi, q\pi)$. Therefore, modes may be more likely to be localized around $\eta = 0$. To confirm mode locations, an analysis of the eigenmode structure along the field line must be preformed, however this thesis uses g^{yy} minima as a preliminary metric for mode

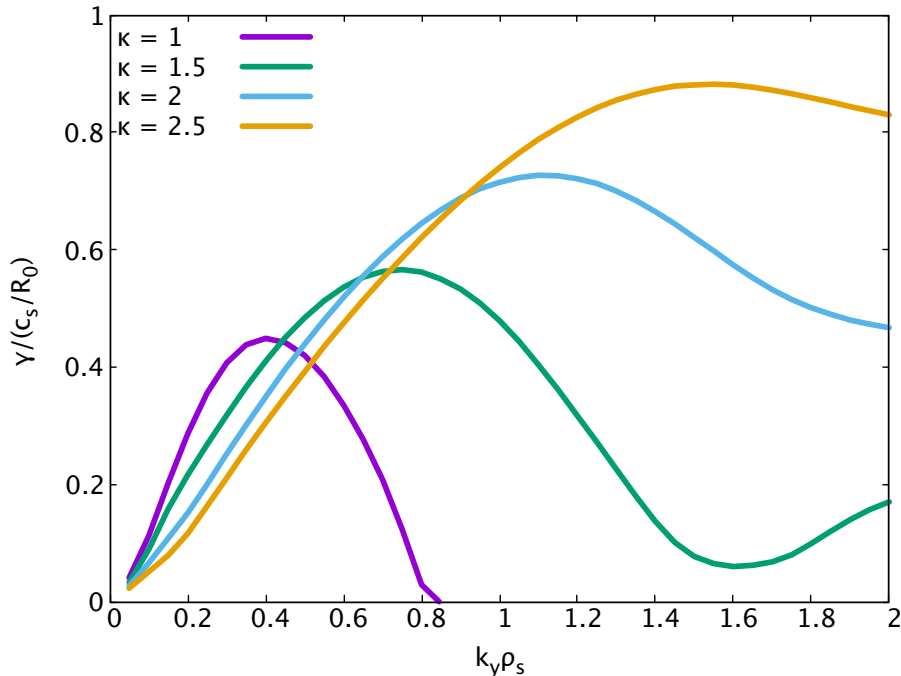


Figure 4.1: ITG growth rates of elongated geometries for the base case ($\kappa = 1$) (purple), $\kappa = 1.5$ (green), $\kappa = 2$ (light blue), and $\kappa = 2.5$ (orange) scanned over $k_y \rho_s$ assuming adiabatic electrons.

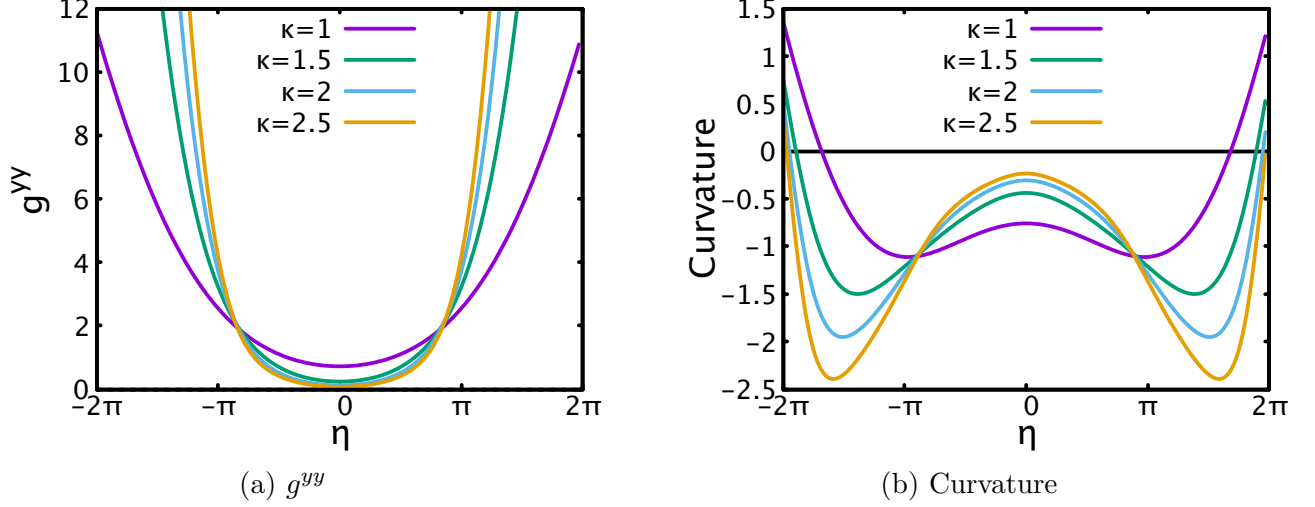


Figure 4.2: A stability metric (a) and curvature of the magnetic field (b) along a field line for the base case ($\kappa = 1$) (purple), $\kappa = 1.5$ (green), $\kappa = 2$ (light blue), and $\kappa = 2.5$ (orange).

localization. In this section, Curvature is defined as

$$\text{Curvature} = rR_0 \frac{B}{B_0} (\kappa_n + \Lambda \kappa_g) - \frac{\mu_0 r R_0}{B} \frac{dp}{d\psi}, \quad (4.1)$$

and is stabilizing, or *favorable*, when positive and destabilizing, or *unfavorable*, when negative. The stability metric g^{yy} is defined as

$$g^{yy} = \frac{r^2 B^2}{|\nabla\psi|^2} (1 + \Lambda^2), \quad (4.2)$$

where the integrated local shear is $\Lambda = -(\nabla\psi \cdot \nabla(\Theta - t\zeta))/B$. The region around $\eta = 0$ for increasing elongation has less unfavorable curvature. Because more unfavorable curvature drives ITG instabilities, smaller growth rates would be expected with increasing elongation. The trend in curvature at $\eta = 0$ matches with the growth rate trends for $k_y \rho_s \leq 0.4$ in Figure 4.1 but not the increase in growth rates at high $k_y \rho_s$.

Another metric of ITG turbulence is the quasilinear heat flux. The growth rates at lower $k_y \rho_s$ have a greater influence on heat flux, because lower wavenumbers correspond to larger wavelength turbulence. Mathematically, lower wavenumbers have a larger contribution than higher wavenumbers, because, assuming $k_x = 0$, $Q_L \propto \gamma/k_y^2$. Hence, the growth rates at $k_y \rho_s \leq 0.4$ will likely contribute to the majority of ITG turbulent heat flux. In addition, if the trends in growth rates for $k_y \rho_s > 2$ are assumed to continue, growth rates for $k_y \rho_s > 2$ for the three elongated geometries would be significant. However, the growth rates do not increase fast enough with $k_y \rho_s$ to significantly contribute to Q_L . At $k_y \rho_s \leq 0.4$ increasing elongation corresponds to decreased growth rates. Therefore, despite geometries with higher elongation having larger maximum growth rates, the lower growth rates at low $k_y \rho_s$ may result in lower ITG turbulent heat flux.

In Figure 4.3, the ITG growth rates for positive triangularity scans are presented. The maximum growth rate and growth rates for $k_y \rho_s \leq 0.65$ were approximately equal for

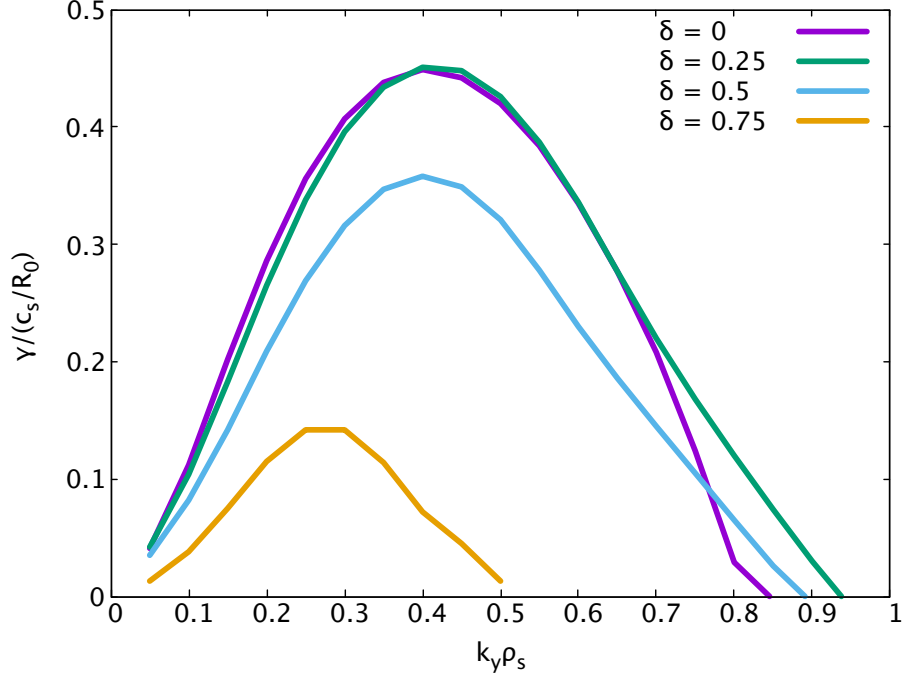


Figure 4.3: ITG growth rates of positive triangularity geometries for the base case ($\delta = 0$) (purple), $\delta = 0.25$ (green), $\delta = 0.5$ (light blue), and $\delta = 0.75$ (orange) scanned over $k_y \rho_s$ assuming adiabatic electrons.

$\delta = 0.25$ and this base case. However, for the two larger triangularity cases, the maximum growth rate and growth rates for $k_y \rho_s \leq 0.75$ were less than the growth rates of the base case, with $\delta = 0.75$ having substantially lower growth rates and fewer unstable modes than any case for $\delta \geq 0$. The trends in growth rates may be explained by the change in mode location and curvature in Figure 4.4. In Figure 4.4a, the base case and $\delta = 0.25$ had only one minimum g^{yy} , located at $\eta = 0$, therefore ITG modes for $\delta = 0.25$ and the base case are expected to exist locally near $\eta = 0$. In Figure 4.4b the curvature near $\eta = 0$ for $\delta = 0.25$ and the base case were almost equivalent, with $\delta = 0.25$ with slightly more unfavorable curvature. Therefore, the change in curvature predicts slightly higher growth rates for $\delta = 0.25$ than for the base case.

For the $\delta = 0.5$ and $\delta = 0.75$ cases, the stability has local minima at $\eta = 0$, $\eta \approx \pm 3\pi/4$, and $\eta = -2\pi$ (it should be noted that because this is a rational surface with $q = 2$, $\eta = 2\pi$ and $\eta = -2\pi$ are the same point). Although the curvature was more unfavorable for both $\delta = 0.5$ and $\delta = 0.75$ with respect to the base case for the modes near $\eta = 0$, the curvature was less unfavorable for the modes near $\eta \approx \pm 3\pi/4$ and more favorable for the modes near -2π . It is clear that growth rates for $\delta = 0.5$ were lower than the base case and $\delta = 0.25$, because the unfavorable curvature near $\eta = 0$ increases marginally compared to the decrease in unfavorable curvature near $\eta \approx \pm 3\pi/4$ and the increase in favorable curvature near $\eta = -2\pi$. The same argument follows for $\delta = 0.75$, despite the large increase in unfavorable curvature near $\eta \approx \pm \pi/2$. The contribution to growth rates from the minima in curvature near $\eta \approx \pm \pi/2$ is likely offset by the increase in curvature near $\eta \approx \pm \pi$, because the minima in g^{yy} is about midway between $\eta \approx \pm \pi/2$ and $\eta \approx \pm \pi$. The change in curvature near

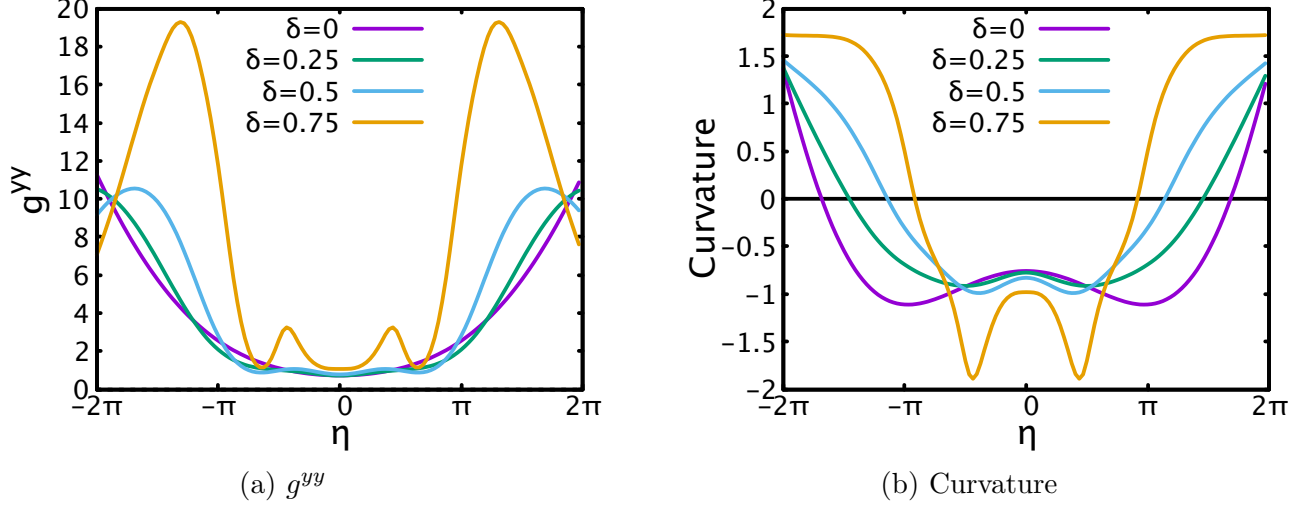


Figure 4.4: A stability metric (a) and curvature of the magnetic field (b) along a field line for the base case ($\delta = 0$) (purple), $\delta = 0.25$ (green), $\delta = 0.5$ (light blue), and $\delta = 0.75$ (orange).

minima of g^{yy} for $\delta = 0.5$ and $\delta = 0.75$ predict the reduction in growth rates compared to $\delta = 0.25$ and the base case observed in Figure 4.3.

An estimate of the relationship between turbulent heat flux and positive triangularity may be made using the growth rates in Figure 4.3. Because growth rates at $k_y \rho_s < 0.4$ for $\delta = 0.25$ were slightly less than the base case and similar until $k_y \rho_s = 0.7$, the quasilinear heat flux for $\delta = 0.25$ should be similar to or slightly less than the quasilinear heat flux for this base case. For the higher positive triangularity cases, as triangularity increases, all growth rates for $k_y \rho_s < 0.7$ decrease significantly. Therefore, the quasilinear heat flux should remain relatively flat for $\delta \leq 0.25$, then decrease significantly with increasing positive triangularity.

The ITG growth rates in negative triangularity geometries are presented in Figure 4.5. Flux surfaces with more negative triangularity had lower maximum growth rates at low $k_y \rho_s$, and the growth rates at any $k_y \rho_s$ were lower for configurations with more negative triangularity than configurations with less negative triangularity. The changes in curvature at local minima of g^{yy} were not as predictive for the change in growth rates between this base case and the negative triangularity cases. The stability metric and curvature for negative triangularity geometries are shown in Figure 4.6. For $\delta = -0.25$ and the base case, the stability metric has a minimum at $\eta = 0$, so ITG modes are expected to be localized only near $\eta = 0$ for these two cases. In Figure 4.6b, the unfavorable curvature near $\eta = 0$ increases slightly from the base case to $\delta = -0.25$. The increase in unfavorable curvature near $\eta = 0$ would suggest growth rates would increase marginally from $\delta = 0$ to $\delta = -0.25$.

For the cases $\delta = -0.5$ and $\delta = -0.75$, g^{yy} has minima at $\eta = 0$, $\eta \approx \pm 3\pi/4$, and $\eta \approx \pm 7\pi/4$. The curvature near $\eta \approx \pm 7\pi/4$ for $\delta = -0.5$ and $\delta = -0.75$ was approximately the same as the curvature near $\eta = 0$, therefore the modes near $\eta \approx \pm 7\pi/4$ would not significantly contribute to the growth rate trends in negative triangularity. The unfavorable curvature near $\eta = 0$ increases slightly δ increases, and the unfavorable curvature decreases slightly near $\eta \approx \pm 3\pi/4$. Based on the changes in curvature near g^{yy} minima, the growth

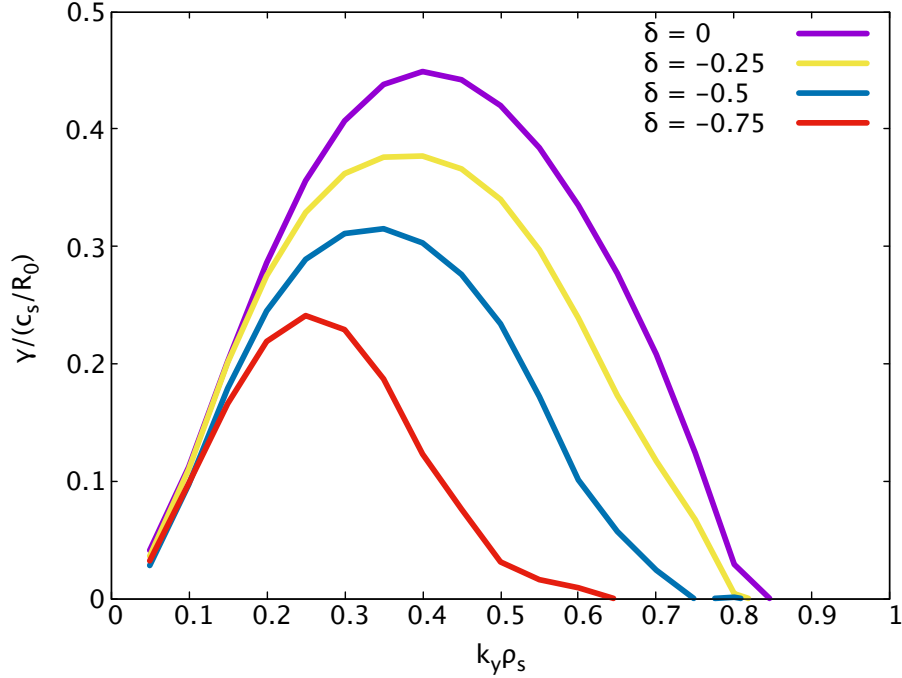


Figure 4.5: ITG growth rates of negative triangularity geometries for the base case ($\delta = 0$) (purple), $\delta = -0.25$ (yellow), $\delta = -0.5$ (dark blue), and $\delta = -0.75$ (red) scanned over $k_y \rho_s$ assuming adiabatic electrons.

rates for each negative triangularity case should remain relatively similar to the base case, however a significant change in growth rates are observed in Figure 4.5.

Based on the growth rates in Figure 4.5, an estimation for the heat flux may be made.

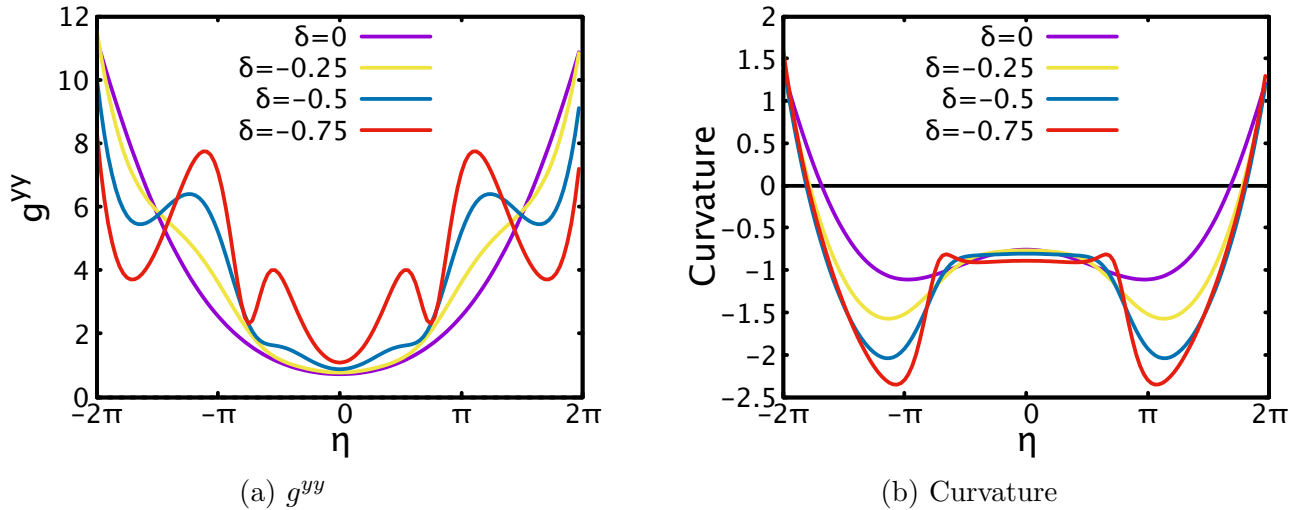


Figure 4.6: A stability metric (a) and curvature of the magnetic field (b) along a field line for the base case ($\delta = 0$) (purple), $\delta = -0.25$ (yellow), $\delta = -0.5$ (dark blue), and $\delta = -0.75$ (red).

Because the growth rates for $k_y \rho_s \leq 0.2$ were similar in all four cases, the contribution of these modes to the heat flux may be comparable. For $k_y \rho_s \geq 0.2$, the growth rates at each $k_y \rho_s$ decreases monotonically with increasing negative triangularity. Therefore, the quasilinear heat flux from ITG turbulence is likely to be less for a case with higher negative triangularity than a case with less negative triangularity.

It is also interesting to compare the positive and negative triangularity cases. As has been mentioned, both maximum growth rate and quasilinear heat flux predictions decrease with increasing negative or positive triangularity with respect to this base case. However, the $\delta = 0.25$ case has larger growth rates than the $\delta = -0.25$ case. Therefore, using a quasilinear assumption, the heat flux from the $\delta = 0.25$ case would be larger than the $\delta = -0.25$ case. The $\delta = 0.5$ case has a maximum growth rate larger than the $\delta = -0.5$ case, but the $\delta = 0.5$ case has lower growth rates for $k_y \rho_s \leq 0.3$ than the $\delta = -0.5$ case. The quasilinear heat flux from the $\delta = 0.5$ case is likely to be comparable to but less than the quasilinear heat flux from the $\delta = -0.5$ case. At $\delta = 0.75$, the growth rates were much smaller than the growth rates for $\delta = -0.75$, and the heat flux should follow suit.

4.2 Quasilinear Heat Flux

The quasilinear heat flux Q_L of elongation and triangularity scans is presented in this section. For each shaping scan, the quasilinear flux was computed using a simple Python script QLHeat.py. Mathematically, the quasilinear heat flux is described by

$$Q_L = n\chi \nabla T, \quad (4.3)$$

where χ is computed by the following:

$$\chi = \mathcal{C} \sum_{k_y} \frac{\gamma_{k_y}}{\langle k_{\perp}^2 \rangle}, \quad (4.4)$$

$$\langle k_{\perp}^2 \rangle = \frac{\int_{-\infty}^{\infty} dz \sqrt{g} |\Phi|^2 (k_x^2 g^{xx} + 2k_x k_y g^{xy} + k_y^2 g^{yy})}{\int_{-\infty}^{\infty} dz \sqrt{g} |\Phi|^2}, \quad (4.5)$$

where the constant \mathcal{C} is chosen to match nonlinear and quasilinear heat fluxes for a standard case, and Φ is the electrostatic potential from the eigenfunction. The integral for the average perpendicular wavenumber squared can be discretized by adding the contribution from each radial mode k_x for each summation along the finite field line domain, $[-q\pi, q\pi)$:

$$\int_{-\infty}^{\infty} dz \rightarrow \sum_{k_x} \sum_{n \neq 0}.$$

The constant \mathcal{C} was chosen to compare quasilinear and nonlinear heat fluxes in Section 5.2. To compare nonlinear and quasilinear heat fluxes, a case must be chosen to match the quasilinear to the nonlinear heat flux; for this thesis, the base case was chosen. Then, \mathcal{C} was computed as the ratio of nonlinear heat flux to linear heat flux without the constant.

The quasilinear heat flux for various elongations away from the base case are presented in Figure 4.7. As κ increases, the quasilinear heat flux decreases approximately linearly. The

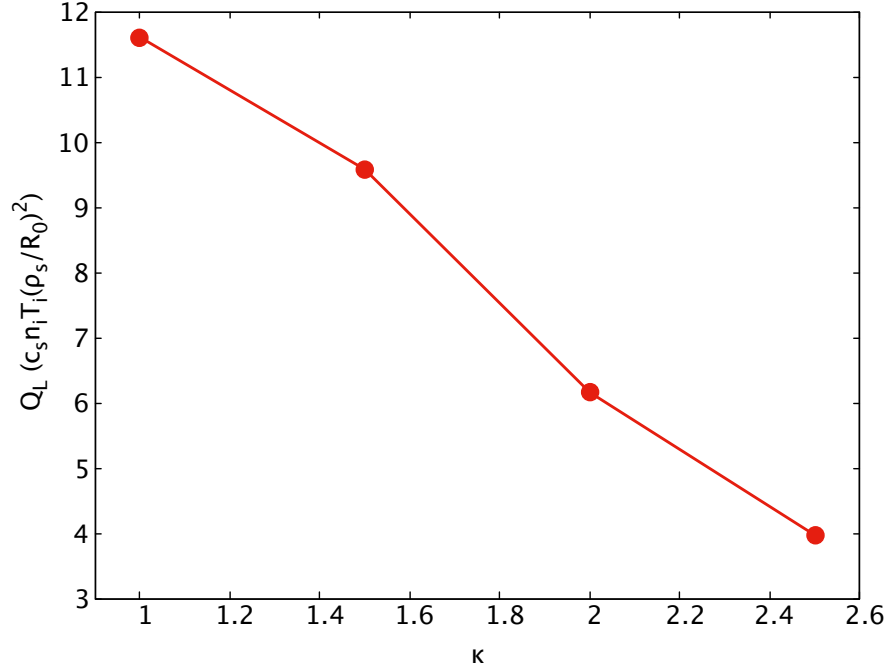


Figure 4.7: Quasilinear heat flux using growth rates for $k_y \rho_s \leq 2$ for the base case ($\kappa = 1$), $\kappa = 1.5$, $\kappa = 2$, and $\kappa = 2.5$.

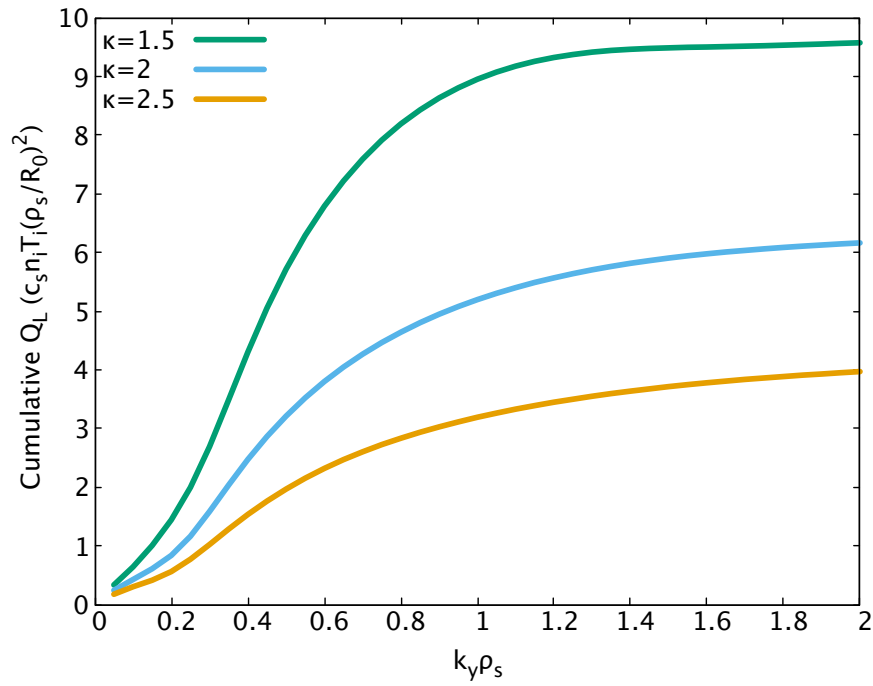


Figure 4.8: Cumulative quasilinear heat flux contribution as a function of $k_y \rho_s$ for $\kappa = 1.5$ (green), $\kappa = 2$ (light blue), and $\kappa = 2.5$ (orange).

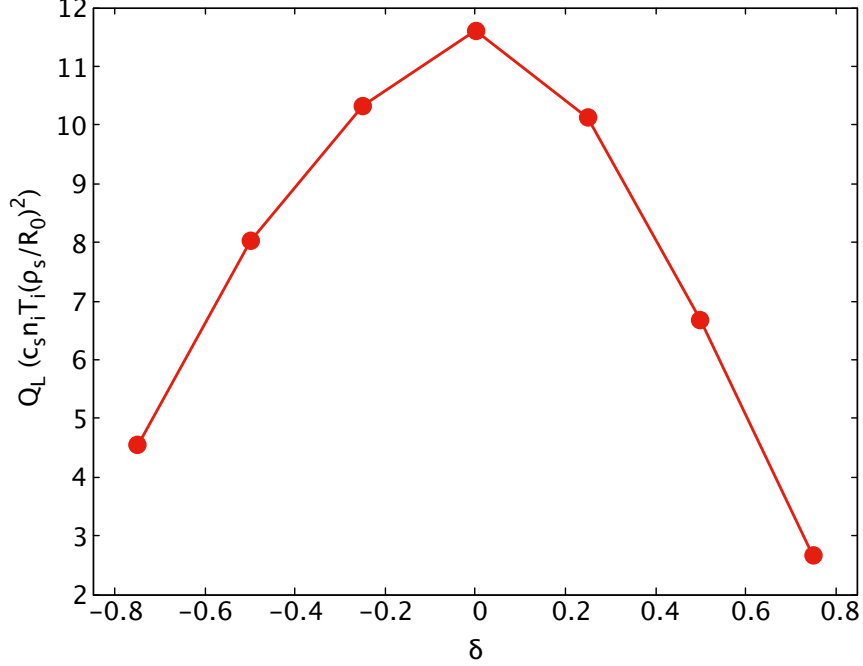


Figure 4.9: Quasilinear heat flux for the base case ($\delta = 0$), $\delta = \pm 0.25$, $\delta = \pm 0.5$, and $\delta = \pm 0.75$.

quasilinear heat flux for $\kappa = 2$ was approximately 3 times lower than the circular base case with $\kappa = 1$. The decrease in Q_L with elongation was in good agreement with the predictions made from Figure 4.1 in the previous section.

Also, as mentioned in the previous section, growth rates at $k_y \rho_s > 2$ are likely to be significant, but the contributions to Q_L from modes at $k_y \rho_s > 2$ would likely be on the same order as the contributions from the modes at $k_y \rho_s = 2$. In Figure 4.8, the cumulative heat flux is plotted with $k_y \rho_s$ for the three elongated cases. Almost all of the contribution to Q_L for each case comes from growth rates at $k_y \rho_s < 1.5$. Importantly, the contributions to Q_L from modes $1.5 \lesssim k_y \rho_s \leq 2$ were very small, meaning contributions to Q_L from growth rates at $k_y \rho_s > 2$ would be very small as well. Therefore, growth rates at $0.05 \leq k_y \rho_s \leq 2$ are sufficient to compute the quasilinear heat flux for $\kappa \in \{1.5, 2, 2.5\}$.

In Figure 4.9 the quasilinear heat fluxes for triangularity scans away from the base case are presented. Beginning at the base case of $\delta = 0$, as more triangularity—both positive and negative—is added, the quasilinear heat flux decreases significantly. Despite having very similar growth rate trends, the $\delta = 0.25$ case has a significantly lower Q_L than the base case, which was likely due to $\delta = 0.25$ having lower growth rates for $k_y \rho_s < 0.4$ (Figure 4.3), because $Q_L \propto \gamma / k_y^2$. Additionally, the quasilinear heat fluxes for positive triangularity configuration were lower than the negative triangularity counterparts. This trend can be explained by examining Figure 4.3 and Figure 4.5. For negative triangularity configurations in Figure 4.5, the growth rates for $k_y \rho_s \lesssim 0.15$ —the region likely contributing to the majority of the turbulence—were approximately equal to the growth rates of the base case, and the positive triangularity configurations had growth rates noticeably lower than the base case for the same $k_y \rho_s$ range (Figure 4.3).

4.3 Section Summary

In this section, the linear stability of ITG modes for flux surface shapes with independently varied elongation and triangularity from a base case was presented. Linear simulations showed growth rates at low $k_y \rho_s$ decrease monotonically with increased elongation, positive triangularity, and negative triangularity. The trends in curvature at points along the magnetic field where the stability metric g^{yy} has local minima were predictive of the trends in growth rates for negative triangularity and large positive triangularity geometries. For elongation scans, the relationship between curvature near the g^{yy} minimum was not so clear. Quasilinear heat flux decreased for increasing elongation, positive triangularity, and negative triangularity. Additionally, the quasilinear heat flux for each positive triangularity case was lower than the negative triangularity case with the same magnitude of triangularity.

5 Nonlinear Studies

The effects of shaping on nonlinear ITG behavior is presented in this section. Nonlinear simulations were performed for triangularity and elongation scanned away from the base case described in Section 4 for $-0.75 \leq \delta \leq 0.75$ and $\kappa = 1.5$ assuming adiabatic electrons. The default resolutions for the nonlinear simulations were $nx0 \times nky0 \times nz0 \times nv0 \times nw0 = 128 \times 64 \times 32 \times 32 \times 8$ and $k_y^{\min} = 0.05$ for $\kappa = 0$, $|\delta| \leq 0.5$, $nky0 = 128$ for $\kappa = 1.5$, and $k_y^{\min} = 0.025$ for $\delta = \pm 0.75$. All simulations began with a radial box radius of $L_x = 60\rho_s$. To check for numerical convergence, three simulation parameters need to be checked: $nz0$, $nv0$, and the radial box size. The parallel spatial and parallel velocity resolutions were doubled and the box size was doubled by halving k_y^{\min} until the nonlinear heat flux changed by less than five percent. Although each case numerically converged for $nz0$, unfortunately, due to time and resource constraints, none of the nonlinear simulations numerically converged for all three criteria. However, there was evidence that most of the configurations had a nonlinear heat flux that was reasonably close to what the numerically converged value will be; this evidence is presented in this section.

The quasilinear heat flux and other quantities of interest were obtained by time averaging over the saturated state unless stated otherwise. The saturated state is when the time averaged electrostatic heat flux $\langle Q_{es} \rangle$ is in a quasi-stationary state. As with the quasilinear heat flux, $\langle Q_{es} \rangle$ has gyro-Bohm normalization. The fluctuating electrostatic potential Φ was normalized to $(T_i/e)(\rho_s/R_0)$.

5.1 Simulation Quality

Before presenting the nonlinear heat fluxes for each case, the quality of each simulation must be scrutinized, because no geometry's nonlinear simulation numerically converged for all of $nz0$, $nv0$, and k_y^{\min} . In addition to discussing for which dimensions each geometry numerically converged, two other settings will be presented. The first setting was the spectral domain size for the turbulent $\langle Q_{es} \rangle$ into both k_x and k_y modes. Because of the discretized nature of the simulation, only a finite number of wavenumbers can be considered. The spectral decomposition of heat flux should peak at low wavenumbers then decay like a power law. If $\langle Q_{es} \rangle$ is close to zero before the maximum k_x or k_y in the simulation is reached, then the simulation is not missing significant contributions to the nonlinear heat flux from higher wavenumber modes. The second setting will aid in estimating an adequate radial box size for the flux tube by estimating the number of turbulent correlation lengths per box. This was done by computing the correlation of Φ with itself between points (x,y) and $(x+\Delta x, y+\Delta y)$:

$$C(\Delta x, \Delta y) = \frac{\langle \Phi(x, y, 0)\Phi(x + \Delta x, y + \Delta y, 0) \rangle}{\langle |\Phi|^2 \rangle}. \quad (5.1)$$

It should be noted for C , the bracket notation is an ensemble average. To find the radial turbulent correlation length, C was computed for $\Delta y = 0$. A radial turbulent correlation length is defined as the width of C at a point Δx_{corr} , for which $C(\Delta x_{\text{corr}}, 0)$ has decayed by a factor of the natural number e from the maximum value of the correlation function. In each geometry, $C(\Delta x_{\text{corr}}, 0) = C(0, 0)/e$, and both C and Δx_{corr} were computed in the GENE diagnostic, `Correlations (x/y, t)`. Because strong zonal modes with little fluctuation were

present in each case, C was computed without zonal modes. If the box size is several radial turbulent correlation lengths in width, then the saturated $\langle Q_{es} \rangle$ is likely close to the numerically converged value. This section will discuss how each case has converged in $nz0$, $nv0$, and k_y^{\min} and whether the k_x , k_y , and flux tube domains were large enough such that $\langle Q_{es} \rangle$ will likely not change significantly with an increase in any domain size. This section begins with the base case, then moves on to the elongated $\kappa = 1.5$ case, and ends with the finite triangularity cases.

5.1.1 Base Case

Convergence tests for the base case were performed for the parallel spatial dimension ($nz0$) and for the simulation box size, but not for the parallel velocity dimension ($nv0$). Time traces of the nonlinear heat flux for the base case with different simulation resolutions are shown in Figure 5.1. From the saturated states of the simulations, the base case has converged in parallel spatial resolution. Additionally, the time trace for the doubled simulation domain ($k_y^{\min} = 0.025$) appears to saturate at approximately the same value of $\langle Q_{es} \rangle$ as the other time traces. To confirm or contradict convergence in k_y^{\min} , more statistics are needed for $k_y^{\min} = 0.025$, and, consequently, the simulation must be extended in time. No convergence test in for $nv0$ has been performed for the base case.

Although a higher resolution in the k_x or k_y spectrum may be needed, the simulation domain in k_x - k_y space was large enough to consider all the modes contributing significantly

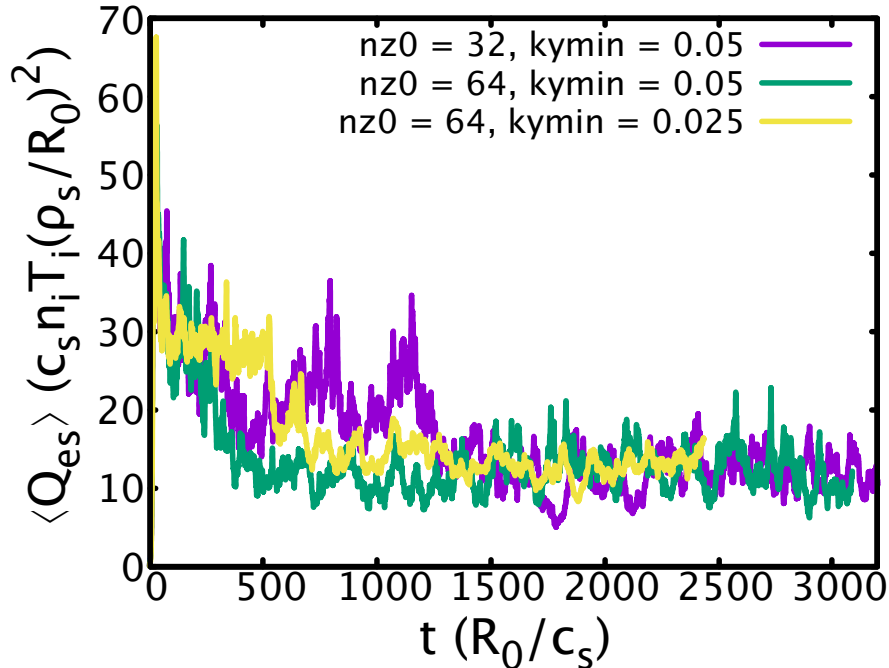


Figure 5.1: Time trace of nonlinear heat flux for the base case with $nz0 = 32, k_y^{\min} = 0.05$ (purple) and $nz0 = 64, k_y^{\min} = 0.05$ (green) showing the base case converged in the parallel spatial direction. Also the incomplete run of the base case with $nz0 = 32, k_y^{\min} = 0.025$ (yellow) is shown to illustrate convergence is likely.

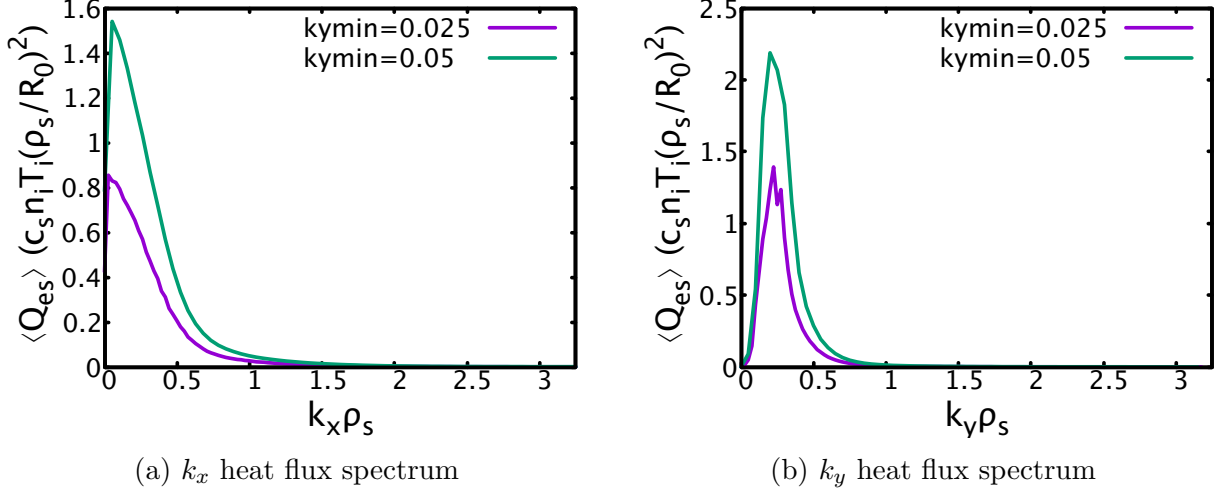


Figure 5.2: Heat flux spectra in k_x (a) and k_y (b) for the base case with $k_y^{\min} = 0.05$ (green) and $k_y^{\min} = 0.025$ (purple). With more resolution in k_x - k_y space, the maximum $\langle Q_{es} \rangle$ decreases, because the nonlinear heat flux contributions from each mode were divided into more bins in the finer resolution simulation ($k_y^{\min} = 0.025$).

to the nonlinear heat flux. In Figure 5.2, the nonlinear heat flux is broken down into contributions from k_x modes (Figure 5.2a) and from k_y modes (Figure 5.2b) for $k_y^{\min} = 0.05$ and 0.025. In Figure 5.2a, the nonlinear heat flux peaks at very low k_x then decays quickly, approaching zero by $k_x \rho_s = 2$. Any modes with k_x larger than the maximum value computed in the simulation would likely not contribute significantly to the nonlinear heat flux. A similar

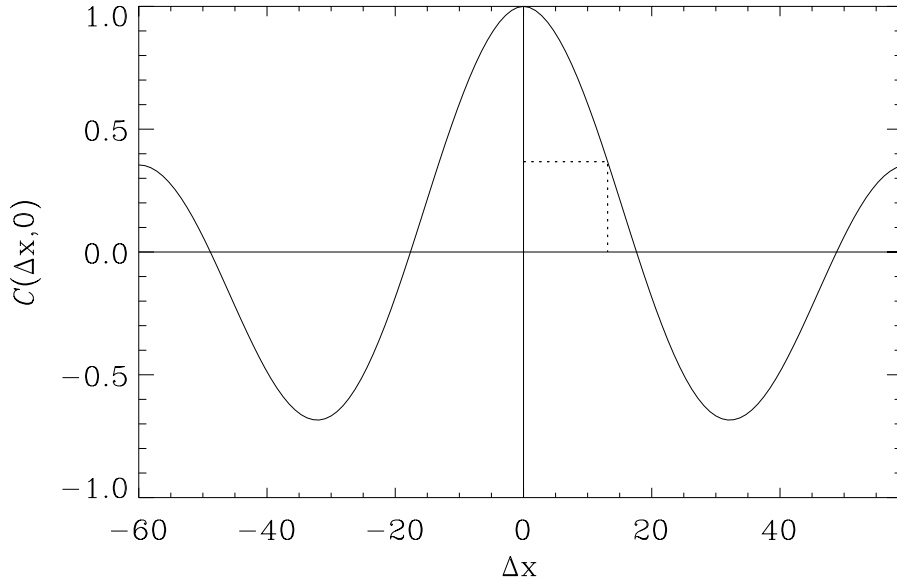


Figure 5.3: Radial correlation coefficient of Φ with itself without zonal modes for the base case $k_y^{\min} = 0.05$. The horizontal dashed line denotes the half correlation length and the vertical dashed line denotes correlation coefficient at the half correlation length.

argument can be made for the k_y spectrum in (Figure 5.2b), noting $\langle Q_{es} \rangle$ approaches zero at modes with $k_y \rho_s \lesssim 1$. Therefore, the simulations for the base case consider a large enough domain in k_x - k_y space.

To estimate if the spatial box size was large enough for convergence, the box size should contain several radial turbulent correlations. The correlation for the base case with $k_y^{\min} = 0.05$ is presented in Figure 5.3. A half correlation length is denoted by the horizontal dotted line. For the base case with $k_y^{\min} = 0.05$, the turbulent correlation length was about $25\rho_s$, so the box size contains four full radial turbulent correlation lengths. Therefore the box size for the base case with $k_y^{\min} = 0.05$ was likely large enough, and the turbulent $\langle Q_{es} \rangle$ will not likely significantly change with an increased box size. However, numerical convergence is not guaranteed.

5.1.2 Elongation

Only one elongated geometry was used in the nonlinear simulations, $\kappa = 1.5$, because of higher computational costs. In Figure 5.4 the nonlinear heat flux for the base case and $\kappa = 1.5$ is decomposed into k_x and k_y modes. The nonlinear heat flux decays quickly after peaking at low k_x for both the base case and $\kappa = 1.5$ in Figure 5.4a. The contributions from $k_x \rho_s \gtrsim 2$ were negligible, therefore the simulations for $\kappa = 1.5$ had a large enough domain in k_x space. In Figure 5.4b, the nonlinear heat flux peaks at low $k_y \rho_s$, and decays quickly as $k_y \rho_s$ increases. However, for $\kappa = 1.5$, the decay in $\langle Q_{es} \rangle$ was slower than the base case, and a larger simulation domain in k_y space was needed. Although nonlinear simulations have been done for only one elongated case, if the trend of significant nonlinear contributions from modes with large $k_y \rho_s$ is similar to the increase in growth rates at large $k_y \rho_s$ in Figure 4.1, then larger k_y domains will be needed for larger κ . Because larger k_y domains would likely be needed for larger κ , resources were concentrated on $\kappa = 1.5$ before attempting simulations of geometries with more elongation.

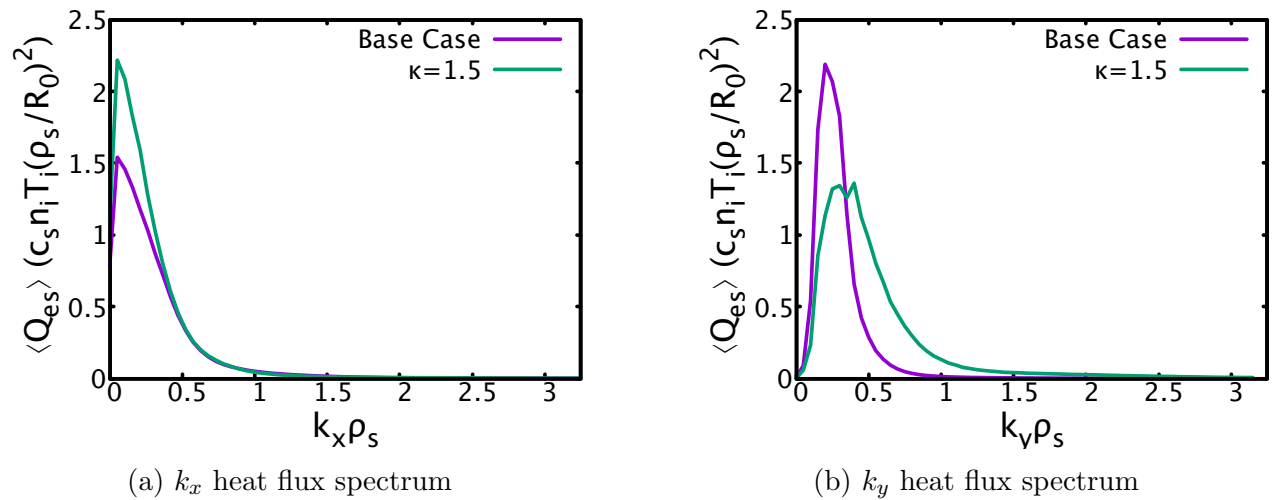


Figure 5.4: Heat flux spectra in k_x (a) and k_y (b) for the base case (purple) and $\kappa = 1.5$ (green).

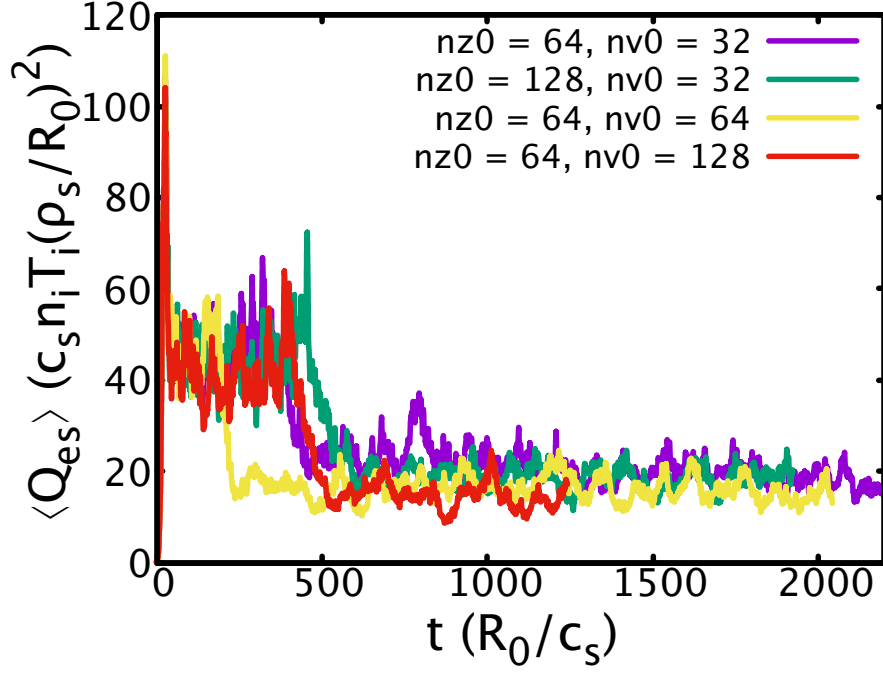


Figure 5.5: Time trace of nonlinear heat flux for $\kappa = 1.5$ with $nz0 = 64, nv0 = 32$ (purple) and $nz0 = 128, nv0 = 32$ (green), and $nz0 = 64, nv0 = 64$ (yellow). The incomplete simulation using $nz0 = 64, nv0 = 128$ (red) is included to show the parallel velocity space is likely close to convergence.

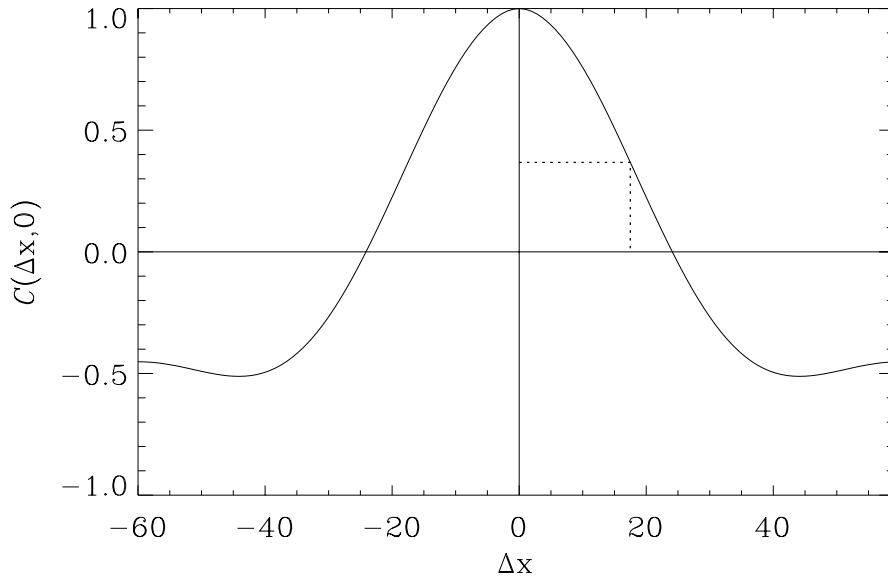


Figure 5.6: Radial correlation coefficient of Φ with itself without zonal modes for $\kappa = 1.5$ with $k_y^{\min} = 0.05$. The horizontal dashed line denotes the half correlation length and the vertical dashed line denotes correlation coefficient at the half correlation length.

Convergence in $nz0$ and $nv0$ was tested for the case with $\kappa = 1.5$. Time traces of $\langle Q_{es} \rangle$ for $\kappa = 1.5$ are presented in Figure 5.5. The saturated states of the simulations doubling $nz0$ indicate convergence in the parallel spatial coordinate for $nz0 = 64$. When $nv0$ was doubled from 32 to 64, the saturated $\langle Q_{es} \rangle$ decreased notably. Also shown is the time trace for $nv0 = 128$, with a saturated $\langle Q_{es} \rangle$ similar to $nv0 = 64$. However, to confirm convergence in the parallel velocity coordinate, more statistics are needed for the simulation with $nv0 = 128$.

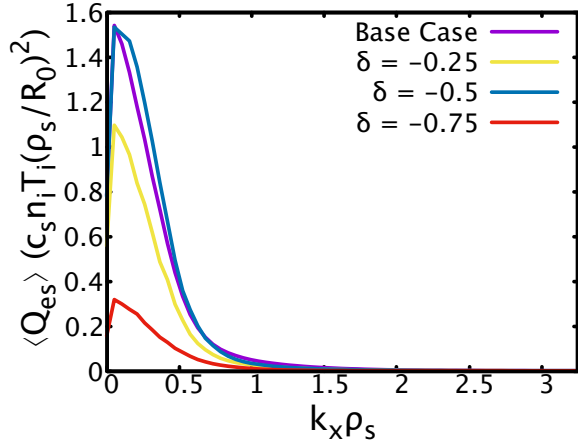
To check adequacy of box size, the correlation coefficient for the $\kappa = 1.5$ was computed and is presented in Figure 5.6. The radial turbulent correlation length, denoted by the twice the Δx value at the intersection of the dotted lines, was about $35\rho_s$. The box size contains three full radial turbulent correlation lengths, so the box size for the $\kappa = 1.5$ may be adequately large so any increase in box size will not substantially change the nonlinear heat flux.

5.1.3 Triangularity

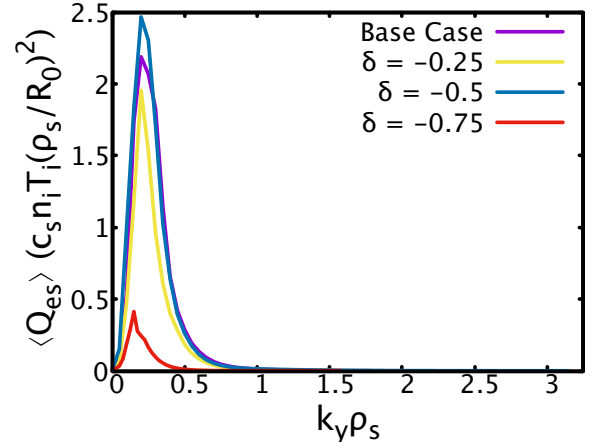
Convergence tests in $nz0$ and $nv0$ and the adequacy of the spectral domain and box sizes were checked for cases with finite triangularity in this section. The nonlinear heat flux is broken down into the k_x and k_y spectra for each finite δ configuration and the base case in Figure 5.7. In Figure 5.7a, the $\langle Q_{es} \rangle$ spectra for negative triangularity geometries peaked at low $k_x\rho_s$, then decay to essentially zero by $k_x\rho_s \lesssim 2$. The k_y spectra of $\langle Q_{es} \rangle$ for negative triangularity cases are shown in Figure 5.7b, where the nonlinear heat flux peaks at a moderately low $k_y\rho_s$, then decays to zero near $k_y\rho_s \lesssim 1$. In both the k_x and k_y heat flux spectra for negative triangularity, the cases with more negative triangularity had a faster decay in $\langle Q_{es} \rangle$ as k_x or k_y increases. Therefore, the k_x and k_y domains in the simulations were adequate for all negative triangularity nonlinear cases presented here.

In Figure 5.7c, the nonlinear heat flux spectra in k_x for geometries with positive triangularity and the base case for reference are presented. Each case peaks at a low $k_x\rho_s$, then decays quickly to zero, with cases with larger positive triangularity decaying faster. The k_y spectra for positive triangularity cases in Figure 5.7d peaked at moderately low $k_y\rho_s$ before decaying close to zero before reaching the maximum $k_y\rho_s$ used in the simulation. The case for $\delta = 0.75$ has much smaller $\langle Q_{es} \rangle$ than the other positive triangularity cases, so the nonlinear heat flux for the k_x (Figure 5.7e) and k_y (Figure 5.7f) spectra were plotted separately. The nonlinear heat flux for $\delta = 0.75$ peaks at a low $k_x\rho_s$ and decays quickly like the other cases. However, there was a second region of finite nonlinear heat flux for $1 \lesssim k_x\rho_s \lesssim 2$ before decaying to a negligible amount before the k_x domain ends. The k_y nonlinear heat flux spectrum for $\delta = 0.75$ sees two peaks with rapid decays: one near $k_y\rho_s \approx 0.25$ and another near $k_y\rho_s \approx 2.5$. After the second peak, $\langle Q_{es} \rangle$ decays rapidly to a negligible amount near $k_y\rho_s = 0.6$. Therefore, the nonlinear simulations for positive triangularity use a large enough k_x and k_y spectrum.

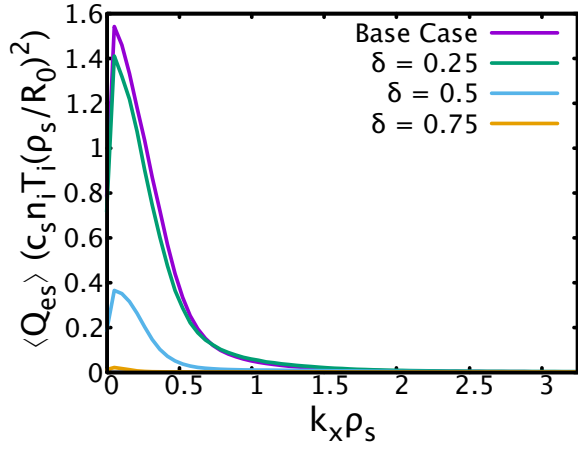
For the $\delta = 0.25$ case, the time traces of nonlinear heat flux are presented in Figure 5.8. Although the two traces do not match up exactly, the time averaged electrostatic heat flux over the saturated regime differs by less than three percent. The two traces show a convergence in $nz0$. No traces for higher parallel velocity resolution or halving k_y^{\min} have been performed for $\delta = 0.25$.



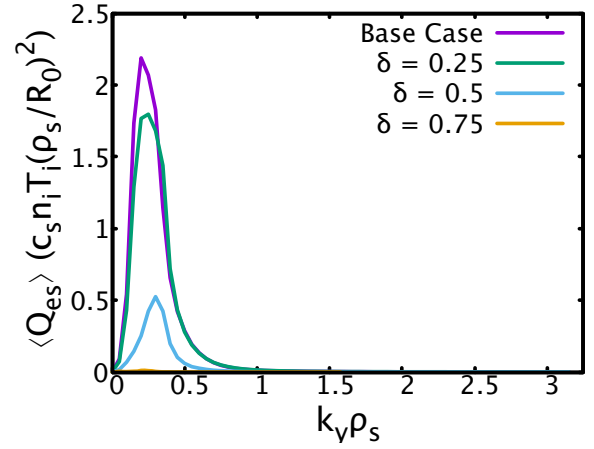
(a) k_x heat flux spectrum of negative δ .



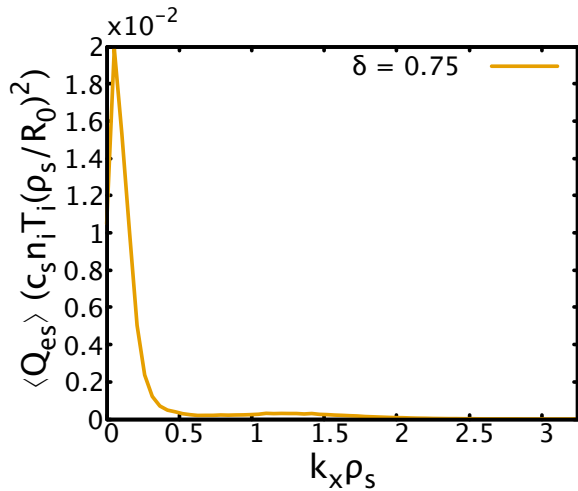
(b) k_y heat flux spectrum of negative δ .



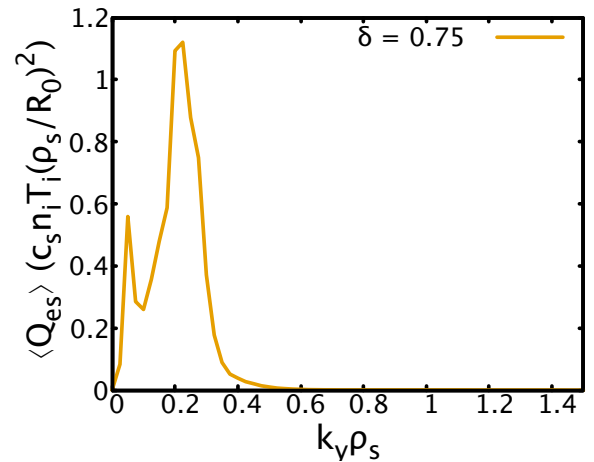
(c) k_x heat flux spectrum of positive δ .



(d) k_y heat flux spectrum of positive δ .



(e) k_x heat flux spectrum of $\delta = 0.75$



(f) k_y heat flux spectrum of $\delta = 0.75$

Figure 5.7: Heat flux spectra for negative triangularity geometries in k_x (a) and k_y (b) for the base case (purple), $\delta = -0.25$ (yellow), $\delta = -0.5$ (dark blue), and $\delta = -0.75$ (red), and for positive triangularity geometries in k_x (c) and k_y (d) for the base case (purple), $\delta = 0.25$ (green), $\delta = 0.5$ (light blue), and $\delta = 0.75$ (orange). Because the nonlinear heat flux is much smaller, separate figures are shown for the k_x (e) and k_y (f) spectra for $\delta = 0.75$.

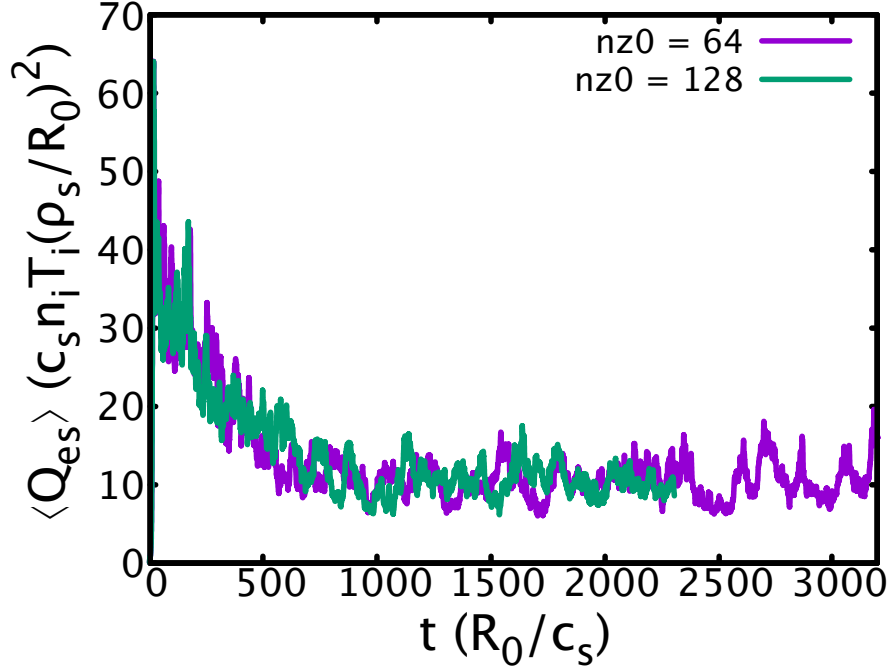


Figure 5.8: Time trace of nonlinear heat flux for $\delta = 0.25$ with $nz0 = 64$ (purple) and $nz0 = 128$ (green) to illustrate convergence in the parallel spatial resolution.

The only convergence test performed for the $\delta = 0.5$ case was for the parallel spatial coordinate. The time traces of nonlinear heat flux for the case with $\delta = 0.5$ is shown in Figure 5.9. In the saturated regions, both time traces appeared to have a base line of approximately the same value of $\langle Q_{es} \rangle \approx 1$ and quasi-periodic spikes in nonlinear heat flux to $\langle Q_{es} \rangle \approx 7$, lasting a couple hundred time units. It is unknown if the quasi-periodic spikes in nonlinear heat flux were a property of this shaping or an indication that higher resolutions or larger box sizes are needed. Although the saturated regions for the two traces appear similar, for $nz0 = 128$ more statistics are needed for an accurate $\langle Q_{es} \rangle$ before confirming convergence for $nz0$.

For $\delta = 0.75$, convergence tests in $nz0$ and $nv0$ were performed. Time traces of $\langle Q_{es} \rangle$ for $nz0 = 64$ and $nz0 = 128$ show convergence in $nz0$, despite the $nz0 = 64$ simulation took nearly 2000 time units to reach a quasi-stationary state and the $nz0 = 128$ simulation reached a saturated state by 500 time units. The time trace for $nv0 = 64$ has a saturated nonlinear heat flux half that of the other cases with $nv0 = 32$, indicating a higher resolution in parallel velocity is needed. Additionally, any future convergence tests may need the convergence criteria relaxed. The saturated nonlinear heat fluxes were so low (0.14 for $nv0 = 32$ and 0.07 for $nv0 = 64$) that machine precision errors and the choice of where the saturated state begins may alter the saturated $\langle Q_{es} \rangle$ by more than five percent.

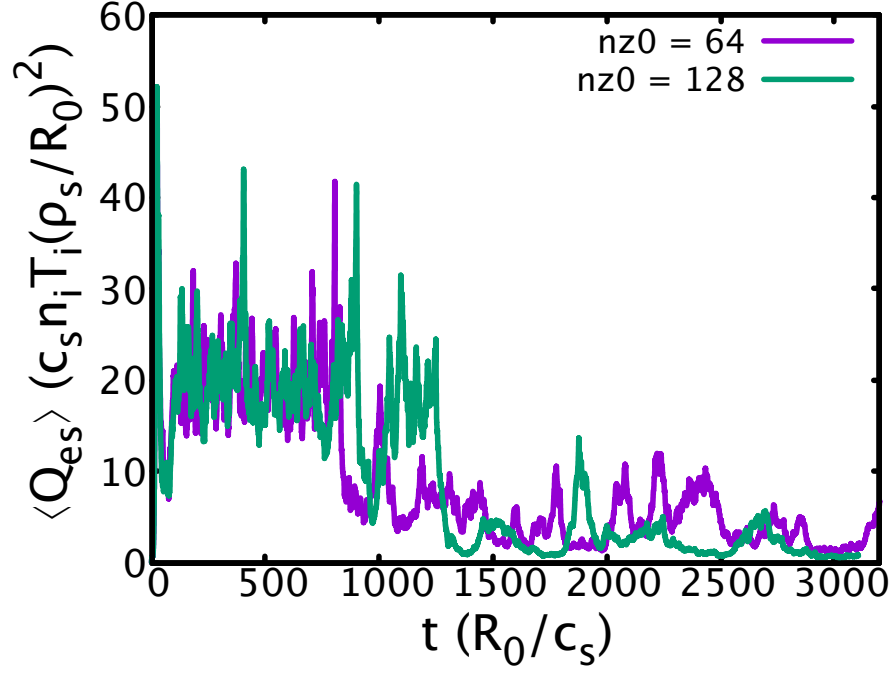


Figure 5.9: Time trace of nonlinear heat flux for $\delta = 0.5$ with $nz0 = 64$ (purple) and $nz0 = 128$ (green) to show the relative insensitivity to parallel spatial resolution and large quasi-periodic change in nonlinear heat flux.

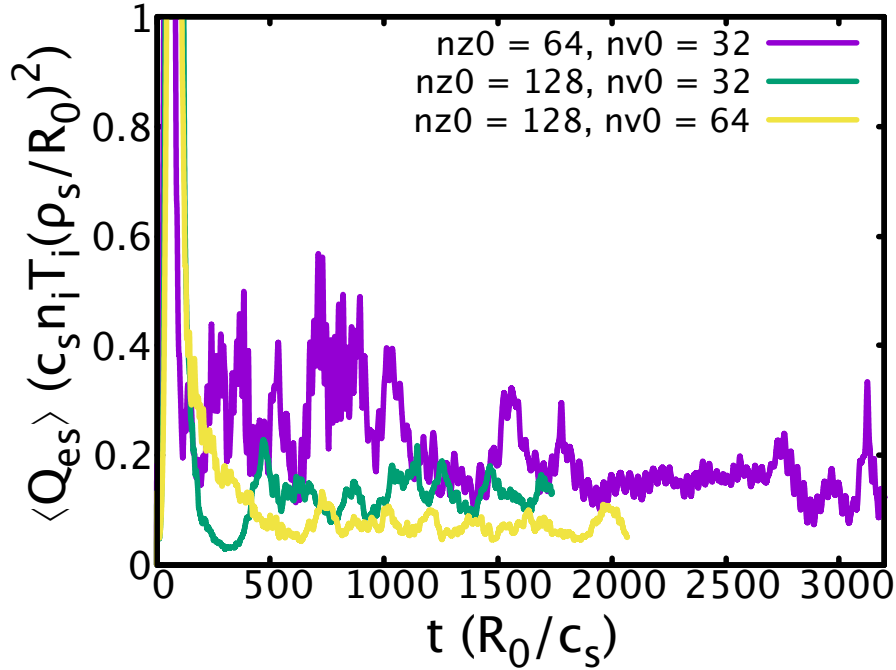


Figure 5.10: Time trace of nonlinear heat flux for $\delta = 0.75$ with $nz0 = 64, nv0 = 32$ (purple) and $nz0 = 128, nv0 = 32$ (green), and $nz0 = 64, nv0 = 64$ (yellow). For $nz0 = 64, nv0 = 32$, the saturated state begins at about $t/(c_s/R_0) = 2000$, and the saturated state for $nz0 = 128, nv0 = 32$ begins around $t/(c_s/R_0) = 400$.

The time traces for convergence tests in $nz0$ for $\delta = -0.25$ are presented in Figure 5.11. For all three traces, each doubling the resolution of $nz0$ of the last, the saturated region began at about 500 time units and showed quasi-periodic spikes in $\langle Q_{es} \rangle$ similar to the $\delta = 0.5$ case (Figure 5.9). Like with $\delta = 0.5$, for $\delta = -0.25$ there appears to be a relative insensitivity of saturated $\langle Q_{es} \rangle$ with $nz0$, and it is unclear if the quasi-periodic increases in $\langle Q_{es} \rangle$ were related to the simulation settings or the geometry.

The case of $\delta = -0.5$ was tested for convergence in $nz0$ and $nv0$, with the time traces of nonlinear heat flux given in Figure 5.12. The traces for $nz0 = 64, nv0 = 32$ and $nz0 = 128, nv0 = 32$ indicate convergence in the parallel spatial coordinate resolution. When $nv0$ was doubled to 64, the saturated nonlinear heat flux decreased significantly. When $nv0$ was doubled again to 128, the simulation did not saturate, but the simulation appears to be decreasing to a $\langle Q_{es} \rangle$ almost half of the saturated $\langle Q_{es} \rangle$ for $nv0 = 64$. To confirm convergence in $nv0$, the simulation with $nv0 = 128$ must be continued, and another simulation with $nv0 = 256$ must have a saturated $\langle Q_{es} \rangle$ with five percent of that of $nv0 = 128$.

The last case of finite triangularity discussed in this section is $\delta = -0.75$, where convergence in $nz0$ and $nv0$ was tested. The configuration with $\delta = -0.75$ converged in $nz0$, as seen from the time traces of nonlinear heat flux in Figure 5.13. Although the time trace of $\langle Q_{es} \rangle$ for $nv0 = 64$ appears to have saturated at the same level as the other traces with $nv0 = 32$, the simulations with $nv0 = 32$ had a nonlinear heat fluxes larger by almost 15 percent. Further convergence tests in $nv0$ are needed for $\delta = -0.75$.

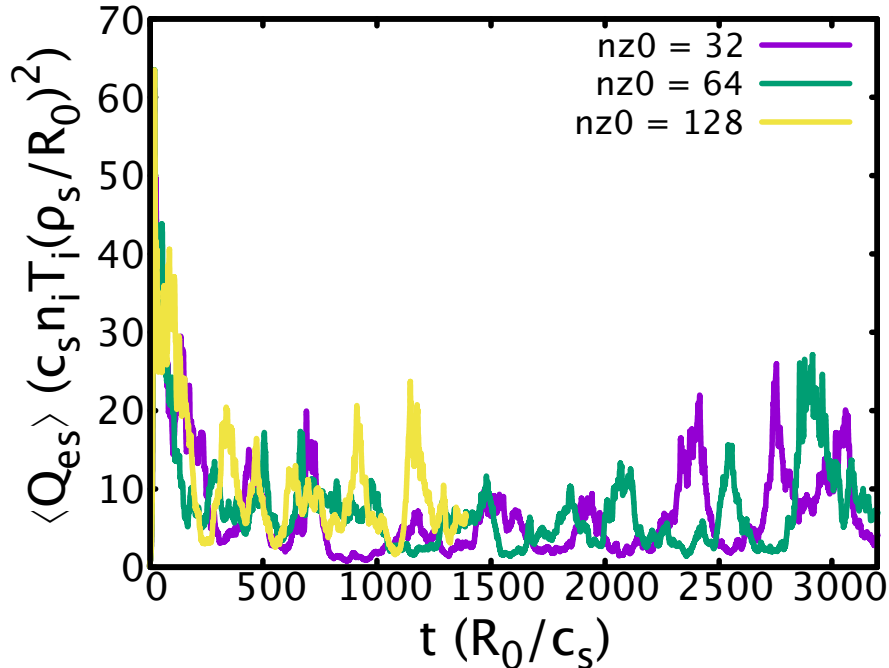


Figure 5.11: Time trace of nonlinear heat flux for $\delta = -0.25$ with $nz0 = 32$ (purple) and $nz0 = 64$ (green), $nz0 = 128$ (yellow) is shown to illustrate the relative insensitivity to parallel spatial resolution and large quasi-periodic change in nonlinear heat flux.

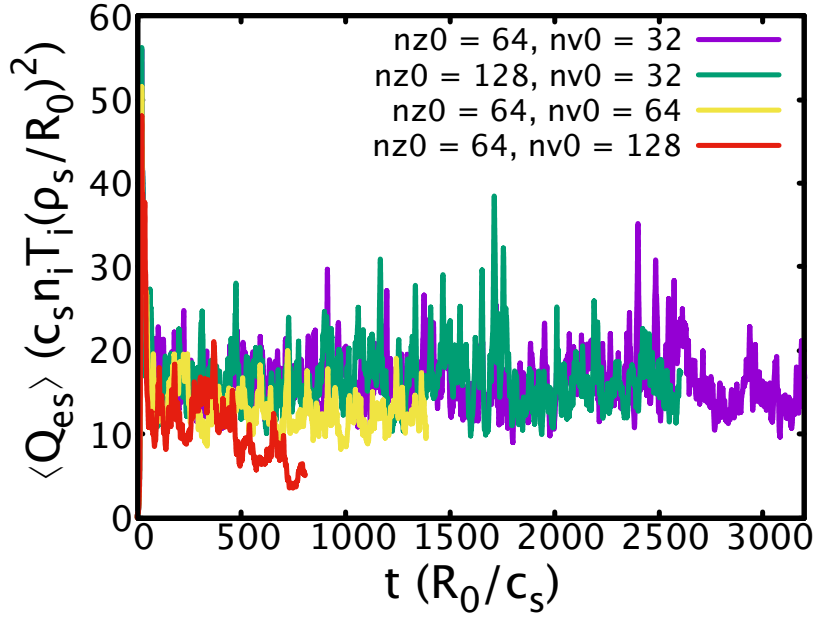


Figure 5.12: Time trace of nonlinear heat flux for $\delta = -0.5$ with $nz0 = 64, nv0 = 32$ (purple) and $nz0 = 128, nv0 = 32$ (green), is shown to illustrate convergence in the parallel spatial resolution. The simulations for $nz0 = 64, nv0 = 64$ (yellow) and $nz0 = 64, nv0 = 128$ (red) are plotted to show a higher parallel velocity resolution is needed.

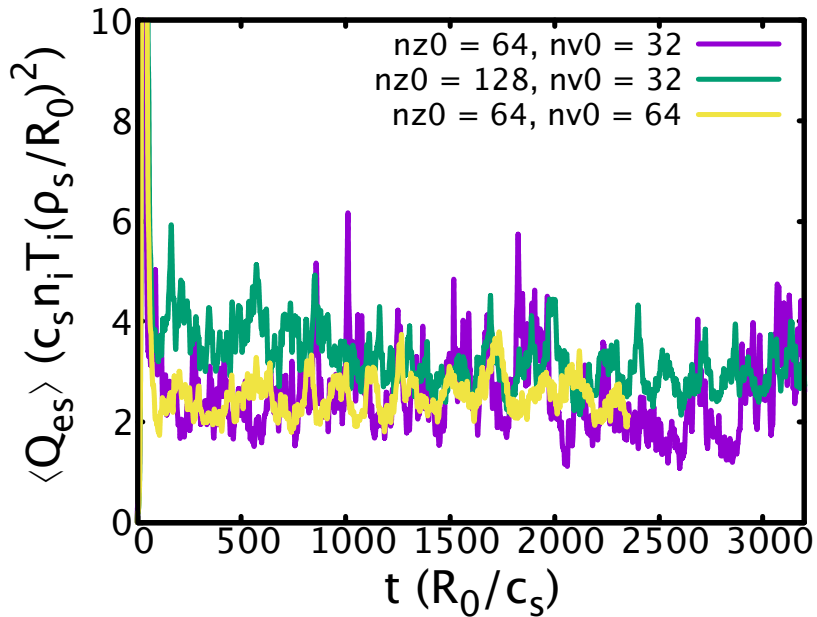


Figure 5.13: Time trace of nonlinear heat flux for $\delta = -0.75$ with $nz0 = 64, nv0 = 32$ (purple) and $nz0 = 128, nv0 = 32$ (green), is shown to illustrate convergence in the parallel spatial resolution. The simulation for $nz0 = 64, nv0 = 64$ (yellow) is also plotted to show the simulation likely converged for the parallel velocity.

None of the finite δ cases were checked for numerical convergence by doubling the box size, so the adequacy of the box sizes for each triangularity case was estimated by the number of radial turbulent correlation lengths in the simulation domain. The correlation coefficient for each finite triangularity case is presented in Figure 5.14. For $\delta = 0.25$ (Figure 5.14a) and $\delta = 0.25$ (Figure 5.14b), the radial turbulent correlation lengths were both about $30\rho_s$, meaning the box for both cases was about four full radial turbulent correlation lengths

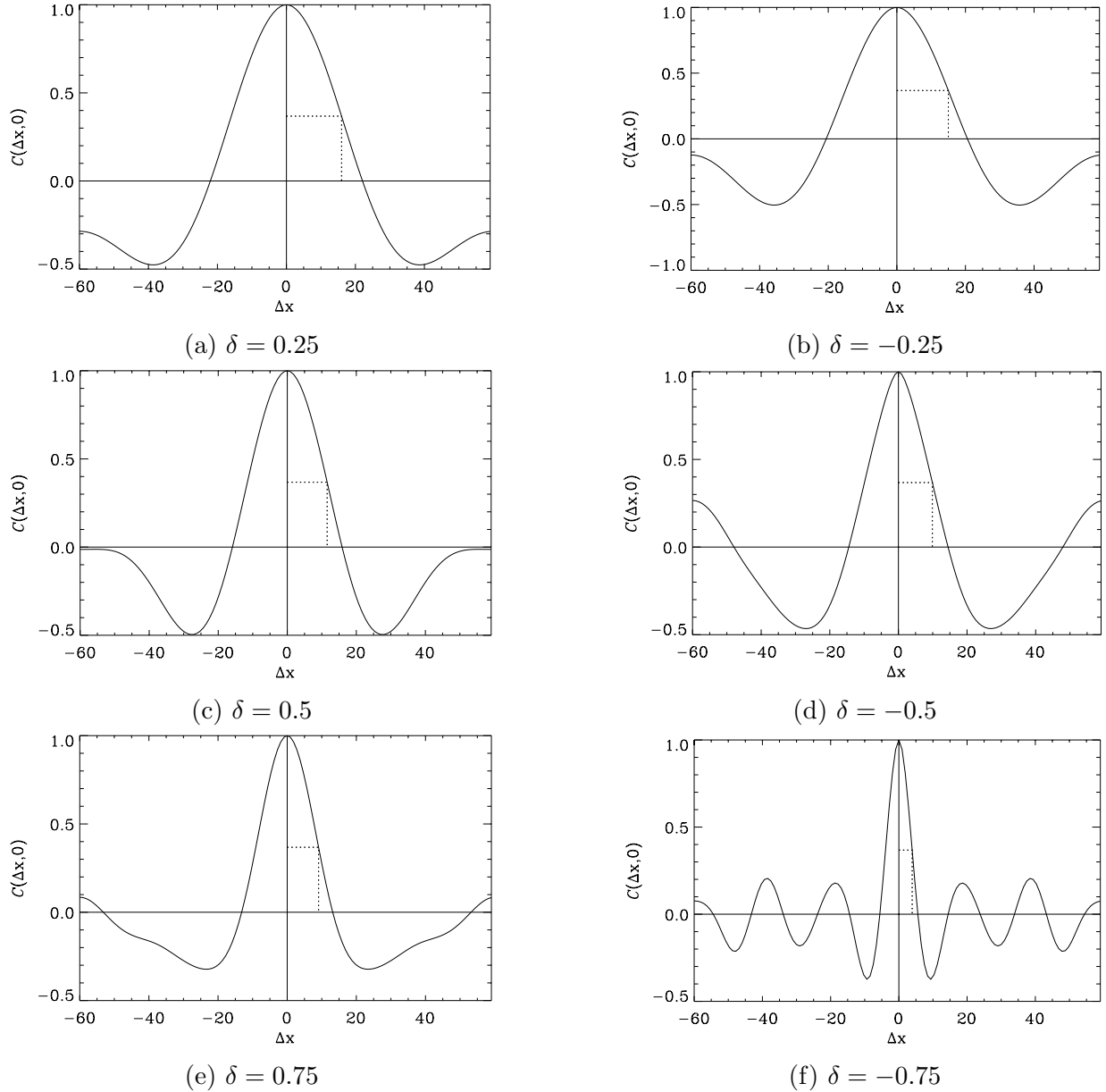


Figure 5.14: Radial correlation coefficient of Φ with itself without zonal modes for (a) $\delta = 0.25$, (c) $\delta = 0.5$, (e) $\delta = 0.75$, (b) $\delta = -0.25$, (d) $\delta = -0.5$, (f) $\delta = -0.75$. The horizontal dashed line denotes the half correlation length and the vertical dashed line denotes correlation coefficient at the half correlation length.

in width. The cases $\delta = 0.5$ (Figure 5.14c) and $\delta = -0.5$ (Figure 5.14d) both had radial turbulent correlation lengths of about $22\rho_s$, and the box size for $\delta = 0.5$ and $\delta = -0.5$ contain five full radial turbulent correlation lengths. The radial turbulent correlation length for the case with $\delta = 0.75$ in Figure 5.14e was a little less than $20\rho_s$, therefore six full correlation lengths can fit in the simulation box. For $\delta = -0.75$, the radial turbulent correlation length, shown in Figure 5.14f, was about $10\rho_s$, which was the smallest of any geometry explored in this thesis. The radial box size for $\delta = -0.75$ can fit about 12 radial turbulent correlation lengths. Therefore, the box size of every finite triangularity case was likely large enough that the convergence check of halving k_y^{\min} would not significantly change the nonlinear heat flux.

5.2 Nonlinear Heat Flux

In this section non-converged nonlinear heat fluxes from the base case, $\kappa = 1.5$, and $-0.75 \leq \delta \leq 0.75$ are given and compared with the quasilinear heat fluxes presented in Section 4.2. Additionally, an analysis of mode strengths is presented in an attempt to provide physical explanations for the differences in nonlinear heat fluxes for each geometry. A summary of Q_L and $\langle Q_{es} \rangle$ are given in Table 5.1 along with the parallel spatial and parallel velocity resolutions and k_y^{\min} of the simulation from which the nonlinear heat flux value was obtained. By choice, the quasilinear and nonlinear heat fluxes of the base case were chosen to be equal. For the case $\kappa = 1.5$, the nonlinear heat flux was about 1.7 times greater than the quasilinear heat flux for the same geometry, with convergence only in $nz0$.

The nonlinear and quasilinear heat fluxes for each finite δ case is presented in Figure 5.15. The quasilinear heat flux exhibits a monotonic decrease with increased triangularity—both positive and negative. The non-converged nonlinear heat fluxes also show a general decrease with increasing triangularity. The stray case was $\delta = -0.5$, where the converged nonlinear heat flux is likely significantly lower than the value reported in Table 5.1. This is reasonable to assume, because if the end of the time trace for $nv0 = 128$ in Figure 5.12 is the value of

Geometry	Q_L	$\langle Q_{es} \rangle$	Nonlinear Resolution ($nz0, nv0, k_y^{\min}$)
Base Case	11.61	11.61	(32, 32, 0.05)
$\kappa = 1.5$	9.58	16.3	(64, 64, 0.05)
$\delta = -0.75$	4.54	2.51	(64, 64, 0.025)
$\delta = -0.5$	8.02	12.39	(64, 64, 0.05)
$\delta = -0.25$	10.33	5.63	(32, 32, 0.05)
$\delta = 0.25$	10.12	10.77	(64, 32, 0.05)
$\delta = 0.5$	6.68	3.05	(64, 32, 0.05)
$\delta = 0.75$	2.66	0.07	(128, 64, 0.025)

Table 5.1: Comparison of quasilinear and nonlinear heat fluxes for each configuration with a nonlinear simulation performed and the $nz0$, $nv0$, and k_y^{\min} settings for the simulation from which the nonlinear heat flux was calculated. The quasilinear heat flux for the base case was chosen to be equal to the nonlinear heat flux of the base case to set \mathcal{C} for each quasilinear heat flux.

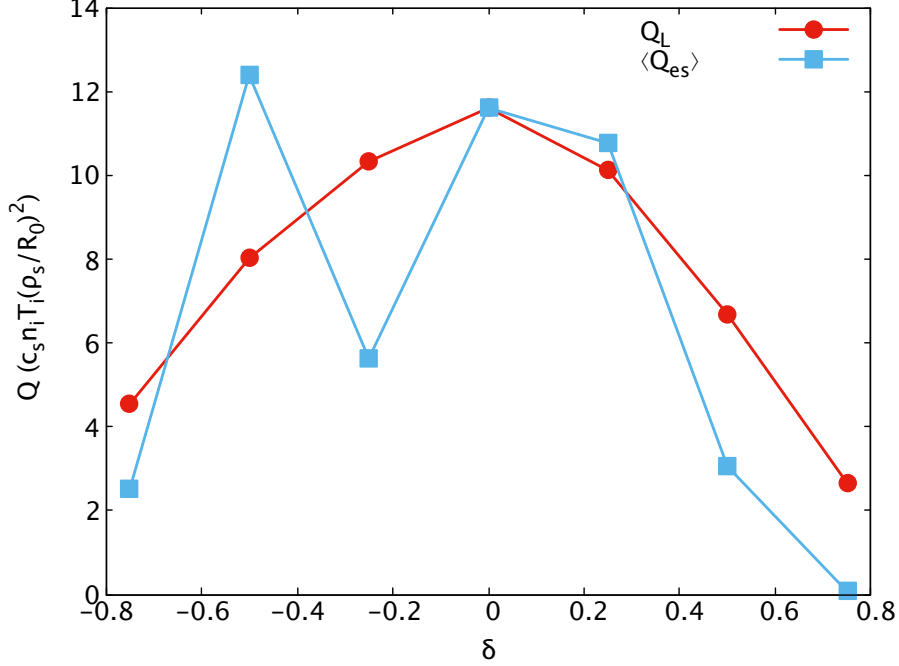


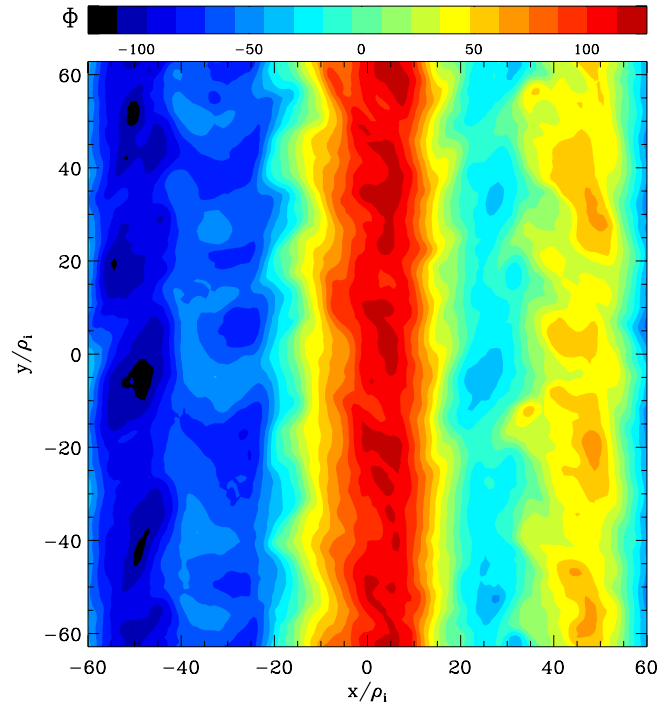
Figure 5.15: Quasilinear and nonlinear heat fluxes varying triangularity from Table 5.1. All nonlinear heat fluxes were likely close to the converged values except $\delta = -0.5$, which, from Figure 5.12, is probably closer to five.

the saturated $\langle Q_{es} \rangle$, the nonlinear heat flux would be around five. Taking this into account, it is likely that the nonlinear heat flux would monotonically decay with increasing positive and negative triangularity.

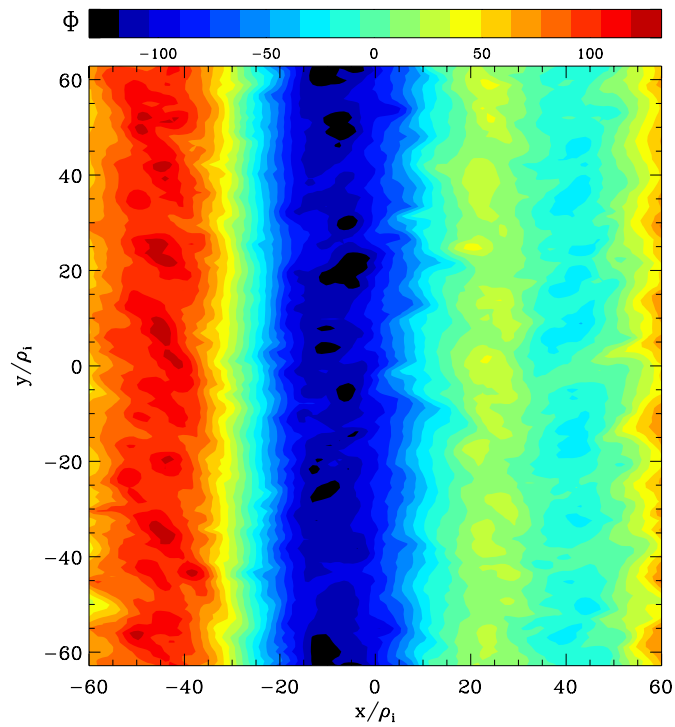
Though the qualitative trends of nonlinear and quasilinear heat flux with triangularity likely agree, there was little quantitative agreement between the two metrics. Excluding the base case and $\delta = -0.5$, all cases other than $\delta = 0.25$ had quasilinear heat fluxes at least twice as large as the nonlinear heat fluxes, with Q_L for $\delta = 0.75$ being 38 times greater than $\langle Q_{es} \rangle$. The quasilinear and nonlinear heat fluxes for the case of $\delta = 0.25$ differ by less than ten percent.

Some physical insight into why the case $\kappa = 1.5$ had larger nonlinear heat flux than the base case may be gained through the electrostatic potential contours of both cases, shown in Figure 5.16. The contours shown in Figure 5.16 were taken at the last time step in the simulation. In Figure 5.16a, the magnitude of Φ is plotted in the x - y simulation domain for the base case. Four distinct bands of alternating positive and negative potential nearly uniform in the binormal direction indicate strong zonal flows. In Figure 5.16b, the contours of Φ for the $\kappa = 1.5$ case have many jagged radial elongations. Because plasma particles drift along lines of constant electrostatic potential in accordance to the $\mathbf{E} \times \mathbf{B}$ drift, the local radial elongations in the contours of Φ allows for charged particles to stream more freely radially out of the simulation domain, leading to a larger nonlinear heat flux compared to the base case.

The local radial elongations in Φ in the $\kappa = 1.5$ case are typically sheared away with sufficiently strong zonal flows, and a decrease in zonal flow strength for $\kappa = 1.5$ relative to



(a) Base Case



(b) $\kappa = 1.5$

Figure 5.16: Contours of Φ for the base case (a) and $\kappa = 1.5$ (b) taken at the last time step of the simulation.

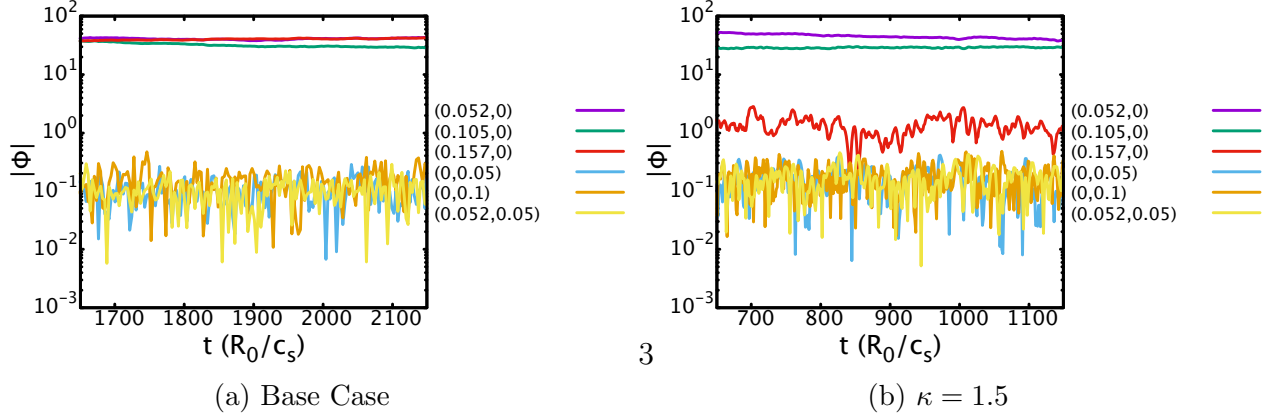


Figure 5.17: Time traces of the magnitude of electrostatic potential of several zonal and nonzonal modes for nonlinear simulations of (a) the base case, (b) $\kappa = 1.5$. The modes are denoted with (k_x, k_y) where zonal modes have $k_x \neq 0, k_y = 0$. Each subfigure depicts the same sized time domains and range of $|\Phi|$ values.

the base case could explain the local radial elongations of Φ in Figure 5.16b. In Figure 5.17, the mode amplitude for electrostatic potential of several zonal and nonzonal modes for low k_x and k_y are shown for the base case and $\kappa = 1.5$. The zonal modes, $k_x \neq 0, k_y = 0$, for the base case (Figure 5.17a) were about 100 times stronger than the nonzonal modes. Higher mode numbers had lower amplitudes, decaying to amplitudes similar to the nonzonal modes shown as wavenumbers increase; the higher wavenumber modes are not shown for the sake of clarity. In Figure 5.17b, time trace of $|\Phi|$ for low mode numbers are shown. As with Figure 5.17a, the zonal modes (0.052,0) and (0.105,0) were about 100 times stronger than the other nonzonal modes. However, the zonal mode (0.157,0) was only 10 times stronger than the nonzonal modes. This provides evidence that some zonal modes were not as strong at higher elongations.

For finite the triangularity cases, the relative strengths of zonal modes to nonzonal modes do not correlate inversely with nonlinear heat flux, as might be expected. The time traces of electrostatic potential amplitude for low k_x and low k_y zonal and nonzonal modes for each finite triangularity case is presented in Figure 5.18. Although only modes with low k_x and low k_y are shown, modes with higher wavenumbers decay in amplitude as wavenumber increases and are not shown for clarity. For $\delta = 0.25$ (Figure 5.18a) and $\delta = -0.25$ (Figure 5.18b), the lowest two wavenumber zonal modes had amplitudes about 100 times larger than nonzonal modes, like the base case, but the higher wavenumber zonal modes were about ten times larger than the nonzonal modes. For $\delta = 0.5$ (Figure 5.18c) and $\delta = -0.5$ (Figure 5.18d), the zonal modes were about 100 times as strong as the nonzonal modes, and all modes were similar in strength the the same modes in the base case (Figure 5.17a). Although the zonal modes for $\delta = 0.75$, shown in Figure 5.18e, were also about 100 times stronger than the nonzonal modes, all mode strengths were an order of magnitude less than the base case mode strengths. In Figure 5.18f, several low wavenumber mode amplitudes are shown for $\delta = -0.75$, where the zonal mode strengths were less than an order of magnitude higher than the nonzonal modes. Only considering relative mode strength of zonal modes to nonzonal modes, the nonlinear heat fluxes for $\delta = 0.25$ and $\delta = -0.25$ would be larger than the

base case, for $\delta = 0.5$, $\delta = -0.5$, and $\delta = 0.75$ nonlinear heat fluxes would be similar to the base case nonlinear heat flux, and $\delta = -0.75$ would have a higher nonlinear heat flux. However, the nonlinear heat fluxes do not correlate with the relative strength of zonal modes to nonzonal modes and cannot explain the trends in nonlinear heat flux with finite triangularity cases.

Although the relative zonal mode magnitude to nonzonal mode magnitudes were similar for the base case and $\delta = 0.75$, the nonlinear heat flux for the $\delta = 0.75$ case was nearly zero; one possible explanation is the case $\delta = 0.75$ may be in a Dimits region. A Dimits region is a range of temperature gradients between the critical temperature gradient for linear instability R_0/L_{Tcrit} and $R_0/L_{Tcrit} + \Delta_{Dimits}$, where Δ_{Dimits} is the Dimits shift. The Dimits shift is a numerical phenomena of a nonlinear upshift in the threshold for collisionless, electrostatic ITG turbulence [29]. The Dimits shift is caused by zonal flows that are sufficiently strong to suppress linear ITG modes yet weak enough to be stable; for temperature gradients larger than the Dimits shifted critical temperature $R_0/L_{Tcrit} + \Delta_{Dimits}$, nonlinear suppression of turbulence impossible [51]. There are several indications that the case for $\delta = 0.75$ may be within a Dimits region. First, zonal modes had an electrostatic potential magnitude about 100 times larger than the nonzonal modes (Figure 5.18e), suggesting large suppression of turbulence by zonal modes for all cases except $\delta = -0.75$. Additionally, the amplitude of the two lowest k_x zonal modes and all nonzonal modes for $\delta = 0.75$ was about ten times lower than every geometry other than $\delta = -0.75$, and every case but $\delta = 0.75$ has $\langle Q_{es} \rangle$ significantly larger than zero. It follows that every geometry (again, except $\delta = -0.75$) has strong suppression of turbulence by zonal flows, but only for $\delta = 0.75$ was the strength of the zonal modes weak enough to keep the simulation nearly nonlinearly stable. However, a temperature gradient scan would be needed to conclude whether or not $\delta = 0.75$ is in a Dimits region.

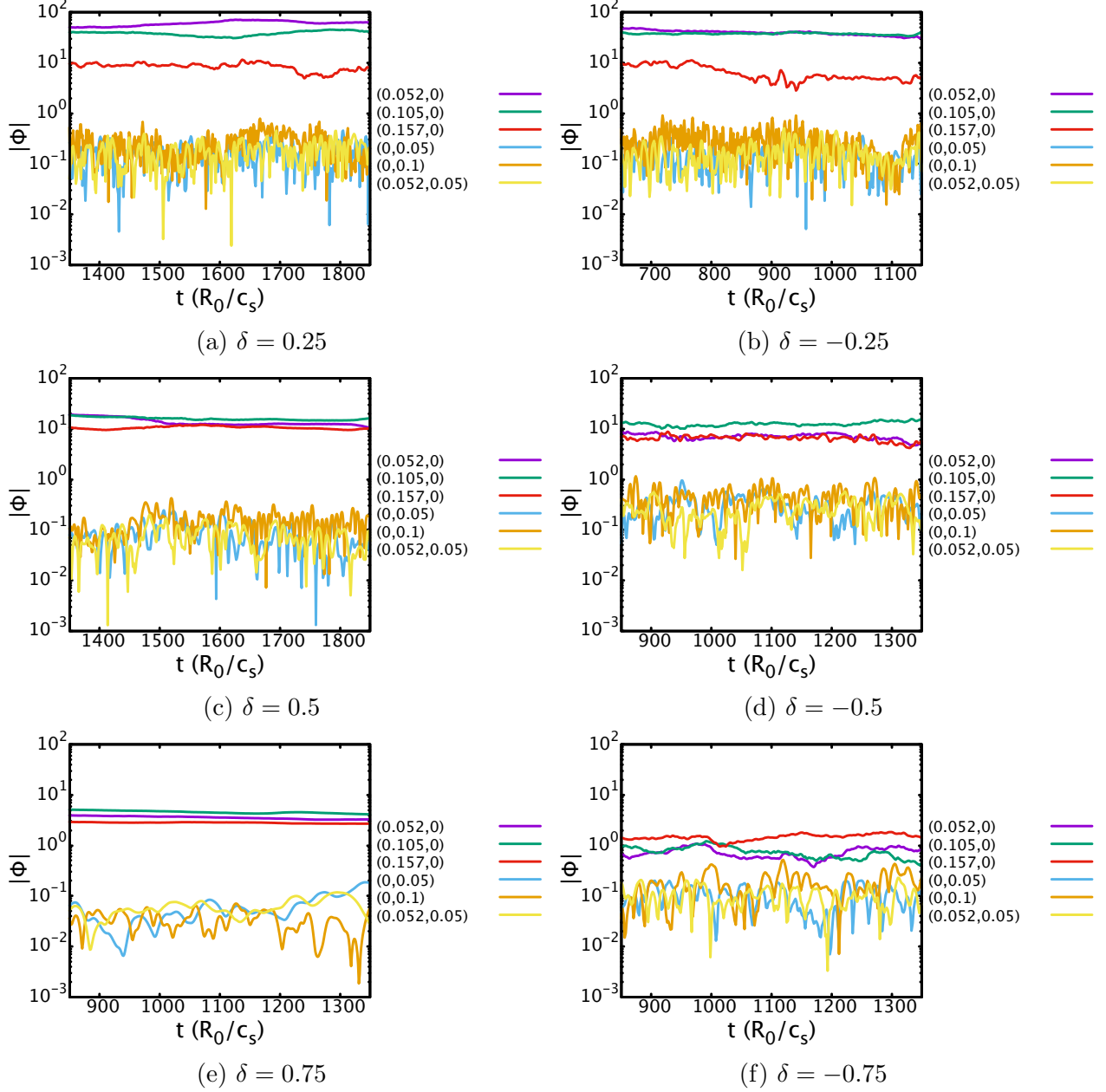


Figure 5.18: Time traces of the magnitude of electrostatic potential of several zonal and nonzonal modes for nonlinear simulations of (a) $\delta = 0.25$, (b) $\delta = -0.25$, (c) $\delta = 0.5$, (d) $\delta = -0.5$, (e) $\delta = 0.75$, and (f) $\delta = -0.75$. The modes are denoted with (k_x, k_y) where zonal modes have $k_x \neq 0, k_y = 0$. Each subfigure depicts the same sized time domain and range of $|\Phi|$ values.

5.3 Section Summary

In this section, the nonlinear simulations of the base case, $\kappa=1.5$, and the six finite δ cases were presented. All cases converged numerically for the parallel spatial direction, but none of the cases converged for all three metrics: $nz0$, $nv0$, and k_y^{\min} . Additionally,

the k_x - k_y domain for each case was large enough to account for all modes with significant contributions to $\langle Q_{es} \rangle$, and the box size of the flux tubes for each case were several radial turbulent correlation lengths in width, thus the box size was likely appropriate for each case. The nonlinear heat flux was presented and showed $\kappa = 1.5$ had a larger $\langle Q_{es} \rangle$ than the base case, disagreeing with quasilinear heat flux trends for elongation. For $\kappa = 1.5$, the contours of Φ had local radial elongations which correlated with weaker zonal modes. The nonlinear heat flux had an almost monotonic decrease in nonlinear heat flux with increasing triangularity. For $\delta = -0.5$, a simulation with a larger $nv0$ than the simulation for the $\langle Q_{es} \rangle$ presented indicates the nonlinear heat flux will likely fit the monotonic trend in $\langle Q_{es} \rangle$ with δ , agreeing with the quasilinear heat flux trends. The nonlinear heat fluxes for finite triangularity cases were often significantly lower than the corresponding quasilinear heat fluxes. It was shown that the trend of decreasing in $\langle Q_{es} \rangle$ with increasing triangularity cannot be fully explained by relative amplitudes of zonal modes to nonzonal modes. In addition, there is some evidence the case $\delta = 0.75$ was in a Dimits region, which would explain the near absence of nonlinear heat flux, however that evidence was not conclusive.

6 Conclusions

The work in this thesis is an update and expansion on previous ion temperature gradient turbulence tokamak shaping studies. Linear simulations investigated more extreme shaping cases than previously done [40, 42, 43]. Further, the relationship between curvature and a stability metric with linear growth rates has been discussed for the first time. Nonlinear simulations presented in this thesis accounted for more physics than the studies using a linear heat flux approximation [40, 42–44]. Finally, the first comparison of the trends in nonlinear and quasilinear heat fluxes with elongation and triangularity were performed. Unfortunately, the nonlinear simulations have not converged numerically, but evidence was presented showing most cases had a nonlinear heat flux that was likely reasonably close to the converged values. The key conclusions are summarized and future research directions are recommended in this section.

6.1 Summary

6.1.1 Linear Studies

Although a linear stability analysis and quasilinear heat calculations for ITG modes varying tokamak flux surface shaping are not novel, the work in this thesis investigated geometries with more shaping than previously done and compared trends in curvature with trends in growth rates. For geometries with elongation added to the base case, as elongation increased, the maximum growth rate increased and shifted to larger $k_y \rho_s$ and the growth rates at low $k_y \rho_s$ decreased. The trend in curvature for elongated geometries near the mode location along the magnetic field line correlated inversely with growth rates at low $k_y \rho_s$, which was consistent with how curvature is expected to affect ITG drift waves. However, the curvature trend for elongated geometries near the mode location directly correlates with the maximum growth rates, which was inconsistent with how curvature is expected to affect ITG drift wave instabilities. For positive triangularity at $\delta = 0.5$ or greater, both maximum growth rates and growth rates at low $k_y \rho_s$ decrease, which correlated with changes in the curvature trends at mode locations. As negative triangularity was increased, the maximum growth rates and some of the growth rates at low $k_y \rho_s$ decreased. The trend in growth rates for negative triangularity could not strictly be correlated with changes in curvature at mode locations, because the curvature changed little near the mode locations. The quasilinear heat flux calculations indicated as more shaping was added, Q_L decreased. The decrease in Q_L appeared to have a linear dependence with increasing elongation. The trend of Q_L with increased triangularity had almost a negative parabolic shape with the maximum quasilinear heat flux at the base case. Additionally, positive triangularity had lower values of Q_L than their negative counterparts.

6.1.2 Nonlinear Studies

In this thesis, the first scans of elongation and triangularity with nonlinear gyrokinetic studies for a nonlinear heat flux were presented. Although the nonlinear simulations did not numerically converge, evidence presented showed whether the nonlinear simulations gave reasonable or unreasonable values of saturated $\langle Q_{es} \rangle$. Additionally, the nonlinear heat fluxes

were compared to quasilinear heat flux estimations for different tokamak shaping for the first time. While the trends for nonlinear and quasilinear heat flux with elongation did not agree, the increase in nonlinear heat flux correlated with local radial elongations in the $|\Phi|$ contours and a decrease in zonal mode strength for some zonal modes. The trends for nonlinear and quasilinear heat flux with triangularity agreed qualitatively, with the exception of $\delta = -0.5$. The exception of $\delta = -0.5$ was likely due to too low of simulation resolutions and not a feature of the geometry. Quantitatively, nonlinear heat fluxes were significantly lower than the quasilinear heat fluxes for the same triangularity cases. The decrease in nonlinear heat flux with increased triangularity did not correlate with the relative amplitude of zonal modes to nonzonal modes. However there is evidence—though not conclusive—that the temperature gradient falls within a Dimits region for $\delta = 0.75$, potentially explaining the exceptionally low nonlinear heat flux for that geometry.

6.2 Future Research

6.2.1 Nonlinear Convergence Tests

As has been mentioned several times, the nonlinear simulations presented in this thesis have not been shown to have numerically converged. Therefore more simulations of the geometries discussed in this thesis must be performed to ensure numerical convergence. Convergence in three areas are needed for nonlinear simulations to have fully numerically converged: parallel spatial resolution ($nz0$), parallel velocity resolution ($nv0$), and box size (k_y^{\min}). In addition, $\delta = 0.5$ and $\delta = -0.25$ have not clearly shown convergence in $nz0$ as well due to the quasi-periodic increases in $\langle Q_{es} \rangle$. To test if these quasi-periodic increases were intrinsic on shaping or an artifact of simulation resolution, repeating $nz0$ convergence tests for $\delta = 0.5$ and $\delta = -0.25$ with an increase in $nv0$ or box size is recommended.

6.2.2 Other Tokamak Shaping Studies

In practice, tokamaks often have both finite triangularity and elongation greater than one, therefore studies exploring the full 2D parameter space of κ and δ would provide a more complete picture on how tokamak shaping affects ITG turbulence. The methods described in this thesis provide a framework for which the full 2D shaping study could be performed. The linear studies would not be resource intensive, and obtaining a quasilinear heat flux computation for each shaping would follow easily. However, the nonlinear simulations would be resource intensive, but some time would be saved from using the converged simulation settings if the research suggested in the previous section is performed first.

6.2.3 Temperature Gradient Scans

As mentioned in Section 5.2, there is evidence the case $\delta = 0.75$ may be in a Dimits region, and the other cases were not. If so, this implies the Dimits shift may have a dependence on shaping. Very little is known about the Dimits shift, and performing a temperature scan on each of the shaping cases presented in this thesis would determine if $\delta = 0.75$ is in a Dimits region, if the Dimits shift depends on shaping, or if the critical temperature gradient depends on shaping. To determine the critical temperature gradient, linear simulations of

the temperature scans would need to be performed. Then, to find the Dimits shift, nonlinear simulations of the temperature scans would need to be done.

6.2.4 ITG Saturation Metric

Recent theory on ITG turbulence saturation suggests an amendment to the mixing length estimate of $\chi \sim \gamma/k_{\perp}^2$ used in quasilinear heat flux estimates would increase the accuracy of a quasilinear heat flux estimate [52]. The new theory uses a fluid model of ITG turbulence with adiabatic electrons to identify a turbulent correlation time τ for a three mode coupling by which energy is transferred nonlinearly between a stable mode, zonal mode, and unstable mode. A code, PTSM3D, has been developed to compute the turbulent correlation time for the three mode coupling [25]. The new scaling for a turbulent diffusivity is $\chi \sim \gamma/(\tau C^2 k_{\perp}^2)$, where C is constant associated with τ . Computing an updated quasilinear heat flux with the ITG saturation metric would provide insight into how the new theory predicts the role of ITG saturation in heat flux for tokamaks with various geometries and whether including the $1/(\tau C^2)$ term in Q_L improves agreement with nonlinear heat fluxes.

6.2.5 Electron Turbulence

Drift wave turbulence is not limited to ion temperature gradient modes; other modes arising from electron behavior, such as trapped electron modes (TEMs) and electron temperature gradient (ETG) modes, are known to exist. A recent study on the DIII-D tokamak showed a configuration with negative triangularity had high confinement with low enough edge pressure to prevent terminal disruptions in the plasma. In this study, a gyrokinetic simulation of the reconstructed experimental equilibrium showed suppression of TEM turbulence in the negative triangularity configuration compared to its positive triangularity counterpart [53]. The full implications of how tokamak shaping effects TEM and ETG turbulence is unknown, and a sound computational and theoretical understanding could help guide further experiments on negative triangularity configurations. A study using similar methods as the work in this thesis with the appropriate settings in GENE would illuminate the effect of tokamak shaping on electron turbulence.

6.2.6 Stellarator Shaping

As mentioned in Section 1.2.3, optimizing a stellarator to reduce turbulence is a large area of ongoing research. Building an optimization routine for turbulence requires knowing how changing each shaping parameter affects turbulence. Therefore a study varying stellarator shaping parameters using the methods of the work presented in this thesis would be a necessary first step towards a turbulence-optimized stellarator. A study independently varying each stellarator shaping parameter would be a large undertaking, because stellarator flux surfaces are often described with many shaping parameters, a result of stellarator flux

surface shaping being often described with a Fourier representation [54]:

$$R(\psi, \Theta, \zeta) = \sum_{m,n} R_{m,n} \cos(m\Theta + n\zeta), \quad (6.1)$$

$$Z(\psi, \Theta, \zeta) = \sum_{m,n} Z_{m,n} \sin(m\Theta + n\zeta). \quad (6.2)$$

Because each mode coefficient is a shaping parameter, using as few as five m and n modes means there are at most 20 independent shaping parameters to vary. Therefore, a stellarator shaping study similar to the work in this thesis would be resource intensive.

References

- [1] U.S. Energy Information Administration (EIA) Independent Analysis & Statistics. Monthly Energy Review August 2018. Technical Report August, U.S. Energy Information Administration, 2018.
- [2] Shahriar Shafiee and Erkan Topal. When will fossil fuel reserves be diminished? *Energy Policy*, 37(1):181–189, 2009.
- [3] J. Ongena and G. Van Oost. Energy for future centuries: Prospects for fusion power as a future energy source. *Fusion Sci. Technol.*, 61(2T):3–15, 2012.
- [4] John Wesson. *Tokamaks*. Oxford University Press, 3 edition, 2004.
- [5] Toroidal and poloidal. https://en.wikipedia.org/wiki/Toroidal_and_poloidal. Accessed: 2018-11-20.
- [6] Yuhong Xu. A general comparison between tokamak and stellarator plasmas. *Matter Radiat. Extrem.*, 1(4):192–200, 2016.
- [7] David A. Gates, David Anderson, S. Anderson, M. Zarnstorff, Donald A. Spong, Harold Weitzner, G. H. Neilson, D. Ruzic, D. Andruczyk, J. H. Harris, H. Mynick, C. C. Hegna, O. Schmitz, J. N. Talmadge, D. Curreli, D. Maurer, A. H. Boozer, S. Knowlton, J. P. Allain, D. Ennis, G. Wurden, A. Reiman, J. D. Lore, Matt Landreman, J. P. Freidberg, S. R. Hudson, M. Porkolab, D. Demers, J. Terry, E. Edlund, S. A. Lazerson, N. Pablant, R. Fonck, F. Volpe, J. Canik, R. Granetz, A. Ware, J. D. Hanson, S. Kumar, C. Deng, K. Likin, A. Cerfon, A. Ram, A. Hassam, S. Prager, C. Paz-Soldan, M. J. Pueschel, I. Joseph, and A. H. Glasser. *Stellarator Research Opportunities: A Report of the National Stellarator Coordinating Committee*, volume 37. Springer US, 2018.
- [8] R. J. Buttery, B. Covele, J. Ferron, A. Garofalo, C. T. Holcomb, T. Leonard, J. M. Park, T. Petrie, C. Petty, G. Staebler, E. J. Strait, and M. Van Zeeland. DIII-D Research to Prepare for Steady State Advanced Tokamak Power Plants. *J. Fusion Energy*, 38(1), 2019.
- [9] Paulett C. Liewer. Measurements of microturbulence in tokamaks and comparisons with theories of turbulence and anomalous transport. *Nucl. Fusion*, 25(5):543–621, 1985.
- [10] O. Grulke and T. Klinger. Large-scale fluctuation structures in plasma turbulence. *New J. Phys.*, 4.
- [11] P. W. Terry, D. A. Baver, and Sangeeta Gupta. Role of stable eigenmodes in saturated local plasma turbulence. *Phys. Plasmas*, 13(2), 2006.
- [12] Toroidal coordinates. http://fusionwiki.ciemat.es/wiki/Toroidal_coordinates. Accessed: 2018-11-20.
- [13] W. D. D’haeseller, W. N. G. Hitchon, J. D. Callen, and J. L. Shohet. *Physics Flux Coordinates and Magnetic Field Structure*. Springer-Verlag, 1991.

- [14] H Grad and H Rubin. Hydromagnetic equilibria and force-free fields. Technical report, United Nations (UN), 1958.
- [15] V. D. Shafranov. Plasma equilibrium in a magnetic field. *Rev. Plasma Phys.*, 2:103, 1966.
- [16] J. M. Greene and M. S. Chance. The Second Region of Stability Against Ballooning Modes. *Nucl. Fusion*, 21(4):453–464, 1981.
- [17] R. L. Miller, M. S. Chu, J. M. Greene, Y. R. Lin-Liu, and R. E. Waltz. Noncircular, finite aspect ratio, local equilibrium model. *Phys. Plasmas*, 5(4):973–978, 1998.
- [18] C. Mercier and H. Luc. Lectures in plasma physics : the magnetohydrodynamic approach to the problem of plasma confinement in closed magnetic configurations. Technical report, Commission of the European Communities, Brussels, 1974.
- [19] C. C. Hegna. Local three-dimensional magnetostatic equilibria. *Phys. Plasmas*, 7(10):3921–3928, 2000.
- [20] L. L. Lao, S. P. Hirshman, and R. M. Wieland. Variational moment solutions to the Grad Shafranov equation. *Phys. Fluids*, 24(8):1431–1441, 1981.
- [21] J. M. Duff. <https://gitlab.com/jduff2/NE3DLE>, 2019.
- [22] J. W. Connor, R. J. Hastie, and J. B. Taylor. Shear, periodicity, and plasma ballooning modes. *Phys. Rev. Lett.*, 40(6):396–399, 1978.
- [23] P. Xanthopoulos, W. A. Cooper, F. Jenko, Yu Turkin, A. Runov, and J. Geiger. A geometry interface for gyrokinetic microturbulence investigations in toroidal configurations. *Phys. Plasmas*, 16(8):1–13, 2009.
- [24] I. G. Abel, G. G. Plunk, E. Wang, M. Barnes, S. C. Cowley, W. Dorland, and A. A. Schekochihin. Multiscale gyrokinetics for rotating tokamak plasmas: Fluctuations, transport and energy flows. *Reports Prog. Phys.*, 76(11), 2013.
- [25] Benjamin J Faber. *The Role of Three-Dimensional Geometry on Turbulence in Quasi-Helically Symmetric Stellarators*. Doctor of philosophy, University of Wisconsin-Madison, 2018.
- [26] M. A. Beer. *Gyrofluid Models of Turbulent Transport in Tokamaks*. Phd, Princeton University, 1995.
- [27] P. B. Snyder. *Gyrofluid Theory and Simulation of Electromagnetic Turbulence and Transport in Tokamak Plasmas*. Phd, Princeton University, 1999.
- [28] S. E. Parker, W. Dorland, R. A. Santoro, M. A. Beer, Q. P. Liu, W. W. Lee, and G. W. Hammett. Comparisons of gyrofluid and gyrokinetic simulations. *Phys. Plasmas*, 1(5):1461–1468, 1994.

- [29] A. M. Dimits, G. Bateman, M. A. Beer, B. I. Cohen, W. Dorland, G. W. Hammett, C. Kim, J. E. Kinsey, M. Kotschenreuther, A. H. Kritz, L. L. Lao, J. Mandrekas, W. M. Nevins, S. E. Parker, A. J. Redd, D. E. Shumaker, R. Sydora, and J. Weiland. Comparisons and physics basis of tokamak transport models and turbulence simulations. *Phys. Plasmas*, 7(3):969–983, 2000.
- [30] H. Sugama, T. H. Watanabe, and W. Horton. Collisionless kinetic-fluid model of zonal flows in toroidal plasmas. *Phys. Plasmas*, 14(2), 2007.
- [31] H. Biglari, P. H. Diamond, and P. W. Terry. Influence of sheared poloidal rotation on edge turbulence. *Phys. Fluids B*, 2(1):1–3, 1990.
- [32] M. N. Rosenbluth and F. L. Hinton. Poloidal Flow Driven by Ion-Temperature-Gradient Turbulence in Tokamaks. *Phys. Rev. Lett.*, 80(4):724–727, 1998.
- [33] Osamu Yamagishi and Hideo Sugama. Fluid simulation of tokamak ion temperature gradient turbulence with zonal flow closure model. *Phys. Plasmas*, 23(3), 2016.
- [34] M. A. Beer, S. C. Cowley, and G. W. Hammett. Field-aligned coordinates for nonlinear simulations of tokamak turbulence. *Phys. Plasmas*, 2(7):2687–2700, 1995.
- [35] Gyrokinetic Electromagnetic Numerical Experiment. <http://genecode.org>. Accessed: 2019-01-10.
- [36] F. Jenko, W. Dorland, M. Kotschenreuther, and B. N. Rogers. Electron temperature gradient driven turbulence Electron temperature gradient driven turbulence. *Phys. Plasmas*, 7(5):1904–1910, 2000.
- [37] C. Kessel, J. Manickam, G. Rewoldt, and W. M. Tang. Improved plasma performance in tokamaks with negative magnetic shear. *Phys. Rev. Lett.*, 72(8):1212–1215, 1994.
- [38] T. M. Antonsen, J. F. Drake, P. N. Guzdar, A. B. Hassam, Y. T. Lau, C. S. Liu, and S. V. Novakovskii. Physical mechanism of enhanced stability from negative shear in tokamaks: Implications for edge transport and the LH transition. *Phys. Plasmas*, 3(6):2221–2223, 1996.
- [39] D. D. Hua, X. Q. Xu, and T. K. Fowler. Ion-temperature-gradient modes in noncircular tokamak geometry. *Phys. Fluids B*, 4(10):3216–3225, 1992.
- [40] R. E. Waltz and R. L. Miller. Ion temperature gradient turbulence simulations and plasma flux surface shape. *Phys. Plasmas*, 6(11):4265–4271, 1999.
- [41] Mike Kotschenreuther, G. Rewoldt, and W. M. Tang. Comparison of initial value and eigenvalue codes for kinetic toroidal plasma instabilities. *Comput. Phys. Commun.*, 88(2):128–140, 1995.
- [42] Alexander Kendl and Bruce D. Scott. Flux-surface shaping effects on tokamak edge turbulence and flows. *Phys. Plasmas*, 13(1):1–9, 2006.

- [43] J. E. Kinsey, R. E. Waltz, and J. Candy. The effect of plasma shaping on turbulent transport and EXB shear quenching in nonlinear gyrokinetic simulations. *Phys. Plasmas*, 14(10), 2007.
- [44] E. A. Belli, G. W. Hammett, and W. Dorland. Effects of plasma shaping on nonlinear gyrokinetic turbulence. *Phys. Plasmas*, 15(9), 2008.
- [45] R. E. Waltz, G. D. Kerbel, and J. Milovich. Toroidal gyro-Landau fluid model turbulence simulations in a nonlinear ballooning mode representation with radial modes. *Phys. Plasmas*, 1(7):2229–2244, 1994.
- [46] B. Scott. E x B Shear Flows and Electromagnetic Gyrofluid Turbulence. *Phys. Plasmas*, 7(5):1845–1856, 2000.
- [47] Bruce D. Scott. Free-energy conservation in local gyrofluid models. *Phys. Plasmas*, 12(10):1–18, 2005.
- [48] J. Candy and R. E. Waltz. An Eulerian gyrokinetic-Maxwell solver. *J. Comput. Phys.*, 186:545–581, 2003.
- [49] R. Bravenec, J. Citrin, J. Candy, P. Mantica, and T. Görler. Benchmarking the GENE and GYRO codes through the relative roles of electromagnetic and E x B stabilization in JET high-performance discharges. *Plasma Phys. Control. Fusion*, 58(12), 2016.
- [50] M. J. Pueschel, T. Dannert, and F. Jenko. On the role of numerical dissipation in gyrokinetic Vlasov simulations of plasma microturbulence. *Comput. Phys. Commun.*, 181(8):1428–1437, 2010.
- [51] B. N. Rogers, W. Dorland, and M. Kotschenreuther. Generation and stability of zonal flows in ion-temperature-gradient mode turbulence. *Phys. Rev. Lett.*, 85(25):5336–5339, 2000.
- [52] C. C. Hegna, P. W. Terry, and B. J. Faber. Theory of ITG turbulent saturation in stellarators: identifying mechanisms to reduce turbulent transport. *Phys. Plasmas*, 25(2):1–17, 2018.
- [53] M. E. Austin, A. Marinoni, M. L. Walker, M. W. Brookman, J. S. DeGrassie, A. W. Hyatt, G. R. Mckee, C. C. Petty, T. L. Rhodes, S. P. Smith, C. Sung, K. E. Thome, and A. D. Turnbull. Achievement of Reactor-Relevant Performance in Negative Triangularity Shape in the DIII-D Tokamak. *Phys. Rev. Lett.*, 122(11), 2019.
- [54] S. P. Hirshman and J. C. Whitson. Steepest-descent moment method for three-dimensional magnetohydrodynamic equilibria. *Phys. Fluids*, 26(12):3553–3586, 1983.